N O T I C E

THIS DOCUMENT HAS BEEN REPRODUCED FROM
MICROFICHE. ALTHOUGH IT IS RECOGNIZED THAT
CERTAIN PORTIONS ARE ILLEGIBLE, IT IS BEING RELEASED
IN THE INTEREST OF MAKING AVAILABLE AS MUCH
INFORMATION AS POSSIBLE

THE UNIVERSITY OF KANSAS CENTER FOR RESEARCH, INC.

2291 Irving Hill Drive—Campus West
Lawrence, Kansas 66045

A VORTEX-FILAMENT AND-CORE MODEL

FOR WINGS WITH EDGE VORTEX SEPARATION

A VORTEX-FILAMENT AND-CORE MODEL

FOR WINGS WITH EDGE VORTEX SEPARATION

by

Jenn-Louh Pao and C. Edward Lan

Techn¹cal Report CRINC-FRL-424 -1

November 1981

The Flight Research Laboratory

The University of Kansas Center for Research, Inc.

Lawrence, Kansas 66045

for

Langley Research Center

National Aeronautics and Space Administration

Abstract

An improved vortex filament-vortex core method for predicting aerodynamic characteristics of slender wings with edge vortex separation has been developed. Semi-empirical but simple methods are used to determine the initial positions of the free sheet and vortex core. Comparison with available data indicates that: (1) the present method is generally accurate in predicting the lift and induced drag coefficients but the predicted pitching moment is too positive; (2) the spanwise lifting pressure distributions estimated by the one vortex core solution of the present method are significantly better than the results of Mehrotra's method relative to the pressure peak values for the flat delta; (3) the two vortex-core system applied to the double delta and strake-wing produce overall aerodynamic characteristics which have good agreement with data except for the pitching moment; and (4) the computer time for the present method is about two thirds of that of Mehrotra's method.

Table of Contents

1. List of Symbols

<u>Symbols</u>

a	Percentage of allowed movement of a free segment based on the total velocity at its control point
a'	$\text{Tan } \alpha / \text{Tan}(90^{\circ} - \Lambda)$
a_i	Fourier coefficients
a_ℓ	Leading-edge boundary condition term
$\vec{a}$	$(x_1 - x)\vec{i} + (y_1 - y)\vec{j} + (z_1 - z)\vec{k}$ m (ft)
$\vec{a}'$	$(x_1 - x)\vec{i} + \beta(y_1 - y)\vec{j} + \beta(z_1 - z)\vec{k}$ m (ft)
A_{ij}	Induced downwash coefficient due to wing
b	Wing span m (ft)
$\vec{b}$	$(x_2 - x)\vec{i} + (y_2 - y)\vec{j} + (z_2 - z)\vec{k}$ m (ft)
$\vec{b}'$	$(x_2 - x)\vec{i} + \beta(y_2 - y)\vec{j} + \beta(z_2 - z)\vec{k}$ m (ft)
B_{ik}	Induced downwash coefficient due to leading-edge vortex system m^{-1} (ft^{-1})
c	Local chord m (ft)
$\bar{c}$	Mean geometric chord m (ft)
c_d	Sectional induced drag coefficient
C_{D_i}	$C_D - (C_D/C_{L=0}$ of cambered wings) Induced drag coefficient (Drag/($q_\infty S$))
c_ℓ	Sectional lift coefficient
C_L	Total lift coefficient (Lift/($q_\infty S$))
c_m	Sectional pitching moment coefficient about Y-axis
C_m	Total pitching moment coefficient about Y-axis based on $\bar{c}$ (Moment/($q_\infty S \bar{c}$))
C_{L_1}	The initially computed lift coefficient in the core model
C_{L_s}	The reference lift coefficient based on suction analogy
C_p	Pressure coefficient ($(P-P_\infty)/q_\infty$)

c_R	Root chord m (ft)
c_t	Sectional leading-edge thrust coefficient
C_T	Total leading-edge thrust coefficient (Thrust/$(q_\infty S)$)
c_{tip}	Side-edge chord length m (ft)
F_y, F_z	The Joukowsky force components acting on a segment of vortex core N (lb)
$\vec{G}_1$	$\dfrac{\vec{a} \times \vec{\ell}}{\lvert \vec{a}' \times \vec{\ell}' \rvert^2} \left(\dfrac{\vec{b}'}{\lvert \vec{b}' \rvert} - \dfrac{\vec{a}'}{\lvert \vec{a}' \rvert} \right) \cdot \vec{\ell}'$ m^{-1} (ft^{-1})
$\vec{G}_2$	$\displaystyle\int_{x'}^{\infty} \dfrac{(\vec{R}_1 - \vec{R}) \times d\vec{\ell}}{R_\beta^3}$ m^{-1} (ft^{-1})
$\vec{\imath}$, $\vec{\jmath}$, $\vec{k}$	Unit vectors along X-, Y- and Z- axes, respectively
$\vec{\ell}$	$(x_2 - x_1)\vec{\imath} + (y_2 - y_1)\vec{\jmath} + (z_2 - z_1)\vec{k}$ m (ft)
$\vec{\ell}'$	$(x_2 - x_1)\vec{\imath} + \beta(y_2 - y_1)\vec{\jmath} + \beta(z_2 - z_1)\vec{k}$ m (ft)
M	Mach number, or number of spanwise strips plus one
M_∞	Free stream Mach number
N	Number of chordwise bound elements
N_a	$N(M - 1)$
N_b	$(M - 1)$
$\vec{n}$	A unit vector normal to the wing surface
$\vec{n}_\infty$	A unit vector normal to the free stream velocity vector
q	Dynamic pressure, $(\rho V_\infty^2/2)$ N/m^2 (lb/ft^2)
q_∞	Free stream dynamic pressure $(\rho_\infty V_\infty^2 /2)$, N/m^2 (lb/ft^2)
r	Perpendicular distance of bound element to the core segment
r_c	Characteristic radius of vortex core cm (in.)
R_β	$\left[(x_2 - x_1)^2 + \beta^2(y_2 - y_1)^2 + \beta^2(z_2 - z_1)^2 \right]^{\frac{1}{2}}$
$\vec{R}$	$x\vec{\imath} + y\vec{\jmath} + z\vec{k}$ m (ft)
$\vec{R}'$	$x\vec{\imath} + \beta y\vec{\jmath} + \beta z\vec{k}$ m (ft)
$\vec{R}_\ell$	$\xi\vec{\imath} + \eta\vec{\jmath} + \zeta\vec{k}$ m (ft)
$\vec{R}_\ell'$	$\xi\vec{\imath} + \beta\eta\vec{\jmath} + \beta\zeta\vec{k}$ m (ft)

S	Reference wing area m^2 (ft^2)
$\vec{t}_\infty$	A unit vector along the free stream velocity vector
u, v, w	Induced velocity components along X-, Y-, and Z-axes, respectively m/sec (ft/sec)
V_∞	Free stream velocity m/sec (ft/sec)
$\vec{U}$	Induced velocity vector due to leading-edge vortex system m/sec (ft/sec)
$\vec{V}$	Induced velocity vector due to wing m/sec (ft/sec)
w'	Induced normal wash m/sec (ft/sec)
x, y, z	Wing rectangular coordinate system with positive X-axis along axis of symmetry pointing downstream, positive Y-axis pointing to right, and positive Z-axis pointing upward. m (ft)
$\bar{y}, \bar{z}$	The centroid of the leading-edge vortex filament system m (ft)
$z_c (x, y)$	The ordinate of camber surface measured from X-Y plane m (ft)
z_{min}	Minimum vertical distance of a vortex segment from the wing plane m (ft)

Greek

α	Angle of attack (rad)
β	$(1 - M^2)^{\frac{1}{2}}$
γ	Vortex density referred to freestream velocity
Γ	Concentrated vortex strength based on free stream velocity m (ft)
ΔC_p	Differential pressure coefficient, $(C_{p_{lower}} - C_{p_{upper}})$
θ	Chordwise angular distance (rad)
Λ	Sweep angle of wing leading-edge
ρ	Fluid density kg/m^3 ($slugs/ft^3$)
ϕ	Spanwise angular distance (rad)
ϕ_y	Local dihedral angle, $(Tan^{-1} \frac{\partial z_c}{\partial y})$ (rad)
ψ	Sweep angle of leading-edge vortex element or wing bound element (rad)
ξ, η, ζ	Integration variables in cartesian system m (ft)
λ_y	Relaxation parameter for the y coordinate of vortex core
λ_z	Relaxation parameter for the y coordinate of vortex core

Subscripts

1	The first endpoint of a vortex element
2	The second endpoint of a vortex element
B	Bound element
cp	Control point
i	Chordwise bound element number
j	Spanwise strip number
k	Chordwise bound element number
ℓ	Leading-edge
ℓe	Leading-edge vortex element
L	Left trailing leg
R	Right trailing leg
t	Trailing-edge
T	Chordwise trailing vortices

2. Introduction

It is well known that at moderate to high angles of attack, the flow separates going around the leading-edge of a sharp-edged wing. The separation produces rolled-up vortex sheets above the wing surface which emanate from the local leading-edge. The concentrated vorticity above the wing induces high suction pressure over a large portion of the upper surface of the wing, resulting in a nonlinear contribution to the wing loading. In the analysis and design of slender high speed airplanes flying at off design conditions, a detailed knowledge of the particular loading on the wing surface is required to estimate aerodynamic performance and structural loads.

There have been several different theoretical approaches in solving the vortex flow separation problem since the early 1950's. In general, they can be classified as conical and non-conical flow methods.

In the first category, based on the slender wing approximation, the solutions are obtained from a simplified governing flow equation by neglecting the variation of longitudinal velocity. Therefore, the problem is solved in the so-called cross-flow plane. Legendre (ref. 1) assumed that the rolled-up vortex sheets could be replaced by a pair of concentrated cores over the wing and inboard of the leading-edge. Two boundary conditions were imposed such that velocities along the leading-edges must be finite and the total force on each isolated vortex must be zero. Later, Brown and Michael (ref. 2) used feeding cuts to connect the line vortices and the wing leading-edges. Again, the boundary conditions require tangency of flow on the wing surface, finite velocity at the leading-edges, and zero resultant force on the vortex-plus-cut combination. Mangler and

1

and Smith (ref. 3), modifying the model in reference 2, assumed that the vortex sheets are shed tangentially at leading-edges and roll up as spiral vortices. The boundary conditions of zero pressure discontinuity across the separated vortex sheet and zero total force on the vortex sheet and feed cut are imposed. Finally, Smith (ref. 4) developed the model of a segmented feeding vortex sheet by improving the numerical procedure in reference 3. The main shortcomings of all these models described above are limited to conical flow. The assumption of slenderness leads to a theory which is independent of Mach number. Thus, the theory breaks down at low Mach numbers in the trailing-edge regions, because the trailing-edge Kutta condition is not satisfied. It breaks down also when the aspect ratio is greater than one.

In the second category, the conical flow assumption is removed so that the Kutta conditions are satisfied at both leading-and trailing-edges. In the earlier stage of development, the classical lifting surface theory was extended by including a relatively simple representation of the leading-edge separation. Bollay (ref. 5) suggested a method for low aspect ratio rectangular wings in which all the vorticity is shed from the wing side-edge and is assumed to be along straight lines making an angle of $\alpha/2$ with respect to the wing planform. Gersten (ref. 6) and Garner and Lehrian (ref. 7) extended Bollay's model to cover wings of arbitrary shape. Vorticity is assumed to be shed from the leading-edges at an angle of $\alpha/2$ to the wing plane. The wing was replaced by a series of lifting elements. A Multhopp-type lifting surface method (ref. 8) was used to solve the integral equations in reference 7.

Nangia and Hancock (ref. 9) combined the conventional lifting surface theory with the detached flow model of Brown and Michael (ref. 2).

2

In the latter model, two concentrated cores lie above the wing, connected to the leading-edges by feeding cuts. The trailing wake consists of vortices shed from the trailing-edge and the continuing concentrated vortices. To determine the separated vortex strengths, their position and the wing vorticity distributions, the flow tangency condition on the wing surface and the trailing-edge Kutta condition are applied at selected collocation points, together with the conditions of zero loading on the vortex and cut. The leading-edge Kutta condition is automatically satisfied by the choice of the loading function.

When the wing loading distribution is not required, Polhamus' method of leading-edge suction analogy (ref. 10) has been found to be simple and accurate. He assumed that the overall lift force can be estimated from the sum of potential and vortex lift contributions. The potential lift is defined as the lift due to potential flow about the wing with zero leading-edge suction. Vortex lift is caused by large suction forces induced by vortices in the separated flow, acting on the upper surface of the wing, and is assumed to be equal to, in magnitude, the leading-edge suction force in the attached potential flow.

The detailed literature survey of the above flow concepts were reviewed by Matoi (ref. 11) and Parker (ref. 12).

Since 1970, several methods have been developed by including a more precise representation of the leading-edge separation. Two popular methods under the second category are of the doublet-panel type (refs. 13, 14 and 15) and the free vortices (refs. 16, 17 and 18). In the method of doublet-panel type, such as the free-vortex-sheet method of Johnson, et al. (refs. 13 and 14), the wing surface and free sheet are replaced with doublet panels that have biquadratic strength. The free sheet, whose shape and

3

position must be determined by the iteration, is attached under all conditions to a fed sheet. The fed sheet approximately represents the vortex core effect and moves with the free sheet. The entire set of doublet strengths is determined simultaneously during the iteration process. Hoeijmakers (ref. 15) extended the method of Johnson, et al. (ref. 14) by including the entrainment effect of rotational cores. In this model, the spiralling free shear layer springing from the leading-edge is replaced by a free vortex sheet which is terminated by a combination of a feeding sheet and a discrete line vortex and sink. The strength of the sink is related to the entrainment of the rotational core and derived from semi-empirical arguments. The combination of vortex/sink and feeding sheet sustains no resultant force and produces the condition needed for determining the vortex core position in the cross-flow plane. From references 13 to 15, the panel method has been shown to predict accurate results for flat delta wings. However, the computing time involved is lengthy and the methods are generally restricted to simple geometries.

In the method of free vortices, Mook and Maddox (ref. 16) have used an extension of the vortex lattice method to account for leading-edge separation. In addition to standard vortex lattice, a series of kinked vortex lines are assumed to be shed from the leading-edge. An iterative procedure is used to determine the strength and local flow directions with appropriate boundary condition. In the Kandil method (ref. 17), the flow is modelled in a manner similar to that of Mook and Maddox (ref. 16), but included wing-tip separation. In this model, the bound elements of the vortex lattices were unswept, and the wake behind the trailing-edge and tip vortex elements were force free. The quasi-vortex-lattice potential flow method of Lan (ref. 19) has been extended by Mehrotra (ref. 18) to include vortex flow effects. This is done by modelling with discrete trailing vortex filaments emanating from the leading-edges. The leading-edge Kutta condition is exactly

4

satisfied and partial span vortex separation is allowed. The results of Meh-
rotra's model (ref. 18) indicate that the predicted spanwise pressure distri-
bution is more diffused than the experimental data show. This is because the
effect of a concentrated vortex core in the real flow is not well represented
by a number of free vortices. From the published results, it is clear that
none of the existing free-vortex methods is capable of predicting accurately
the lifting pressure distribution over the wing surface within a reasonable
amount of computer time.

The main objectives of this investigation are : (1) to reduce the computer
time through the use of a pair of concentrated vortex cores above the wing sur-
face, which should also improve the pressure prediction of Mehrotra's model
(ref. 18); (2) to allow the effect of side-edge vortex separation; and (3) to
extend the method of reference 18 to more realistic geometries. Configurations,
which are applicable to real airplane geometries include features such as
camber, strakes and leading-edge vortex flaps. All these configurations will
be treated in this report.

In the following, the aforementioned improvement will be described. First,
the leading-edge vortex system is superimposed on the regular quasi-vortex-
lattice grid by using segmented vortex filaments, as shown in reference 18.
Second, the side-edge vortex system is obtained by extending all the bound
elements to the tip chord in the last vortex strip. Third, the leading-edge
diffused vortex elements, in reference 18, are allowed to merge into a con-
centrated core after two iterations.

5

3. Description of Theoretical Formulation

Mehrotra's method (ref. 18) is a diffused vortex-filament model of the vortex core but serves as a basis for the present method. In the present analysis, the basic assumptions are: (1) the wing is represented by a bound vortex sheet across which there exists a pressure difference; (2) the separated flow along leading-edges is represented by force free leading-edge vortex elements which feed vorticity into a concentrated core. In the present method, the Quasi-Vortex-Lattice method (QVLM) (ref. 19) is used to simplify the induced velocity expressions due to the wing bound vortex sheet.

During the iteration process, the following boundary conditions are imposed: (1) the wing surface must be impermeable; (2) Kutta conditions are imposed along the leading- and trailing-edges of the wing; (3) in the diffused vortex-filament model, the force free condition is applied on the leading-edge vortex filaments and trailing wake elements; and (4) in the core model, the force free condition is applied on the free vortex elements, concentrated core and trailing wake elements.

This is a non-linear problem because the strength of the wing bound vortices and free element vortices, the locations of the leading-edge free vortex elements, and the concentrated core are unknown.

3.1 Mathematical Model of the Wing

The wing lies in the x-y plane and the x-axis is taken to be streamwise along the wing center line. The origin of the right-handed rectangular coordinate system is assumed to be at the moment reference point of the wing.

3.1.1 Wing Bound Element and Trailing Vortices

According to the QVLM, the semi-circle method is used to determine the control station locations and the vortex strips in the spanwise direction, and the wing control points and bound elements in the chordwise direction. The

6

locations of bound- and trailing-vortex elements are as shown in Fig. 1. The
x-location of bound elements is given by

$$x_i = x_\ell + \frac{c}{2} \left(1 - \cos \left(\frac{2i - 1}{2N}\pi\right)\right), \quad i = 1, \text{---}N \tag{1}$$

where x_ℓ is the leading-edge x-coordinate, c is the local chord and N is
the number of bound elements in the chordwise direction. The spanwise lo-
cations of trailing vortices are given by

$$y_j = \frac{b}{4} \left(1 - \cos \left(\frac{2j - 1}{2M}\pi\right)\right), \quad j = 1, \text{---}M \tag{2}$$

where b is the wing span and M is the number of legs of trailing vorticity,
which is one higher than the number of spanwise vortex strips. The locations
of control points are given by

$$x_{cp_k} = x_{\ell_j} + \frac{c_j}{2} \left(1 - \cos \left(\frac{k}{N}\pi\right)\right), \quad k = 0, 1, \text{---}N \tag{3}$$

$$y_{cp_j} = \frac{b}{4} \left(1 - \cos \left(\frac{j}{M}\pi\right)\right), \quad j = 1, \text{---}(M - 1) \tag{4}$$

where x_{ℓ_j} and c_j are the leading-edge x-coordinate and local chord at y_{cp_j},
respectively.

For the strake-wing configuration, there are two sections in the span-
wise direction. Each spanwise section is divided into vortex strips by the
semi-circle method. The edges of the vortex strips in each section are ob-
tained through the following relation

$$y_j = y'_{k-1} + \frac{b_k}{2} \left(1 - \cos \left(\frac{2j - 1}{2M_k}\pi\right)\right), \quad j = 1, \text{---}M_k \tag{5}$$

and y control points are given by

$$y_{cp_i} = y'_{k-1} + \frac{b_k}{2} \left(1 - \cos \left(\frac{i}{M_k}\pi\right)\right), \quad i = 1, \text{---}M_k-1 \tag{6}$$

where b_k is the width of the kth spanwise section and M_k is the number of
spanwise strips plus one in k^{th} section (see Fig. 2).

y'_{k-1} are defined as

$$y'_0 = 0$$

and

$$y'_1 = b_1$$

3.2 Model of Free Vortex Element System

3.2.1 Leading-Edge Vortex System Geometry

The leading-edge vortex system is superimposed on the regular quasi-vortex-lattice grid. A typical leading-edge vortex element is shown by points A through J in Fig.3. These points are connected by a series of short straight segments. A typical set of initial locations for these segments is indicated with dashed lines and the locations after two iterations are given by solid lines.

The segments of the vortex element have the following characteristics:

(1) Initially, points A through E lie along a wing trailing vortex filament with point A being one root chord away from the trailing-edge (point D) in the downstream direction, and the line segments between A and D are parallel to the axis of symmetry. The segments B-C and C-D are 0.1 c_R long. The length of each line segment between A and B remains unchanged as the solution progresses. Segment B-C is allowed to move only in the vertical direction, whereas segment C-D is fixed in the wing plane because of the trailing-edge Kutta condition. Segment D-E is also fixed in the wing plane.

(2) Points E, F, G and H lie in the wing plane. The location of segment E-F is ahead of the wing first bound element and is given by

8

$$x_E = x_{\ell_E} + \frac{c_E}{2} \left(1 - \cos \left(\frac{\pi}{2(N+1)} \right) \right)$$ (7)

$$x_F = x_{\ell_F} + \frac{c_F}{2} \left(1 - \cos \left(\frac{\pi}{2(N+1)} \right) \right)$$ (8)

The segments F-G and G-H are of the same length and point G lies on the leading-edge. These segments are fixed in the wing plane to satisfy the leading-edge Kutta condition.

(3) The initial location of point I is a function of α and is given by (ref. 18)

$$x_I = x_F$$ (9)

$$y_I = y_F$$ (10)

$$z_I = 0.1 \, c_R \, \mathrm{Tan}\,(22.5 - 0.5\,\alpha), \quad \text{for } \alpha \leqslant 15^\circ$$ (11)

or

$$z_I = 0.1 \, c_R \, \mathrm{Tan}\,\alpha, \quad \text{for } \alpha > 15^\circ$$ (12)

Where c_R is the root chord and α is the angle of attack. Initially point J is one root chord away from the trailing-edge. The line connecting I and J may be divided into segments of equal length which lie in a plane parallel to the x-z plane. The initial height of these segments is approximately $0.1 \, c_R$ above the wing plane. In the final converged location, all segments between point H and J (free vortex elements, concentrated core and trailing wake elements) are aligned in the local velocity direction at their mid-points to satisfy the force free condition.

(4) The semi-infinite segments from point A to infinity and J to infinity are straight and are parallel to the undisturbed free stream direction. Since the far wake of the leading-edge vortex element has very little effect on the wing aerodynamic characteristics, the far wake is assumed to be semi-infinite and parallel to the free stream.

9

3.2.2 Side Edge Vortex System Geometry

To establish the side-edge vortex system as shown in Fig. 4, the leading-edge vortex element and wing bound element of the last vortex strip is modified as follows:

(1) Extend the leading-edge bound element to the side-edge (point D). Points D, E, F, G and H lie in the wing plane. The segments F-G, G-H, H-I and I through J are given in the same manner as in the preceding section. The extended leading-edge bound element consists of segments D-E and E-F. The location of each point is given by

$$x_D = x_{\ell_{Tip}} + \frac{c_{Tip}}{2} \left(1 - Cos \left(\frac{\pi}{2 \ (N + 1)} \right) \right) \tag{13}$$

$$x_F = x_{\ell_F} + \frac{c_F}{2} \left(1 - Cos \left(\frac{\pi}{2 \ (N+1)} \right) \right) \tag{14}$$

$$x_E = \frac{1}{2} \ (x_D + x_F) \tag{15}$$

(2) The initial location of each vortex segment along the trailing leg of the extended leading-edge bound element, point A through D, is given by

$$x_{j+1} = x_j + \Delta y \cos \frac{\alpha}{2} \tag{16}$$

$$y_{j+1} = y_{Tip} \tag{17}$$

$$z_{j+1} = z_j + \Delta y \sin \frac{\alpha}{2} \tag{18}$$

where

$\Delta y = 0.95$ x (width of the last vortex strip).

(3) Extend the regular wing bound element to the side-edge. (Points P, Q, R, S). Points P, Q, R and S lie in the wing plane and at the side-edge. The location of each point is given by

$$x_i = x_{\ell_{Tip}} + \frac{c_{Tip}}{2} \ (1 - \cos \ (\frac{2i - 1}{2N}\pi)), \ i = 1, \ ---N \tag{19}$$

$$y_i = y_{Tip} \tag{20}$$

10

where $x_{\ell_{Tip}}$ is the leading-edge x coordinate at the side-edge of the wing; c_{Tip} the side-edge local chord length.

(4) Initially, all the segments between points D and A, P and T, Q and V, etc. lie in a plane parallel to x-z plane at the wing side-edge. Points A, T, U, V and W are one root chord away from the trailing-edge. The initial side-edge vortex segment along points P through T (or Q through U, etc.) is given by,

$$x_{i+1} = x_i + \Delta x \cos \frac{\alpha}{2} \tag{21}$$

$$y_{i+1} = y_{Tip} \tag{22}$$

$$z_{i+1} = z_i + \Delta x \sin \frac{\alpha}{2} \tag{23}$$

where Δx is assumed to be half length of the side-edge chord.

(5) The semi-infinite segments from points A, J, T, U, etc. to infinity are straight and are parallel to the undisturbed free stream.

3.3 Induced Velocity Computation

3.3.1 Induced Velocity Due to Wing

In the quasi-vortex-lattice method (ref. 19), to satisfy wing boundary condition, the continuous vortex distribution over the wing is replaced by a quasi-continuous one, being continuous chordwise but stepwise constant in the spanwise direction. Thus, the wing surface can be divided into a number of vortex strips with the associated trailing vortices (Fig. 1). In any strip, consider a vortex element $\gamma\,dx$ with an arbitrary direction $\vec{l}$ (Fig. 5). The induced velocity due to all bound elements in the ith strip is given by (ref. 19)

$$\vec{V}_{i_1}(\vec{R}) = \frac{\beta^2}{4\pi} \int_{x_\ell}^{x_t} \gamma(x') \frac{\vec{a} \times \vec{l}}{|\vec{a}' \times \vec{l}'|^2} \left(\frac{\vec{b}'}{|\vec{b}'|} - \frac{\vec{a}'}{|\vec{a}'|} \right) \cdot \vec{l}'\,dx' \quad (24)$$

and due to the associated trailing vortices by

$$\vec{V}_{i_2}(\vec{R}) = \frac{\beta^2}{4\pi} \int_{x_\ell}^{x_t} \gamma(x') \left(\int_{x'}^{\infty} \frac{(\vec{R}_1 - \vec{R}) \times d\vec{l}}{R_\beta^3}\,dx' \right) \quad (25)$$

The transformation, $x' = x_\ell + c(y)(1-\cos\theta)/2$, reduce equations (24) and (25) to

$$\vec{V}_{i_1}(\vec{R}) = \frac{\beta^2 c(y)}{8\pi} \int_0^\pi \vec{G}_1(\theta)\,\gamma(\theta)\,\sin\theta\,d\theta \quad (26)$$

and

$$\vec{V}_{i_2}(\vec{R}) = \frac{\beta^2 c(y)}{8\pi} \int_0^\pi \vec{G}_2(\theta)\,\gamma(\theta)\,\sin\theta\,d\theta \quad (27)$$

where

$$\vec{G}_1(\phi) = \frac{\vec{a} \times \vec{l}}{|\vec{a}' \times \vec{l}'|^2} \left(\frac{\vec{b}'}{|\vec{b}'|} - \frac{\vec{a}'}{|\vec{a}'|} \right) \cdot \vec{l}'$$

$$\vec{G}_2(\phi) = \int_{x'}^{\infty} \frac{(\vec{R}_1 - \vec{R}) \times d\vec{l}}{R_\beta^3}$$

and $c(y) = x_t - x_\ell$. $\vec{a}$, $\vec{b}$, etc. are defined in the List of Symbols.

The total induced velocity due to the ith strip of vortex distribution is given by

$$\vec{V}_1 (\vec{R}) = \frac{\beta^2 c(y)}{8\pi} \int_0^\pi \vec{G}_1 (\theta) \gamma (\theta) \, Sin \theta \, d\theta$$

$$+ \frac{\beta^2 c(y)}{8\pi} \int_0^\pi \vec{G}_2' (\theta) \gamma (\theta) \, Sin \theta \, d\theta$$

$$- \frac{\beta^2 c(y)}{8\pi} \int_0^\pi \vec{G}_2'' (\theta) \gamma(\theta) \, Sin \theta \, d\theta \qquad (28)$$

Where the first term is due to bound element, second due to left leg of trailing element and third due to the right leg of trailing elements. The above integrals are reduced to finite sums through the mid-point trapezoidal rule (ref. 19):

$$\vec{V}_1 (\vec{R}) = \frac{\beta^2 c(y)}{8N} \sum_{k=1}^N (\vec{G}_{1_k} + \vec{G}_{2_k}' - \vec{G}_{2_k}'') \, \gamma_k \, Sin \, \theta_k \qquad (29)$$

where $\theta_k = (2k - 1) \, \pi/2N$ and locations of bound elements are given by

$$x_{1_k} = x_{\ell_1} + c_1 \xi_k \qquad (30)$$

$$x_{2_k} = x_{\ell_2} + c_2 \xi_k \qquad (31)$$

$$\xi_k = \tfrac{1}{2} (1 - Cos (\frac{2k - 1}{2N} \pi)), \, k = 1, - - - N \qquad (32)$$

and

$\quad x_{\ell_1} =$ the leading-edge x -coordinate at y_1 (left leg)

$\quad x_{\ell_2} =$ the leading-edge x-cordinate at y_2 (right leg)

$\quad c_1 =$ chord length at y_1

$\quad c_2 =$ chord length at y_2 .

The location of control points and trailing vortices are described in equations (1) through (6).

Thus, the induced volocity due to all vortex strips of the wing can be written as

$$\vec{V} (\vec{R}) = \sum_{i=1}^{M-1} \vec{V}_i (\vec{R}) \qquad (33)$$

13

3.3.2 Induced Velocity Due to Free Vortex Element System

The leading-edge free vortex system consists of $M - 1$ distinct vortex elements. Each element may have different number of small vortex segments. Assume that the ith set has L small segments. The induced velocity at a given point (x,y,z) due to j^{th} segment of ith element is given by (ref. 19)

$$\vec{U}_{ij}(\vec{R}) = \frac{\beta^2 \Gamma_i}{4\pi} \frac{\vec{a} \times \vec{\ell}}{|\vec{a}' \times \vec{\ell}'|^2} \left(\frac{\vec{b}'}{|\vec{b}'|} - \frac{\vec{a}'}{|\vec{a}'|} \right) \cdot \vec{\ell}' \qquad (34)$$

where

$$\vec{R} = x \,\vec{I} + y \,\vec{J} + z \,\vec{k}$$

$$\vec{a} = (x_j - x) \,\vec{I} + (y_j - y) \,\vec{J} + (z_j - z) \,\vec{k}$$

$$\vec{b} = (x_{j+1} - x) \,\vec{I} + (y_{j+1} - y) \,\vec{J} + (z_{j+1} - z) \,\vec{k}$$

$$\vec{\ell} = (x_{j+1} - x_j) \,\vec{I} + (y_{j+1} - y) \,\vec{J} + (z_{j+1} - z_j) \,\vec{k}$$

$$\vec{a}' = (x_j - x) \,\vec{I} + \beta (y_j - y) \,\vec{J} + \beta (z_j - z) \,\vec{k}$$

$$\vec{b}' = (x_{j+1} - x) \,\vec{I} + \beta (y_{j+1} - y) \,\vec{J} + \beta (z_{j+1} - z) \,\vec{k}$$

$$\vec{\ell}' = (x_{j+1} - x_j) \,\vec{I} + \beta (y_{j+1} - y_j) \,\vec{J} + \beta (z_{j+1} - z_j) \,\vec{k}$$

Γ_i = leading-edge bound vortex strength of ith strip.

The subscripts j and $j + 1$ correspond to the end point of jth segment. The induced velocity due to i^{th} element can be written as

$$\vec{U}_i(\vec{R}) = \sum_{j=1}^{L} \vec{U}_{ij}(\vec{R}) \qquad (35)$$

Therefore, the induced velocity due to the entire leading-edge free vortex elements is

$$\vec{U}(\vec{R}) = \sum_{i=1}^{M-1} \vec{U}_i(\vec{R}) \qquad (36)$$

3.4 Formulations of Wing Boundary Condition

The bound elements and the corresponding control points of the wing

14

surface are numbered from the leading-edge to the trailing-edge and from the root to the side-edge. The flow tangency condition can be written as

$$
\left[A_{ij}\right]\{\gamma_j\} + \left[B_{ik}\right]\{\Gamma_k\} = \begin{cases} \cos\alpha \ (\frac{dz}{dx})_i - \sin\alpha \\ \\ a_{\ell k} + \cos\alpha \ (\frac{dz}{dx})_k - \sin\alpha \end{cases} \quad \begin{array}{c} \overline{\text{} } \\ N_a \\ \text{---} \\ N_b \\ \underline{\text{} } \end{array} \qquad (37)
$$

where N_a is the total number of wing bound elements; N_b the number of leading-edge vortex elements; A_{ij} the induced downwash at the ith control point of wing due to a unit horseshoe vortex density at j; B_{ik} the induced downwash at the ith control point due to the kth leading-edge vortex element of unit strength; γ_j the vortex density of the jth bound element; Γ_k the strength of the kth leading-edge vortex element; $(dz/dx)_i$ the camber slope at the ith control point and α the angle of attack. According to equations (52) and (53) of reference 19, the leading-edge thrust coefficient is related to the normal-wash on the leading-edge by the following equation

$$
a_{\ell k} = (\text{induced normalwash} - \cos\alpha \ (\frac{dz}{dx})_k + \sin\alpha)\big|_{at \ \ell.e.} \qquad (38)
$$

which leads to the last expression on the right hand side of equation (37). In the expression, $a_{\ell k}$ is defined as (ref. 19)

$$
a_{\ell k} = N\sqrt{Tan^2 \ \Lambda + \beta^2} \ (\frac{2 \ c_{t_k} \ \cos\Lambda}{\pi \sqrt{1 - M_\infty^2 \ \cos^2 \Lambda}})^{\frac{1}{2}}
$$

where

N = number of chordwise bounded vortex elements

Λ = leading-edge sweep angle

M_∞ = free stream Mach number

$\beta = \sqrt{1 - M_\infty^2}$

c_{t_k} = sectional leading-edge thrust coefficient of the kth strip

For complete leading-edge separation cases, the sectional leading-edge suction

is zéro and so is $a_{\ell k}$.

3.5 Force Free Condition

The vortex segments of each free element above the wing surface and the trailing wake are to be aligned in the direction of local velocity vector calculated at their mid-points. Consider the ith segment of a vortex element. The coordinates of its end points are given by (x_i, y_i, z_i) and $(x_{i+1}, y_{i+1}, z_{i+1})$. Assume that the induced velocity at the mid-point of this segment at a given iteration is given by $(u\vec{i} + v\vec{j} + w\vec{k})$. In the following sections, the formulations of force free condition will be derived in the diffused vortex filament and core models respectively.

3.5.1 Formulation of Force Free Condition of Free Vortex Elements in The Diffused Vortex Filament Model

For the ith segment, the new location of the $(i+1)^{th}$ end point can be obtained by aligning the segment in the direction of local velocity vector. That is

$$x_{i+1} = x_i + \frac{u}{U} \Delta s \tag{40}$$

$$y_{i+1} = y_i + \frac{v}{U} \Delta s \tag{41}$$

$$z_{i+1} = z_i + \frac{w}{U} \Delta s \tag{42}$$

where

$$U = (u^2 + v^2 + w^2)^{\frac{1}{2}}$$

$$\Delta s = \left[(x_{i+1} - x_i)^2 + (y_{i+1} - y_i)^2 + (z_{i+1} - z_i)^2 \right]^{\frac{1}{2}}$$

Before equations (40) - (42) are used, the following points should be considered:

(1) The length of each segment is to be preserved.

(2) The free vortex segments above the wing should not come too close to the wing surface to avoid numerical difficulty in the present inviscid theory.

(3) The adjustment of the location of each segment to satisfy the force free condition should be such that it does not result in numerical

16

fluctuations.

Based on the above considerations, equations (40) to (42) will be modified as follows:

Consider the same i^{th} segment. If this segment moves "a" percent only according to the velocity computed at its mid-point, the equations (40) to (42) can be modified to be

$$\Delta y' = a \frac{v}{U} \Delta s + (1 - a)(y_{i+1} - y_i) \tag{43}$$

$$\Delta z' = a \frac{w}{U} \Delta s + (1 - a)(z_{i+1} - z_i) \tag{44}$$

$$\Delta x' = \left[\Delta s^2 - (\Delta y')^2 - (\Delta z')^2\right]^{\frac{1}{2}} \tag{45}$$

It follows that

$$x_{i+1} = x_i + \Delta x' \tag{46}$$

$$y_{i+1} = y_i + \Delta y' \tag{47}$$

$$z_{i+1} = z_i + \Delta z' \tag{48}$$

The free elements of the leading-edge vortex system have been restricted not to come any closer than a minimum specified height to the wing surface, which is given empirically by Mehrotra (ref. 18) as follows

$$z_{min} = 0.1 \ c_R \ Tan \ (22.5 - 0.5\alpha) \quad , \text{ for } \alpha \leq 15^{o} \tag{49}$$

$$z_{min} = 0.1 \ c_R \ Tan \ \alpha \quad\quad\quad , \text{ for } \alpha > 15^{o} \tag{50}$$

If z_{i+1} is less than z_{min}, it is then set z_{i+1} equal to z_{min} and $\Delta z'$ is recalculated by using

$$\Delta z' = z_{min} - z_i \tag{51}$$

This restriction is needed because whenever the free elements are close to the wing surface, they induce large velocities on the wing and vice versa, which makes the locations of free elements fluctuate. In the real flow, at small angles of attack, the leading-edge vortex system is weak and diffused. The effect of the free vortices is artificially reduced by increasing z_{min} as the angle of attack is decreased below 15 degrees. Note that equations (43) through (48) described above are mainly used to   (1) establish the leading-edge vortex filament system in the first two iterations; and (2) find the new position of

17

trailing wake elements and side-edge vortex system in the entire iteration process.

3.5.2 Formulation of Force Free Condition of Free Sheet Vortex Element in The Core Model

For the ith segment along a free vortex element between the leading-edge and concentrated core, the initial slopes are determined by the total induced velocities at the mid-point of this segment

$$\left(\frac{\Delta y}{\Delta x}\right)' = \frac{v}{u} \tag{52}$$

$$\left(\frac{\Delta z}{\Delta x}\right)' = \frac{w}{u} \tag{53}$$

The new slopes of the ith segment of a free vortex element are given by:

$$\left(\frac{\Delta y}{\Delta x}\right)^* = d^* \left(\frac{\Delta y}{\Delta x}\right) + (1 - d^*)\left(\frac{\Delta y}{\Delta x}\right)' \tag{54}$$

$$\left(\frac{\Delta z}{\Delta x}\right)^* = d^* \left(\frac{\Delta z}{\Delta x}\right) + (1 - d^*)\left(\frac{\Delta z}{\Delta x}\right)' \tag{55}$$

Similar to the parameter "a" in equations (43) and (44) of section 3.5.1, the relaxation parameter of free sheet, d^*, is used in equations (54) and (55) in the core model, to avoid any rapid variation of free sheet shape and divergence of the iteration procedure. The initial value of d^* is 0.5. During the iteration process, when the rate of change of the total free sheet vortex element force is less than five percent, d^* is set to 0.95.

Since the length of each segment is conserved, therefore,

$$\Delta s = \Delta x \left[1 + \left(\frac{\Delta y}{\Delta x}\right)^2 + \left(\frac{\Delta z}{\Delta x}\right)^2\right]^{\frac{1}{2}} \tag{56}$$

Hence

$$(\Delta x)^* = \frac{\Delta s}{\left[1 + \left(\frac{\Delta y}{\Delta x}\right)^{*2} + \left(\frac{\Delta z}{\Delta x}\right)^{*2}\right]^{\frac{1}{2}}} \tag{57}$$

It follows that

$$(\Delta y)^* = (\Delta x)^* \left(\frac{\Delta y}{\Delta x}\right)^* \tag{58}$$

$$(\Delta z)^* = (\Delta x)^* \left(\frac{\Delta z}{\Delta x}\right)^* \tag{59}$$

18

Thus, the new location of the $(i+1)^{th}$ end point is given by

$$x_{i+1} = x_i + (\Delta x)^* \tag{60}$$

$$y_{i+1} = y_i + (\Delta y)^* \tag{61}$$

$$z_{i+1} = z_i + (\Delta z)^* \tag{62}$$

3.5.3 Formulation of Force Free Condition of Vortex Core in The Core Model

During each iteration, the Joukowsky force acting on each segment of the core is computed. Let

$$\vec{F} = \vec{V} \times \vec{\Gamma}$$
$$= (u\vec{i} + v\vec{j} + w\vec{k}) \times (\Gamma_x \vec{i} + \Gamma_y \vec{j} + \Gamma_z \vec{k})$$

Then

$$\frac{F_y}{\Gamma_x u} = \frac{w}{u} - \frac{\Gamma_z}{\Gamma_x} = \frac{w}{u} - (\frac{\Delta z}{\Delta x}) \tag{64}$$

$$\frac{F_z}{\Gamma_x u} = \frac{\Gamma_y}{\Gamma_x} - \frac{v}{u} = (\frac{\Delta y}{\Delta x}) - \frac{v}{u} \tag{65}$$

If the new position of the core is such that $F_y = 0$ and $F_z = 0$, then

$$(\frac{w}{u})' - (\frac{\Delta z}{\Delta x})' = 0 \tag{66}$$

$$(\frac{\Delta y}{\Delta x})' - (\frac{v}{u})' = 0 \tag{67}$$

Assume that

$$(\frac{w}{u}) = (\frac{w}{u})'$$

$$(\frac{v}{u}) = (\frac{v}{u})'$$

Combining equations (64), (65) and (66), (67) yields the following equations for the ith segment:

$$(\frac{\Delta y}{\Delta x})'_i = (\frac{\Delta y}{\Delta x})_i - (\frac{F_z}{\Gamma_x u})_i \tag{68}$$

$$(\frac{\Delta z}{\Delta x})'_i = (\frac{\Delta z}{\Delta x})_i + (\frac{F_y}{\Gamma_x u})_i \tag{69}$$

The new slopes of the ith segment of the concentrated core are taken to be:

$$(\frac{\Delta y}{\Delta x})^*_i = (1 - \lambda_y)(\frac{\Delta y}{\Delta x})_i + \lambda_z (\frac{\Delta y}{\Delta x})'_i \tag{70}$$

$$(\frac{\Delta z}{\Delta x})^*_i = (1 - \lambda_z)(\frac{\Delta z}{\Delta x})_i + \lambda_y (\frac{\Delta z}{\Delta x})'_i \tag{71}$$

Where λ_y and λ_z are relaxation parameters and are discussed in Section 3.8.

19

Combining equations (68) through (71) results in:

$$\left(\frac{\Delta y}{\Delta x}\right)^*_i = \left(\frac{\Delta y}{\Delta x}\right)_i - \lambda_y \left(\frac{F_z}{\Gamma_x u}\right)'_i \tag{70}$$

$$\left(\frac{\Delta z}{\Delta x}\right)^*_i = \left(\frac{\Delta z}{\Delta x}\right)_i + \lambda_z \left(\frac{F_y}{\Gamma_x u}\right)_i \tag{71}$$

During the iteration process, when the rate of change of the vortex core force is less than five percent, the relaxation parameters λ_y and λ_z of each core segment will be further reduced by multiplying the factor 0.1. Thus, the movements of core segment will not cause excessive fluctuation in the aerodynamic characteristics.

Since the segment length is conserved, it follows that

$$\Delta s = \Delta x \left[1 + \left(\frac{\Delta y}{\Delta x}\right)^2 + \left(\frac{\Delta z}{\Delta x}\right)^2\right]^{\frac{1}{2}} \tag{74}$$

$$(\Delta x)^* = \frac{\Delta s}{\left[1 + \left(\frac{\Delta y}{\Delta x}\right)^{*2} + \left(\frac{\Delta z}{\Delta x}\right)^{*2}\right]^{\frac{1}{2}}} \tag{75}$$

Hence,

$$(\Delta y)^* = (\Delta x)^* \left(\frac{\Delta y}{\Delta x}\right)^*_i \tag{76}$$

$$(\Delta z)^* = (\Delta x)^* \left(\frac{\Delta z}{\Delta x}\right)^*_i \tag{77}$$

Thus, the new position of $(i+1)^{th}$ end point of the concentrated core are found as follows

$$x_{i+1} = x_i + (\Delta x)^* \tag{78}$$

$$y_{i+1} = y_i + (\Delta y)^* \tag{79}$$

$$z_{i+1} = z_i + (\Delta z)^* \tag{80}$$

In the present analysis, the effect of the secondary vortices has not been included.

3.6 Centroid of the Leading-Edge Vortex Filament System

After establishing the leading-edge vortex filament system based on exercising Mehrotra's code (ref. 18) through two iterations, the centroid of that diffused vortex element system can be found as follows (ref. 20):

Consider a series of cross flow planes, proceeding from the wing apex toward the trailing-edge. The centroids of the vortex filaments penetrating these planes are given by,

$$\bar{y}_j = \frac{\sum_{i=1}^{n_j} \Gamma_i \, y_{ij}}{\Gamma_{cj}} \tag{81}$$

$$\bar{z}_j = \frac{\sum_{i=1}^{n_j} \Gamma_i \, z_{ij}}{\Gamma_{cj}} \tag{82}$$

where,

$\bar{y}_j$, $\bar{z}_j$ are the centroid position in the jth plane,

y_{ij}, z_{ij} are the intersection position of the ith vortex filament with the jth plane,

Γ_i is the circulation around the ith vortex filament,

Γ_{cj} is the concentrated line vortex strength at the jth plane,

n_j is the number of vortex filaments penetrating the jth plane.

3.7 Modification of Z-Coordinates of the Initial Concentrated Core

In order to have better starting solution so that the number of iterations and computer time can be reduced, the initial z-coordinates of the concentrated core from Section 3.6 are modified to take the experimental values summarized by Smith (ref. 4):

$$
\begin{aligned}
z_v &= 0.154a' + 0.1 & a' &< 1.2 \\
z_v &= 0.1333a' + 0.158 & 1.2 &\le a' < 2.2 \\
z_v &= 0.13a' + 0.132 & a' &> 2.2
\end{aligned} \tag{83}
$$

where

$$a' = \text{Tan } \alpha / \text{Tan } \theta$$

$$\theta = 90^{\circ} - \Lambda$$

z_v is the nondimensional z-coordinate of the concentrated core, referring to the local semi-span; Λ the leading-edge sweep angle; and α the angle of attack. Equation (83) will be used only in the simple wing configuration.

The initial configuration on the core model, on the right half of the wing, is shown in Figs. 6A through 6C. The top view of the initial free sheet and the modified y-coordinate of the core location are shown on the x-y plane in Fig. 6A. The initial modified y-coordinate of the core location is such that it is at least at a location equal to 60 percent of the local semi-span of the wing (see references 4 and 22). The rear view of the detailed free sheet shape and its relative vortex core location above the wing surface are shown on the y-z plane in Fig. 6B. The side view of the free sheet and the modified z-coordinate of the core location are shown on the x-z plane in Fig. 6C. Note that the initial modified z-coordinate of the core location is based on equation (83).

3.8 Formulation of Relaxation Parameters in the Core Model

In the first two iterations of the core model, the core is forced to move either in the y or z direction. The direction depends on the sign and the difference between the initially computed lift coefficient and the reference lift coefficient based on the suction analogy (references 26 and 27). From the numerical experimentation, the relaxation parameters λ_y and λ_z, in equations (70) through (73), are taken as follows:

First iteration

If the initially computed lift coefficient is smaller than the reference lift coefficient based on the suction analogy, the core will move down and the corresponding relaxation parameter is

$$\lambda_{z_1} = -1.5 \frac{(C_{L_s} - C_{L_i})}{(C_{L_s} \, \text{Tan} \, \alpha)} \tag{84}$$

If the initially computed lift coefficient is greater than the reference lift coefficient, the core will move out and the relaxation parameter is

$$\lambda_{y_1} = -2.0 \frac{(C_{L_i} - C_{L_s}) \, \text{Sin} \, \alpha}{C_{L_s}} \tag{85}$$

where C_{L_s} is the reference lift coefficient, and C_{L_i} is the initially computed lift coefficient. The initial set of λ_{y_1} and λ_{z_1} are designed so that the

22

movement of core segments is proportional to the difference in C_{L_1} and C_{L_s}. Also, the higher the angle of attack, the larger the value of λ_{y_1} or the lower the value of λ_{z_1} is used. It was determined from numerical experimentation that the initial core needs larger move-down movement in the z direction than the move-out movement in the y direction.

Second iteration

If the initial movement of the concentrated core is in the z direction, the y-coordinates of the core will be adjusted next in the second iteration. The computed lift coefficient after the initial adjustment of the concentrated core is denoted by C_L. The core will be caused to move out if C_L is greater than C_{L_s} and to move in if C_L is less than C_{L_s}. The corresponding relaxation parameter is:

$$\lambda_{y_2} = - \frac{(C_L - C_{L_s}) \, \text{Sin} \, \alpha}{C_{L_s}} \tag{86}$$

On the other hand, if the initial movement of the concentrated core is in the y direction, the z-coordinate of the core will be adjusted in the second iteration. The core will move down if C_L is less than C_{L_s} and move up if C_L is greater than C_{L_s}. The corresponding relaxation parameter is:

$$\lambda_{z_2} = 0.75 \, \frac{(C_L - C_{L_s})}{(C_{L_s} \, \text{Tan} \, \alpha)} \tag{87}$$

The relaxation parameters λ_{y_2} and λ_{z_2} have the same form as the initial set except the magnitude is reduced by half. Special conditions are imposed for all configurations when the angle of attack is below 20 degrees. They are (1) the magnitude of λ_{z_1} in equation (84) is to be reduced by half; and (2) for the angle of attack below 10 degrees, the angle of attack in equations (84) and (87) is set to 10 degrees to avoid the singularity in α in computing λ_{z_1} and λ_{z_2}. Therefore, the movement of the core in the first two iterations for angles of attack below 20 degrees will not cause a large fluctuation in the aerodynamic characteristics.

23

The relaxation parameters λ_y and λ_z of each segment of the core are to be used from the third iteration on, based on the force gradients of core segments before and after the adjustment of the free sheet vortex elements. Thus, the relaxation parameters to the ith segment of the core are:

$$\lambda_{y_i} = C_{y_i} \left(\frac{F_{y2} - F_{y1}}{|F_{y1}|} \right)_i \qquad , \qquad |C_{y_i}| = \frac{1}{2}\Sigma F \qquad (88)$$

$$\lambda_{z_i} = C_{z_i} \left(\frac{F_{z2} - F_{z1}}{|F_{z1}|} \right)_i \qquad , \qquad |C_{z_i}| = \Sigma F \qquad (89)$$

In the above, F_{y1}, F_{z1}, F_{y2} and F_{z2} are the segment forces of the core before and after the adjustment of the free sheet vortex elements, and ΣF is the algebraic sum of segment forces acting on the core after adjustment of free sheet vortex elements. The sign of C_{y_i} and C_{z_i} are determined so as to reduce the total force acting on the free sheet vortex elements.

In the core model, the locations of free sheet vortex elements and concentrated core have a very sensitive effect on wing loading. To avoid the divergence of the iteration procedure: (1) the restrictions are imposed on the movement of free sheet vortex elements and concentrated core as discussed in sections 3.5.2 and 3.5.3; (2) the end point of the first core segment near apex will remain fixed from the third iteration; and (3) the z-coordinates of concentrated core are not allowed to be below z_{min} given by equations (40 and (50).

3.9 Aerodynamic Characteristics

In reference 26, the more accurate expressions to calculate the overall aerodynamic characteristics are derived by Lan for the cambered wing. Both $\frac{\partial z_c}{\partial x}$ and $\frac{\partial z_c}{\partial y}$ are included in the computation.

Assume that the wing surface (Fig. 7) can be described by:

$$z = z_c(x,y) \tag{90}$$

where $z_c(x,y)$ is the ordinate of camber surface measured from the x-y plane. Introduce a function f such that:

$$f = z - z_c(x,y) \tag{91}$$

Therefore, a unit normal vector on the wing surface can be defined as:

$$\vec{n} = \frac{\vec{\nabla}f}{|\vec{\nabla}f|} = \frac{-\frac{\partial z_c}{\partial x}\vec{i} - \frac{\partial z_c}{\partial y}\vec{j} + \vec{k}}{\left[1 + (\frac{\partial z_c}{\partial x})^2 + (\frac{\partial z_c}{\partial y})^2\right]^{\frac{1}{2}}} \tag{92}$$

The unit vectors $\vec{n}_\infty$ and $\vec{t}_\infty$ are related with $\vec{n}$ (Fig. 8) in the following expressions:

$$\vec{n}_\infty = -\text{Sin } \alpha \, \vec{i} + \text{Cos } \alpha \, \vec{k} \tag{93}$$

$$\vec{t}_\infty = \text{Cos } \alpha \, \vec{i} + \text{Sin } \alpha \, \vec{k} \tag{94}$$

The computed lifting pressure ΔC_p (see Appendix A) is acting normal to the local camber surface, i.e., in the $\vec{n}$ direction. Then, this pressure force can be decomposed into $\vec{n}_\infty$ and $\vec{t}_\infty$ directions to determine the lift and drag components, respectively. Hence, the component in the lift direction is:

$$\vec{n} \cdot \vec{n}_\infty = (\frac{\partial z_c}{\partial x} \text{Sin } \alpha + \text{Cos } \alpha)/\left[1 + (\frac{\partial z_c}{\partial x})^2 + (\frac{\partial z_c}{\partial y})^2\right]^{\frac{1}{2}} \tag{95}$$

the component in the drag direction is:

$$\vec{n} \cdot \vec{t}_\infty = (-\frac{\partial z_c}{\partial x} \text{Cos } \alpha + \text{Sin } \alpha)/\left[1 + (\frac{\partial z_c}{\partial x})^2 + (\frac{\partial z_c}{\partial y})^2\right]^{\frac{1}{2}}$$

To find the pitching moment about y axis, the $\vec{j}$ component of $(\Delta x \, \vec{i} + \Delta z \, \vec{k}) \times \vec{n}$ is needed, where Δx and Δz are the moment arms of the pressure elements referenced to the coordinate system. In the present analysis, Δz is assumed to be zero. Hence, the corresponding $\vec{j}$-component of $(\Delta x \, \vec{i} \times \vec{n})$ is:

$$-\Delta x / \left[1 + (\frac{\partial z_c}{\partial x})^2 + (\frac{\partial z_c}{\partial y})^2\right]^{\frac{1}{2}} \tag{97}$$

3.9.1 Sectional Aerodynamic Characteristics

To find the sectional characteristics, it is assumed that the wing vortices are situated along the cambered surface. Since the resulting lifting pressure is acting normal to the local camber surface, the sectional lift, induced drag and pitching moment coefficients can be determined by combining the lifting pressure ΔC_p and equations (95) to (97) through the local chord integration. Hence, the sectional lift, induced drag and pitching moment coefficients at the jth strip have the following expression:

$$c_{\ell_j} = \frac{1}{c_j} \int_{x_{\ell_j}}^{x_{t_j}} \Delta C_p \left(\frac{\partial z_c}{\partial x} \sin \alpha + \cos \alpha \right) \Big/ \left[1 + \left(\frac{\partial z_c}{\partial x} \right)^2 + \left(\frac{\partial z_c}{\partial y} \right)^2 \right]^{\frac{1}{2}} dx$$

$$+ c_{t_j} \left[\left(\frac{\partial z_c}{\partial x} \right)_j \sin \alpha + \cos \alpha \right]_{\ell_e} \Big/ \left[1 + \left(\frac{\partial z_c}{\partial x} \right)_j^2 + \left(\frac{\partial z_c}{\partial y} \right)_j^2 \right]_{\ell_e}^{\frac{1}{2}} \qquad (98)$$

$$c_{d_j} = \frac{1}{c_j} \int_{x_{\ell_j}}^{x_{t_j}} \Delta C_p \left(-\frac{\partial z_c}{\partial x} \cos \alpha + \sin \alpha \right) \Big/ \left[1 + \left(\frac{\partial z_c}{\partial x} \right)^2 + \left(\frac{\partial z_c}{\partial y} \right)^2 \right]^{\frac{1}{2}} dx$$

$$- c_{t_j} \left[-\left(\frac{\partial z_c}{\partial x} \right)_j \cos \alpha + \sin \alpha \right]_{\ell_e} \Big/ \left[1 + \left(\frac{\partial z_c}{\partial x} \right)_j^2 + \left(\frac{\partial z_c}{\partial y} \right)_j^2 \right]_{\ell_e}^{\frac{1}{2}} \qquad (99)$$

$$c_{m_j} = -\frac{1}{\bar{c} c_j} \int_{x_{\ell_j}}^{x_{t_j}} \Delta C_p \cdot (\Delta x) \Big/ \left[1 + \left(\frac{\partial z_c}{\partial x} \right)^2 + \left(\frac{\partial z_c}{\partial y} \right)^2 \right]^{\frac{1}{2}} dx \qquad (100)$$

where the c_{t_j} terms in equations (98) and (99) are the leading-edge suction effect; x_{ℓ_j} and x_{t_j} the leading-and trailing-edges x-coordinates of the chord passing through the control station of the jth strip; $\bar{c}$ the mean geometric chord, c_j the local chord length. The subscript ℓ_e, in equations (98) and (99), means $\left(\frac{\partial z_c}{\partial x} \right)_j$ and $\left(\frac{\partial z_c}{\partial y} \right)_j$ are evaluated at the leading-edge of the jth strip. Using this transformation,

$$x = x_{\ell_j} + \frac{c_j}{2} (1 - \cos \theta)$$

equation (98) can be reduced to:

$$c_{\ell_j} = \frac{1}{2} \int_0^{\pi} \Delta C_p \sin \theta \left(\frac{\partial z_c}{\partial x} \sin \alpha + \cos \alpha \right) \Big/ \left[1 + \left(\frac{\partial z_c}{\partial x} \right)^2 + \left(\frac{\partial z_c}{\partial y} \right)^2 \right]^{\frac{1}{2}} d\theta$$

$$+ c_{t_j} \left[\left(\frac{\partial z_c}{\partial x}\right)_j \sin \alpha + \cos \alpha \right] \Bigg/ \left[1 + \left(\frac{\partial z_c}{\partial x}\right)_j^2 + \left(\frac{\partial z_c}{\partial y}\right)_j^2 \right]_{\ell_e}^{\frac{1}{2}}$$

$$\cong \quad \frac{\pi}{2(N+1)} \sum_{k=1}^{N+1} \Delta C_{p_k} \left[\left(\frac{\partial z_c}{\partial x}\right)_k \sin \alpha + \cos \alpha \right] \sin \theta_k \Bigg/ \left[1 + \left(\frac{\partial z_c}{\partial x}\right)_k^2 + \left(\frac{\partial z_c}{\partial y}\right)_k^2 \right]^{\frac{1}{2}}$$

$$+ c_{t_j} \left[\left(\frac{\partial z_c}{\partial x}\right)_j \sin \alpha + \cos \alpha \right]_{\ell_e} \Bigg/ \left[1 + \left(\frac{\partial z_c}{\partial x}\right)_j^2 + \left(\frac{\partial z_c}{\partial y}\right)_j^2 \right]_{\ell_e}^{\frac{1}{2}} \qquad (101)$$

and

$$\theta_k = \frac{(2k - 1)\pi}{2(N + 1)} \quad , \quad k=1, \text{---} \ (N + 1)$$

where the mid-point trapezoidal rule has been used to reduce the integral into a finite sum (ref. 19). Similarly, the sectional induced drag and pitching moment coefficients for the jth strip are given by:

$$c_{d_j} \cong \frac{\pi}{2(N + 1)} \sum_{k=1}^{N+1} \Delta C_{p_k} \left[-\left(\frac{\partial z_c}{\partial x}\right)_k \cos \alpha + \sin \alpha \right] \sin \theta_k \Bigg/ \left[1 + \left(\frac{\partial z_c}{\partial x}\right)_k^2 \right.$$

$$\left. + \left(\frac{\partial z_c}{\partial y}\right)_k^2 \right]^{\frac{1}{2}} - c_{t_j} \left[-\left(\frac{\partial z_c}{\partial x}\right)_j \cos \alpha + \sin \alpha \right]_{\ell_e} \Bigg/ \left[1 + \left(\frac{\partial z_c}{\partial x}\right)_j^2 + \right.$$

$$\left. \left(\frac{\partial z_c}{\partial y}\right)_j^2 \right]_{\ell_e}^{\frac{1}{2}} \qquad (102)$$

$$c_{m_j} \cong - \frac{\pi}{2\bar{c}(N + 1)} \sum_{k=1}^{N+1} \Delta C_{p_k} \left[x_{\ell_j} + \frac{c_j}{2}(1 - \cos \theta_k) \right] \sin \theta_k \Bigg/ \left[1 + \left(\frac{\partial z_c}{\partial x}\right)_k^2 + \right.$$

$$\left. \left(\frac{\partial z_c}{\partial y}\right)_k^2 \right]^{\frac{1}{2}} \qquad (103)$$

According to equations (52) and (53) of reference 19, the sectional leading-edge thrust coefficient is given by:

$$c_{t_j} = \frac{\pi (1 - M_\infty^2 \cos^2 \Lambda)^{\frac{1}{2}} \left[w_j' - \left(\cos \alpha \left(\frac{dz}{dx}\right)_j - \sin \alpha\right) \right]^2}{2N^2 \cos \Lambda \ (1 - M_\infty^2 + \tan^2 \Lambda)} \qquad (104)$$

where M_∞ is the free stream Mach number; Λ the sweep angle of the leading-edge; w_j' and $\left(\frac{dz}{dx}\right)_j$ are the induced normalwash and slope of the wing surface at the leading-edge. For sharp-edged wings, c_t is assumed zero.

27

3.9.2 Overall Aerodynamic Characteristics

The total induced drag, lift, pitching moment and leading-edge thrust coefficients of the wing are determined by spanwise integration of the sectional characteristics. Again, the integration is first transformed to an angular coordinate ($0 \leq \phi \leq \pi$), and then reduced to finite sum by the conventional trapezoidal rule (ref. 19). Therefore, the total lift coefficient has the following expression,

$$C_L = \frac{2}{S} \int_0^{b/2} c_\ell c \, dy \tag{105}$$

where b is the wing span and S the wing area. By the transformation:

$$y = \frac{b}{4} \ (1 - \cos \phi) \tag{106}$$

equation (105) can be reduced to:

$$C_L = \frac{b}{2S} \int_0^\pi c_\ell \ c \sin \phi \ d\phi$$

$$\simeq \frac{b\pi}{2SM} \sum_{i=1}^{M-1} c_{\ell_i} \ c_i \sin \phi_i \tag{107}$$

and

$$\phi_i = \frac{i}{M}\pi \quad , \quad i=1,---(M-1)$$

where M-1 is the total number of spanwise strips.

Similarly, the induced drag, pitching moment and leading-edge thrust coefficients are given by:

$$C_{D_i} \simeq \frac{b\pi}{2SM} \sum_{i=1}^{M-1} c_{d_i} \ c_i \sin \phi_i \tag{108}$$

$$C_m \simeq \frac{b\pi}{2SM} \sum_{i=1}^{M-1} c_{m_i} \ c_i \sin \phi_i \tag{109}$$

$$C_T \simeq \frac{b\pi}{2SM} \sum_{i=1}^{M-1} c_{t_i} \ c_i \sin \phi_i \tag{110}$$

3.10 Summary of Solution Procedures

In the diffused vortex filament model of Mehrotra (ref. 18), the basic unknowns of the problem are the bound vortex density on the wing, the strengths and locations of the elements of the leading-edge vortex system and the

28

trailing wake. The problem is solved in the following iterative manner:

(a) Prescribe the vortex-lattice for the wing surface, and the
    initial locations of the leading-edge and side-edge free
    elements over the wing and in the wake.

(b) By satisfying the wing boundary condition, equation (37), ob-
    tain the bound vortex density of the wing and the strengths of
    free elements.

(c) Calculate the aerodynamic characteristics and loads.

(d) Adjust the free elements of the leading- and side-edges vortex
    system and the trailing wake in the local velocity vector dir-
    ection.

(e) Repeat steps (b) through (d) for two iterations.

After two iterations in Mehrotra's diffused vortex filament model, the
present model with the leading-edge vortex core is then introduced (See Fig. 9).
In the core model, the basic unknowns of the problem are the bound vortex
density on the wing, the strengths and locations of the free sheet vortex
elements, the concentrated core and the trailing wake. The problem is still
solved in the iterative manner:

(f) Find the centroid of the established leading-edge vortex
    filament system, equations (81) and (82), from step (e).

(g) Allow the leading-edge vortex elements to merge and feed
    vorticity into the concentrated core through connecting
    segments.

(h) From the numerical experimentation, the z-coordinate of the
    initial core is modified by equation (83), and the y-coordinate
    of the initial core is adjusted so that the initial core
    location is at least 60 percent of the local semi-span
    of the wing to have a better starting solution.

29

(i) By satisfying the wing boundary condition, equation (37),
the initial bound vortex density of the wing and the
strength of free vortex elements are obtained.

(j) In the first two iterations of core model, the core is
forced to move either in the y or z direction. The dir-
ection depends upon the sign and the difference between
the initially computed lift coefficient and the reference
lift coefficient based on the suction analogy. The relax-
ation parameters λ_y and λ_z are based on equations (84)
through (87).

(k) From the third iteration of the core model, the movement of
the core is based on the relaxation parameters for each seg-
ment of the core, equations (88) and (89). These are used
to keep the core moving in a direction for which the total
algebraic sum of the forces acting on the free sheet is to
be decreased.

(l) Based on step (k), the orientation of the leading-edge free
elements of the free vortex sheet, side-edge vortices, the
concentrated core and the trailing wake are adjusted in the
local velocity vector direction.

(m) By satisfying the wing boundary condition, equation (37),
the bound vortex density of the wing and the strength of
free elements are obtained.

(n) Calculate all the aerodynamic characteristics and loads.

(o) Calculate the force acting on all free elements of the free
vortex sheet over the wing surface and the concentrated core.

(p) Repeat steps (j) through (o) until a converged solution is
obtained.

The converged positions and orientations for the free sheet vortex elements, side-edge vortex elements, and the concentrated core are assumed to have occurred when the sum of the magnitude of the total force acting on the core and free sheet has reached a local minimum value in the iteration cycle.

Numerical results to date indicate that when the angle of attack is decreased below 20 degrees, the present method has difficulty in generating a satisfactory starting solution. The main reason is the poor initial shape of the free vortex sheet from   Mehrotra's model. Thus, with the core model method, the starting solution for wings at angles of attack less than 20 degrees is taken to be the initial shape for 20 degrees angle of attack.

31

4. Numerical Results and Discussions

This section presents numerical characteristics of and predictions by the present method. These predictions are compared with results from the methods of Mehrotra (ref. 18), Johnson, et al. (refs. 13 and 14) (called Free Vortex Sheet (FVS)), Lan (ref. 26), Lamar (ref. 27) (called Vortex-lattice Method based on Suction Analogy (VLM-SA)) and with data. Numerical characteristics and results of the present method will be presented and discussed next.

4.1 Numerical Characteristics

The numerical results predicted by the present method have the following numerical characteristics:

(a) Convergence Characteristics

In the present method, numerical convergence can be expected during the iteration process if certain restrictions are imposed on the movements of the free sheet and vortex core (see sections 3.5 and 3.8).

(b) Initial Vortex Shape

For the angle of attack below 20 degrees, the starting solution is taken to be the initial vortex shape from the 20 degrees angle of attack solution.

(c) Spanwise Strips

In reference 18, Mehrotra made a parametric study to find a relation between the aspect ratio and the number of spanwise strips which should be used to represent the lifting pressure on delta wings in order to obtain reasonably accurate aerodynamic results. The relation just mentioned is reproduced and displayed graphically in Fig. 10. From this figure eight vortex strips over the wing semi-span are seen to be needed for simple deltas in the aspect ratio range from 1.0 to 1.75. Because of this study and because of the strake-wing and double delta configurations to be treated here being also of low aspect ratio, the same number was used initially.

32

Due to the leading-edge kink these configurations had to be represented by two spanwise regions per semi-span. Experience with the QVLM of Lan's (ref. 19) has shown that for two spanwise region solutions, it is better to have a different number of spanwise strips in each region. The final choice of spanwise strips used here is four for the strake region and five for the wing region.

(d) Chordwise Vortex Elements

All results to be presented have been calculated by using six chordwise vortex elements for all configurations.

(e) Reference Lift Coefficient

The reference lift coefficient discussed previously (see section 3.8) for use in adjusting the core movement is based on the suction analogy as implemented by Lan (ref. 26).

(f) Complete Leading-Edge Separation

In this study, only wings having complete leading-edge separation will be considered.

4.2 Numerical Results

This section presents numerical results by the present method based on the preceding ideas. These results are compared with other methods and data for certain test configurations which are shown in Figs. 11 to 15. Note that they consist of a flat delta wing (Fig. 11), a conical cambered delta wing (Fig. 12), a delta wing with leading-edge vortex flap (Fig. 13), a double delta wing (Fig. 14) and a strake wing (Fig. 15). The one vortex core system is used for the delta wings while the two vortex-core system is used for the others.

Overall Forces and Moments

The overall aerodynamic characteristics are presented in Figs. 16 to 20.

33

All theoretical curves for the results generated are graphed by fairing
through those at the α's given in the following table.

Method	Solution α's
Present method	
Flat delta wing	5°, 10°, 20.4°, 30.7°
Conical cambered delta	5°, 10°, 20.4°, 30.7°
Delta wing with LEVF	5°, 10°, 20°, 24°
Double delta wing	5°, 10°, 20°, 28°
Strake Wing	5°, 10°, 21.6°, 27.7°
Mehrotra	5°, 10°, 15°, 20°, 25°, 30°
Lan	All α's
VLM-SA	All α's
FVS	10°, 15°, 20°, 25°, 30°

Delta Wing

(a) Planar

The results for the flat delta wing are shown in Fig. 16. It is seen
that C_L and C_{D_i} can be accurately predicted by the present method as well as
by the other methods. However, the present method predicts the C_m to be
more positive (i.e. more nose up) at high angles of attack, whereas the
methods of VLM-SA and Lan predict more nose down pitching moment. This
nose up moment of the present method could be due to the estimated peak
load being too forward. Mehrotra's results have good agreement with data
(ref. 22) even though he used a diffused vortex model.

(b) Conical camber

The results for a conical cambered delta wing are presented in Fig. 17.
The C_L results from Lan's method have the best agreement with data. The C_L
results are underpredicted by the present method at lower angles of attack

34

and by the VLM-SA at higher angles of attack. FVS results (ref. 30) are generally low. The C_{D_i} results of Fig. 17(b) show that the FVS method is best at angles of attack below 20 degrees and the present method is best for angles of attack above 20 degrees. The other methods all predict values of C_{D_i} which are too low over the angle of attack range. Similar to the case for the flat delta, the present method predicts a pitch up tendency for the cambered wing.

(c) Leading-edge vortex flap

Recently, there has been much interest in applying the leading-edge vortex flap to increase the lift-drag ratio under maneuvering conditions. Some low speed results for a 74°-delta wing have been reported in reference 29. The geometry of the planform is shown in Fig. 13 and it was modeled theoretically with its undeflected trailing-edge flap omitted for simplicity. The results are presented in Fig. 18 where the C_L, C_{D_i} and C_m have been based on the total planform area excluding the leading-edge flap. It is seen that the predicted results by the methods of Lan and VLM-SA agree well with data. The C_L and C_{D_i} results estimated by the presented method slightly exceed the values of the data at moderate angles of attack. The C_m results show the present method to have a more nose up moment than the data for angles of attack above 12 degrees.

Having compared the results in the one vortex-core system, it is of interest to see the aerodynamic characteristics in the two vortex-core system.

Double Delta Wing

For the double delta wing (ref. 28), the comparison is made in Fig. 19. The results show that the C_L and C_{D_i} are well predicted by the present method and the methods of Lan and VLM-SA. At high angles of attack the present method predicts the C_m results better than others.

35

Strake Wing

From reference 28, it is understood that the aerodynamic advantage of strake-wing planforms are (1) the transonic maneuvering capability, and (2) the utilization of vortex lift. For the strake-wing configuration of Fig. 15 (ref. 31), the results are presented in Fig. 20. It is seen that the C_L predicted by the present method has good agreement with data whereas the method of Lan overpredicts the data in the high angle of attack region. The experimental data in Fig. 20(b) shows that the pitching moments become more positive as the angle of attack is increased. This could be due to the wing vortex breakdown on the main wing. From the geometry of strake wing in Fig. 15, it can be seen that the wing area is much larger than the strake. As shown in the data in Fig. 20(a), the C_L values start to decrease at about 14 degrees of angle of attack, signifying the start of the wing vortex bursting.

Lifting Pressure Distribution

Figs. 21 through 29 show the spanwise pressure distributions for different planforms at specified angles of attack and for constant x-locations. The results are discussed below.

Delta Wing

(a) Planar

For the flat delta wing, the spanwise pressure distributions are calculated at angles of attack equal to 10.2°, 20.4° and 30.7°, and compared with data at the two x-locations, $x/c_R = 0.5333$ and 0.9333 in Figs. 21 to 23. In general, the pressure peak obtained by using Mehrotra's method is lower than the data near midchord, higher near the trailing-edge and is shifted toward the root chord. One objective in the present method is to improve the pressure distribution of Mehrotra's method, so as to allow for the occurrence of a sharper pressure peak. The predicted pressure distributions

36

of the present method more closely resemble the data than do those of Mehrotra. At the low angle of attack ($\alpha = 10.2^{\circ}$), the present method predicts a pressure peak that is inboard of the data at midchord and is lower near the trailing-edge. This may be due to the free sheet being too large, since its initial shape and core location is taken from the 20-degree solution and the size of free sheet will not shrink in the iteration process. Thus, the inboard pressure distribution are higher than those measured.

(b) Conical camber

The results of the estimated spanwise pressure distribution for the conical cambered delta are presented in Figs. 24 through 26, and are compared with data (ref. 22) and the FVS solution (ref. 30). Again, the presented results are at the angles of attack equal to 10.2°, 20.4° and 30.7° and comparisons are made at two x-locations, $x/c_R = 0.67$ and 0.935. At low and moderate angles of attack, the present method predicts values of the pressure peak which are lower than data, whereas the FVS solution predicts higher peaks. At high angles of attack the spanwise pressure distribution predicted by the present method has better agreement with data than does the FVS solution. There are two pressure peaks near the trailing-edge at all angles of attack. The inboard peak is expected and is typical for flat delta configurations. However, the reason for the outboard peak is not conclusively known. Some possible reasons for its occurrence are as follows: (1) the wing vortex distribution is not located on the highly cambered surface; instead, it is on a flat surface; (2) the large spanwise camber slope term ($\partial z/\partial y = -1.4402$) near leading-edge is not included in the boundary condition; (3) eight spanwise strips may not be sufficient to resolve the lifting pressures in the tip region of this conically cambered wing.

(c) Leading-edge vortex flaps

Spanwise pressure distributions predicted by the present method at 24-de-

gree angle of attack and two x-locations, x/c_R = 0.5197 and 0.8937, are presented in Fig. 27 for a 74°-delta wing with leading-edge vortex flap. Since there are no data or other theoretical results available, only the present theoretical results are presented on each figure.   Fig. 27(a) shows that the pressure peak is at about 60 percent of the local semispan and that matches the vortex core location. Near the trailing-edge the interaction of the vortex core and leading-edge vortex flap produces large lifting pressure in the vortex flap region as seen in Fig. 27(b).

Double Delta Wing

From Fig. 28, the spanwise pressure distribution at 20-degree angle of attack at two x-locations, x/c_R = 0.5686 and 0.8099 are presented. In Fig. 28(a), the results near middle root chord indicate that there are two pressure peaks present. The lower pressure peak is behind the highly swept inboard region with the higher pressure peak being on the outboard wing region. The two vortex cores induce large sidewash in the tip region which result in a large pressure peak there. Fig. 28(b) shows the lifting pressures near the trailing-edge and from this figure it is seen that another pressure peak has been produced. This outboard peak may be due to the large sidewash induced near the tip due to the interacting inboard-located vortex cores. The exact reasons for this require additional investigation.

Strake Wing

From Fig.29, the spanwise pressure distribution at an angle of attack of 12 degrees at three constant chord stations, x/c = 0.4, 0.7 and 0.9, are presente. In Fig.29(a), the results near the kink region show that the lifting pressure are mainly from strake vortex. In Figs.29(a) to 29(c), the predicted pressure distributions are generally higher than experimental values. the large pressure peak near the tip region of each figure is mainly due to the

effect of side-edge vortex system. Near the trailing edge the flow field is dominated by the wing with most of the predicted lifting pressure being on the wing. It should be noted that at an angle of attack of about $14°$, the wing vortex breakdown may have occurred (ref. 37). The effect of vortex breakdown is not modelled in the present method.

For a slender delta wing, a typical computer CPU time by the present method is 3230 seconds in 7 iterations with CDC Cyber 175 at Langley Research Center. This is to be compared with 4540 seconds in 10 iterations by Mehrotra's model. For the double delta wing analyzed in this report, the CPU time is 5620 seconds in 8 iterations as compared with 22,450 seconds in 8 iterations by the Boeing code (Ref.14). If the first two iterations in Mehrotra's model can be by-passed by directly assuming a reasonable initial configuration, the saving in CPU time is about 1200 seconds for simple delta configurations.

4.3 Mean Square Error Computation.

To check the accuracy of the results predicted by the present and other theoretical methods, the so-called mean square error (MSE) will be used. Mean square error is defined as:

$$MSE = \left[(\sum_{i=1}^{K}(d_i' - d_i)^2)/K \right]^{1/2} \tag{111}$$

where d_i is the i th experimental data value, K the total number of data points, and d_i' the interpolated theoretical results at the location of data point d_i. Thus, the typical results of mean square error of each theoretical method to the overall lift coefficient and lifting pressure distributions are as shown in the following:

MSE for Overall Lift Coefficient

(a)   a flat delta wing (Fig. 16(a))

Present Theory	0.0209
Lan's Method	0.0172
VLM-SA	0.0045
Mehrotra's Method	0.0242

(b) a conically cambered wing (Fig. 17(a))

 Present Theory   0.0407

 Lan's Method   0.0237

 VLM-SA   0.0423

 FVS Method   0.0470

(c) a delta wing with L. E. vortex flap (Fig. 18(a))

 Present Theory   0.0405

 Lan's Method   0.0378

 VLM-SA   0.0628

(d) a double delta wing (Fig. 19 (a))

 Present Theory   0.0351

 Lan's Method   0.0330

 VLM-SA   0.0534

(e) a strake-wing configuration (Fig.20(a))

 Present Theory   0.0724

 Lan's Method   0.1197

MSE for Lifting Pressure Distribution

Configuration		x/c_R	α, deg.	Present Method	Mehrotra
Flat Delta,	Fig. 21(a)	0.5333	10.2	0.1694	0.1198
" "	Fig. 21(b)	0.9333	10.2	0.1391	0.1539
" "	Fig. 22(a)	0.5333	20.4	0.2642	0.3804
" "	Fig. 22(b)	0.9333	20.4	0.1060	0.1906
" "	Fig. 23(a)	0.5333	30.7	0.5011	0.7773
" "	Fig. 23(b)	0.9333	30.7	0.1496	0.4111

Configuration		x/c_R	α, deg.	Present Method	FVS Method
Delta with Conical Camber,	Fig. 24(a)	0.67	10.2	0.1540	0.1744
"	Fig. 24(b)	0.935	10.2	0.1470	0.2163
"	Fig. 25(a)	0.67	20.4	0.3146	0.3027
"	Fig. 25(b)	0.935	20.4	0.1690	0.1358
"	Fig. 26(a)	0.67	30.7	0.5090	0.4868
"	Fig. 26(b)	0.935	30.7	0.1491	0.3139

For the flat delta wing, the mean square errors for the lifting pressure indicate that the present theory is better than Mehrotra's model. For a delta wing with the conical camber, the present results are also good. However, the lower values of MSE of present results partially may be due to the appearance of an unexpected pressure peak near the tip region.

5. Concluding Remarks

A free sheet-vortex core model to predict pressure loadings and overall aerodynamic characteristics of low aspect-ratio wings with edge vortex separation has been developed, by incorporating a vortex core in the free sheet of Mehrotra's method. In the present method, Mehrotra's model is used in the first two iterations to establish the vortex filament system. Based on Smith's empirical results, the initial vortex core location is adjusted to improve the starting solution. Introduction of a vortex core in the flow model increases the numerical difficulty to obtain a converged solution. The problem is solved by using different sets of relaxation parameters for and by imposing certain restrictions on movements of the free sheet and the vortex core. For low to moderate angles of attack ($\alpha < 20°$), the starting solution is taken to be the initial shape of the 20-degree angle of attack solution.

Comparison with available data indicates that: (1) the present method is generally accurate in predicting the lift and induced drag coefficients but the predicted pitching moment is too positive; (2) the spanwise lifting pressure distributions estimated by the one vortex core solution of the present method are significantly better than the results of Mehrotra's method relative to the pressure peak values for the flat delta; (3) the two vortex-core system applied to the double delta and strake-wing produces overall aerodynamic characteristics which have good agreement with data except for the pitching moment; (4) the computer time for the present method is about two thirds of that of Mehrotra's method for a delta wing and one quarter of that of FVS method for a double delta wing configuration.

In view of the improvements embodied in the present method and possible further refinement, it would be of interest to:

42

(1) model the fuselage portion as a potential flow region, with the assumption of attached flow in the fuselage region and a very small thrust coefficient being assumed in that region;

(2) examine the fuselage effect on wing vortex flow;

(3) examine the canard effect on wing vortex flow;

(4) compare the chordwise pressure distribution with available data to improve the pitching moment computation.

6. References

(1). Legendre, R., "E'coulement an voisinage de la pointe avante d'une aile à forte flèche aux incidences moyennes", Rechere Aéronautique (O.N.E.R.A.), No. 30, pp. 3-8, 1952.

(2). Brown, C.E. and Michael, W.H., "On Slender Delta Wings with Leading-Edge Separation", NACA TN 3430, 1955.

(3). Mangler, K.W. and Smith, J.H.B., "A Theory of the Flov Past a Slender Delta Wing with Leading-Edge Separation", Proc. Roy. Soc. A251, pp. 200-217, 1959.

(4). Smith, J.H.B., "Improved Calculation of Leading-Edge Separation for Slender, Thin, Delta Wings", Proc. Roy. Soc. A 306, pp. 69-90, 1968.

(5). Bollay, W., "A Non-Linear Wing Theory and Its Application to Rectangular Wings of Small Aspect Ratio", Journal of the Aeronautical Science, Vol. 4, pp. 294-296, 1937.

(6). Geroten, K., "Calculation of Non-Linear Aerodynamic Stability Derivatives of Aeroplanes", AGARD Report 342, April 1961.

(7). Garner, H.C. and Lehrian, D.E., "Non-Linear Theory of Steady Forces on Wings with Leading-Edge Separation", ARC R & M 3375, 1963.

(8). Multhopp, H., "Method for Calculating the Lift Distribution of Wings (Subsonic Lifting Surface Theory)", ARC R & M 2884, 1950.

(9). Nangia, R.K. and Hancock, G.J., "A Theoretical Investigation for Delta Wings with Leading-Edge Separation at Low Speeds", ARC CP-1086, 1968.

(10). Polhamus, E.C., "A Concept of the Vortex Lift of Sharp-Edge Delta Wings Based a Leading-Edge-Suction Analogy", NASA TN D-3767, 1966.

(11). Matoi, T.K., "On the Development of a Unified Theory for Vortex Flow Phenomena for Aeronautical Applications", AD-A012399, April 1975.

44

(12). Parker, A.G., "Aerodyanmic Characteristics of Slender Wings with
Sharp Leading-Edges - A Review", Journal of Aircraft, Vol. 13,
No. 3, pp. 161-168, March 1976.

(13). Brune, G.W., Weber, J.A., Johnson, F.T., Lu, P. and Rubbert, P.E.,
"A Three Dimensional Solution of Flow over Wings with Leading-
Edge Separation", AIAA Journal, Vol. 14, pp. 519-525, April 1976.

(14). Johnson, F.T., Tinoco, E.N., Lu, P. and Epton, M.A., "Recent Advances
in the Solution of Three-Dimensional Flows over Wings with Leading-
Edge Vortex Separation", AIAA Paper 79-0282, 1979.

(15). Hoeijmakers,H.W.M. and Bennekers, B., "A Computational Model for
the Calculation of the Flow about Wings with Leading-Edge Vortices",
AGARD CP-247, October 1978.

(16) Mook, D.T. and Maddox, S.A., "Extension of a Vortex-Lattice Method
to Include the Effects of Leading-Edge Separation", Journal of
Aircraft, Vol. 11, pp. 127-128, Feb. 1974.

(17). Kandil, O.A., Mook, D.T. and Nayfeh, A.H., "Nonlinear Prediction of
the Aerodynamic Loads on Lifting Surfaces", Journal of Aircraft,
Vol. 13, pp. 22-28, January 1976.

(18). Mehrotra, S.C. and Lan, C.E., "A Theoretical Investigation of the
Aerodynamics of Low-Aspect-Ratio Wings with Partial Leading-Edge
Separation", NASA CR-145304, January 1978.

(19). Lan, C.E., "A Quasi-Vortex-Lattice Method in Thin Wing Theory",
Journal of Aircraft, Vol. 11, No. 9, pp. 518-527, Sept. 1974.

(20). Kandil, O.A., Mook, D.T. and Nayfeh, A.H., "New Convergence Criteria
for the Vortex-Lattice Models of the Leading-Edge Separation",
NASA SP-405, pp. 285-300, May 1976.

(21). Fink, P.T., "Wind-Tunnel Tests on a Slender Delta Wing at High Incidence", Z. Flugwissenschaften, Jahrg. 4, Heft 7, pp. 247-249, July 1956.

(22). Wentz, W.H., "Effects of Leading-Edge Camber on Low-Speed Characteristics of Slender Delta Wings", NASA CR-2002, 1972.

(23). Bartlett, G.E. and Vidal, R.J., "Experimental Investigation of Influence of Edge Shape on the Aerodynamic Characteristics of Low Aspect Ratio Wings at Low-Speeds", Journal of the Aeronautical Sciences, Vol. 22, No. 8, pp. 517-533, August 1955.

(24). Fink, P.T. and Taylor, J., "Some Low-Speed Experiments with 20 deg. Delta Wings", ARC R & M 3489, 1367.

(25). Marsden, D.J., Simpson, R.W. and Rainbird, W.J., "The Flow over Delta Wings at Low Speeds with Leading-Edge Separation", The College of Aeronautics, Cranfield, Rept. No. 114, Feb. 1958.

(26). Lan, C.E. and Chang, J.F., "Calculation of Vortex Lift Effect for Cambered Wings by Suction Analogy", NASA CR-3449, 1981.

(27). Lamar, J.E. and Gloss, B.B., "Subsonic Aerodynamic Characteristics of Interacting Lifting Surfaces with Separated Flows around Sharp Edges Predicted by a Vortex Lattice Method", NASA TN D-7921, 1975.

(28). Lamar, J.E., "Analysis and Design of Strake-Wing Configuration", Journal of Aircraft, Vol. 17, No. 1, pp. 20-27, January 1980.

(29). Rao, D.M., "Leading-Edge Vortex Flap Experiments on a 74 Deg. Delta Wing", NASA CR-159161, November 1979.

(30). Kuhlman, J.M., "Analytical Studies of Separated Vortex Flow on Highly Swept Wing", NASA CR-3022, November 1978.

46

(31). White, R.P. Jr., "Prediction and Measurement of the Aerodynamic
      Forces and Pressure Distributions of Wing-Tail Configurations at
      Very High Angle of Attack", AGARD CP-247, October 1978.

(32). Harder, R.L. and Desmarais, R.N., "Interpolation Using Surface
      Splines", Journal of Aircraft, Vol. 9, pp. 189-191, February 1972.

(33). Bois, G.P., "Tables of Indefinite Integrals", Dover Publication Inc.,
      New York.

(34). Lamb, H., "Hydrodynamics , 6th ed. Dover, New York.

(35). Steger, J.L. and Kutler, P., "Implicit Finite-Difference Procedures
      for the Computation of Vortex Wakes", AIAA Journal, Vol. 15, pp.
      581-590, April 1977.

(36). Wedemeyer, E.H., "Stable and Unstable Vortex Separation", AGARD
      CP-247, October 1978.

(37). White, R.P. Jr., "An Experimental Investigation of Vortex flow Control
      for High Lift Generation", ONR CR 212-223-2, December,1975.

Appendix A

An Improved Lifting Pressure Expression

From reference 18, it is understood that the total lifting pressure, for the wing with leading-edge vortex element system, is contributed by wing bound elements, wing streamwise vortices, leading-edge bound elements and the streamwise vortices of the leading-edge vortex element system. Hence, the total lifting pressure at the ith bound element of the jth strip control station has the following expression:

$$\Delta C_{p_{j,i}} = (\Delta C_{p_{j,i}})_T + (\Delta C_{p_{j,i}})_B \tag{A.1}$$

where $(\Delta C_{p_{j,i}})_T$ is the lifting pressure due to streamwise vortices; $(\Delta C_{p_{j,i}})_B$ the lifting pressure due to bound elements.

A.1 Derivation of $(\Delta C_{p_{j,i}})_T$

From Fig. Al, it is clear that the lifting pressure due to streamwise vortices of wing and leading-edge vortex element are calculated along the common edge y_j of two adjoined spanwise strips. First, the force acting on the chordwise element of length Δx of the leading-edge vortex system is:

$$F_i = \rho \, V_\infty^2 \, (\Gamma_j \, v_i) \, \Delta x \tag{A.2}$$

where ρ is the fluid density, V_∞ the free stream velocity, Γ_j the vortex strength of the jth leading-edge vortex element, and v_i the sidewash at point i. Thus, the force acting at the ith point on the common edge per unit dynamic pressure and length is:

$$(\frac{F}{q\Delta x})_i = 2 \, \Gamma_j \, v_i \tag{A.3}$$

where q is the dynamic pressure. Similarly, the force acting at the same point due to the right leg of the jth strip, per unit dynamic pressure and length, can be written as:

$$(\frac{F_R}{q\Delta x})_i = -2 \, v_i \int^{x_\ell} \gamma dx \tag{A.4}$$

48
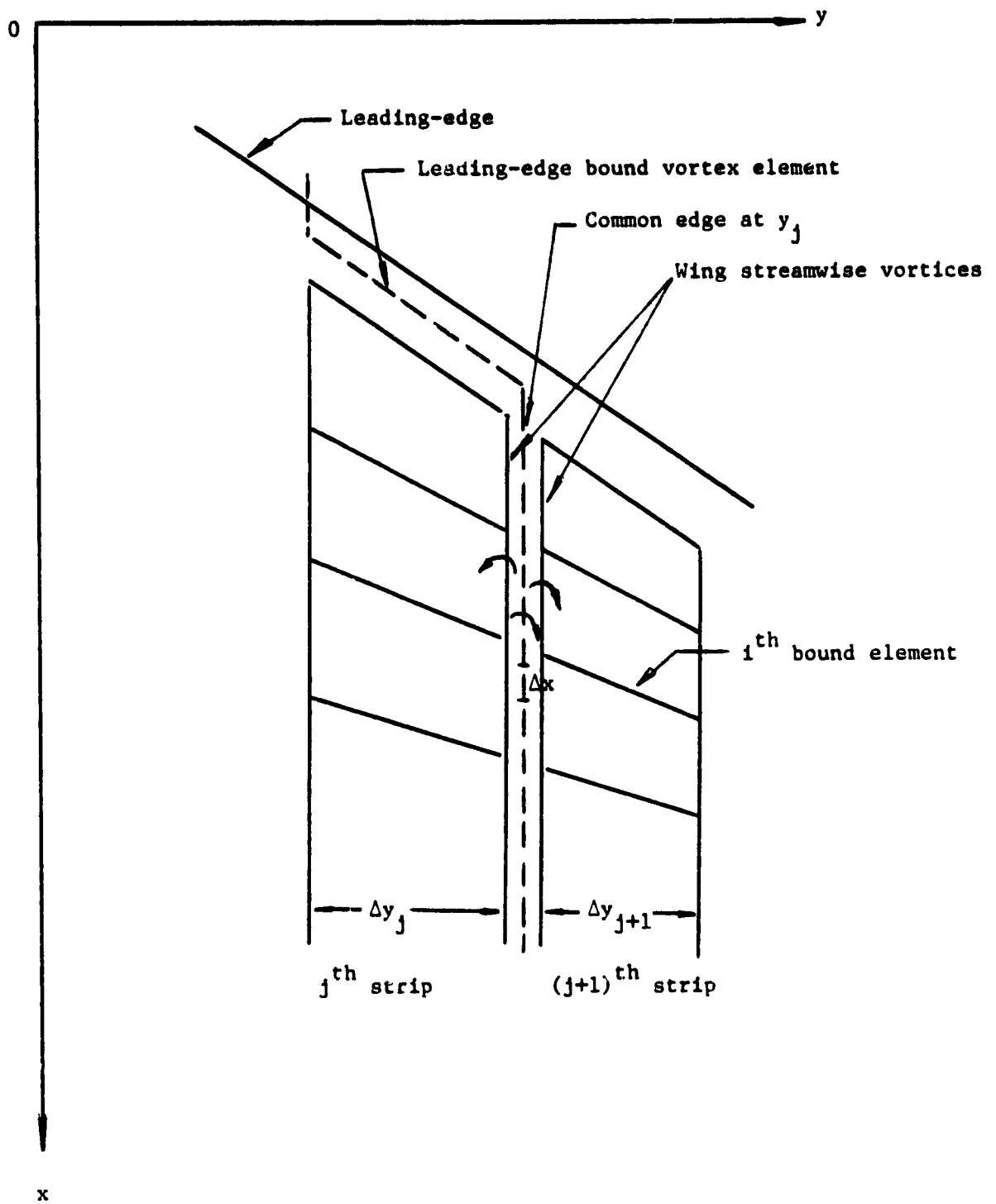
Figure A1.- The leading-edge bound vortex element and wing streamwise
vortices at the common edge y_j

49

where γ is the wing bound vortex density, x_ℓ the leading-edge x-coordinate of the trailing leg under consideration. Using the transformation,

$$x = x_\ell + \frac{c_j}{2} (1 - \cos \theta) \tag{A.5}$$

the equation (A.4) can be reduced to the form:

$$\left(\frac{F_R}{q\Delta x}\right)_i = -v_i c_j \int_0^{\theta_i} \gamma \sin \theta \, d\theta$$

$$\approx -\frac{\pi c_j v_i}{N} \left[\sum_{k=1}^{i-1} \gamma_k \sin \theta_k + \tfrac{1}{2} \gamma_i \sin \theta_i \right] \tag{A.6}$$

where c_j is the local chord length of the common edge at y_j, N the number of bound elements in chordwise direction and $\theta_k = \frac{(2k - 1)\pi}{2N}$. The integral has been reduced to a finite sum through the conventional trapezoidal rule.

For the left leg of the $(j+1)^{th}$ strip:

$$\left(\frac{F_L}{q\Delta x}\right)_i = \frac{\pi c_j v_i}{N} \left[\sum_{k=1}^{i-1} \gamma_k \sin \theta_k + \tfrac{1}{2} \gamma_i \sin \theta_i \right] \tag{A.7}$$

Therefore, the force per unit dynamic pressure and per unit length at the ith point along the jth common edge is:

$$\left(\frac{F_T}{q\Delta x}\right)_i = \left(\frac{F}{q\Delta x}\right)_i + \left(\frac{F_R}{q\Delta x}\right)_i + \left(\frac{F_L}{q\Delta x}\right)_i \tag{A.8}$$

Thus, the lifting pressure at i^{th} point along the jth common edge other than the last one has the following expression:

$$\left(\Delta C_{P_{j,i}}\right)'_T = 2 \left(\frac{F_T}{q\Delta x}\right)_i / (y_{j+2} - y_j) \tag{A.9}$$

When the lifting pressure is calculated at the last common edge in the spanwise direction, the equation has the following form:

$$\left(\Delta C_{P_{j,i}}\right)' = \left(\frac{F_T}{q\Delta x}\right)_i / (y_{j+1} - y_j) \tag{A.10}$$

where y_{j+2}, y_{j+1} and y_j are the y-location of common edges. Note that equations (A.9) and (A.10) are evaluated at all endpoints of wing bound elements, i.e. along the common edge. Surface spline interpolation (ref. 32) is performed to obtain the lifting pressure at the control station of each

50

vortex strip. Therefore, $(\Delta C_{p_{j,i}})_T$, the lifting pressure due to streamwise vortices at the ith bound element of the jth strip control station is obtained.

A.2 Derivation of $(\Delta C_{p_{j,i}})_B$

From Fig. A2, the normal force per unit length acting at the ith bound element of the jth strip is given by:

$$F_{B_{j,i}} = \rho \, V_\infty^2 \, (u_i \, \gamma_y - v_i \, \gamma_x) \, \Delta S_i$$

$$= \rho \, V_\infty^2 \, (u_i \, \gamma_i \, \cos \psi_i - v_i \, \gamma_i \, \sin \psi_i) \, \Delta y_j / \cos \psi_i$$

$$= 2 \, q \, (u_i - v_i \, \tan \psi_i) \, \gamma_i \, \Delta y_j$$

where,

γ_i is the bound vortex density,

u_i and v_i are the x and y components of the induced velocities,

ψ_i is the sweep angle of the bound element,

Δy_j is the width of the jth strip,

Δs_i is the length of bound element,

γ_x and γ_y are the streamwise and spanwise components of the bound vortex density.

Thus, the lifting pressure due to the ith bound element of the jth strip is:

$$(\Delta C_{p_{j,i}})_B = \frac{F_{B_{j,i}}}{q \, \Delta y_j} = 2(u_i - v_i \, \tan \psi_i) \, \gamma_i \qquad (A.11)$$

For a cambered wing without dihedral, additional lifting pressure will be generated from the interaction of a free stream component with the streamwise vortex density γ_x (ref. 26), as shown in Fig. A3. Adding this component of $(-2 \, \gamma_x \, \sin \alpha \, \sin \phi_y)$ to the lifting pressure due to the wing bound element, equation (A.11) is modified to:

51

$$\gamma_y = \gamma_i \cos\psi_i \text{ (spanwise vortices)}$$

$$\gamma_x = \gamma_i \sin\psi_i \text{ (streamwise vortices)}$$

i^{th} wing bound element of jth strip

Δs_i

Δy_j

j^{th} strip
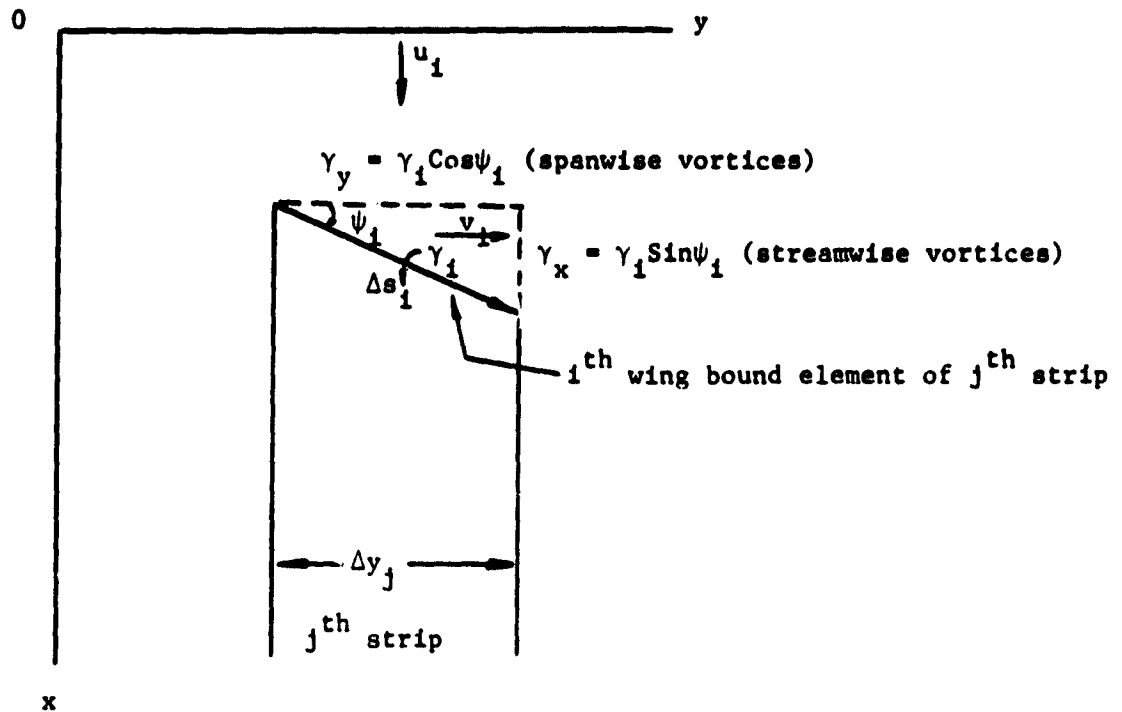
Figure A2.- Wing bound element components

V_∞

Mean chord plane

$C_P = -2\gamma_x \sin\alpha \sin\phi_y$

$\phi_y = \tan^{-1}(\partial \bar{z}_c/\partial y)$

γ_x

Section A-A

$V_\infty \sin\alpha$

$V_\infty \sin\alpha \sin\phi_y$

ϕ_y
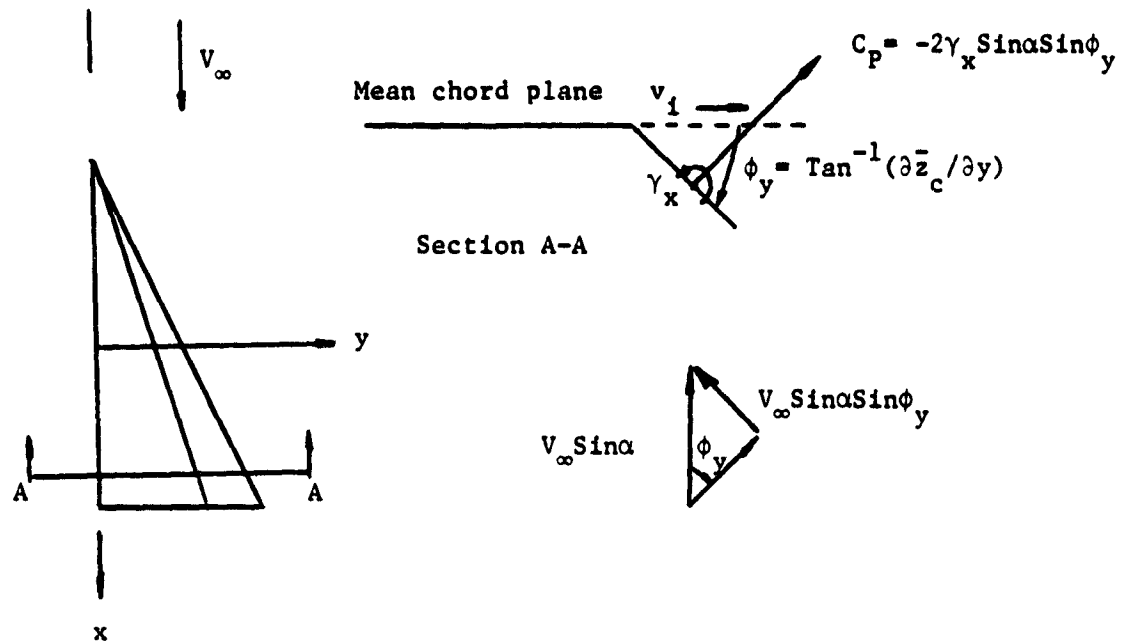
Figure A3.- Local dihedral effect on lifting pressure

$$\left(\Delta C_{P_{j,i}} \right)_B = 2 \left[(u_i - \mathbf{\hat{v}}_i \text{ Cos } \phi_y + \text{Sin } \alpha \text{ Sin } \phi_y) \text{ Tan } \psi_y \right] \gamma_i \qquad \text{(A.12)}$$

where ϕ_y may be defined as the local dihedral angle, $\text{Tan}^{-1}(\partial z_c / \partial y)$, and may be different everywhere on a cambered wing. The correction term in equation (A.12) is applied only to the wing bound element and leading-edge bound element so that the local dihedral effect are included.

At positive α, normally the wing bound elements produce positive lifting pressure near the leading edge; while the leading-edge bound elements produce negative lifting pressure. Thus, the leading-edge Kutta condition can be satisfied when the net lifting pressure is zero at the leading-edge. In order to substract the lifting pressure induced by the leading-edge bound element from that produced by the wing bounded vortex elements, the following prodecures will be used:

(1) Extrapolate lifting pressure due to the wing bound elements in each chordwise direction to obtain the lifting pressure at the location of the leading-edge bound element EF. (See Fig. 3) Using the Fourier series relation, the lifting pressure at any chordwise location is determined by the following equation:

$$\Delta C_p \text{ Sin } \theta = a_0 + \sum_{\ell=1}^{N} a_\ell \text{ Cos } \ell\theta \qquad \text{(A.13)}$$

where $\text{Sin}\theta$ is included to eliminate the known square root singularity of the lifting pressure at the leading - and trailing-edges.

Therefore,

$$a_0 = \frac{1}{\pi} \int_0^\pi \Delta C_p \text{ Sin}\theta \text{ } d\theta$$

$$\approx \frac{1}{N} \sum_{k=1}^{N} \Delta C_{p_k} \text{ Sin } \theta_k$$

$$a_\ell = \frac{2}{\pi} \int_0^\pi \Delta C_p \text{ Sin}\theta \text{ Cos}\ell\theta \text{ } d\theta \approx \frac{2}{N} \sum_{k=1}^{N} \Delta C_{p_k} \text{ Sin}\theta_k \text{ Cos}\ell\theta_k \qquad \text{(A.14)}$$

$$\theta_k = \frac{(2k-1)\pi}{2N} , \quad k=1, ---N$$

53

where N is the number of wing bound elements in the chordwise direction. The integrals for Fourier coefficients are reduced to finite sums through the mid-point trapezoidal rule.

(2) Subtract suction pressure induced by the leading-edge bound elements. First, the concentrated strength of the leading-edge vortex element is converted to the vortex density. Since,

$$\Gamma = \int \gamma \, dx \tag{A.15}$$

from the transformation,

$$x = x_\ell + \frac{c_j}{2} (1 - \cos \theta) \tag{A.16}$$

it can be obtained that

$$\Gamma_j = \frac{c_j}{2} \int \gamma \sin \theta \, d\theta \tag{A.17}$$

It is assumed that the concentrated vorticity due to the leading-edge vortex system is distributed near the leading-edge only. Using the mid-point trapezoidal rule, equation (A.17) becomes:

$$\Gamma_j = \frac{\pi c_j \sin \theta_1}{2(N + 1)} \gamma_j \tag{A.18}$$

or,

$$\gamma_j = \frac{2(N + 1) \Gamma_j}{\pi c_j \sin \theta_1} \tag{A.19}$$

where $\theta_1 = \frac{\pi}{2(N + 1)}$. Thus, the decrease of lifting pressure at the leading-edge bound element of the jth strip is:

$$(\Delta C_p)_{j_{decrease}} = -2 \left[u_j - (v_j \cos \phi_y + \sin \alpha \sin \phi_y) \tan \psi_j \right]_{\ell_e} \gamma_j \tag{A.20}$$

where the subscript ℓe means that u_j, v_j, ϕ_y and ψ_j are evaluated at the leading-edge bound vortex element of the jth strip. Hence, the actual lifting pressure at the location of the leading-edge bound element of the jth strip is:

54

$$(\Delta C_{p_{j,1}}) = \left[(\Delta C_{p_{j,1}})_B + (\Delta C_{p_{j,1}})_T\right]_{le} + (\Delta C_p)_{j_{decrease}} \tag{A.21}$$

The lifting pressures defined by equation (A.1) at a discrete number of points are Fourier-analyzed through equation (A.14) so that lifting pressures at any locations can be calculated.

Appendix B

Correction to Sidewash Calculation in Discrete Vortex Method

In developing the free vortex filament theory for calculating aerodynamic characteristics of wings with edge-separated vortex flow, the position of the concentrated vortex core is adjusted in the direction of decreasing Kutta-Joukowsky force. The magnitude of the force, and hence the new position of the vortex core, depends on the calculated induced velocity components on the core. It is well known that the induced sidewash cannot be accurately calculated by the discrete vortex approximation at points close to the vortex sheet. Therefore, the vortex core location and the wing aerodynamic characteristics will not be accurately evaluated. A method to improve the accuracy of calculating sidewash by discrete vortex approximation will be detailed in the following paragraphs.

B.1 A Test Case

Assume a vortex distribution with constant density $(\vec{\omega} = \omega \vec{1})$ exist in a rectangular region, as shown in Fig. B1. The induced velocity vector at any point in space with position vector $\vec{R}$, is then given by:

$$\vec{V}(\vec{R}) = \frac{\beta^2}{4\pi} \int_s \frac{(\vec{R}_1 - \vec{R}) \times \vec{\omega}}{R_\beta^3} \, ds$$

$$= \frac{\beta^2}{4\pi} \int_o^{b/2} \int_o^a \frac{\omega (\zeta - z)\vec{j} - (\eta - y)\vec{k}}{\left[(\xi - x)^2 + \beta^2 (\eta - y)^2 + \beta^2 (\zeta - z)^2\right]^{3/2}} \, d\xi \, d\eta \quad (B.1)$$

where

$$\beta^2 = 1 - M^2$$

$$R_\beta^2 = (\xi - x)^2 + \beta^2 (\eta - y)^2 + \beta^2 (\zeta - z)^2$$

$$\vec{R}_1 - \vec{R} = (\xi - x)\vec{1} + (\eta - y)\vec{j} + (\zeta - z)^2$$

Since the vortex density ω is assumed to be constant over the entire region, equation (B.1) can be integrated (ref. 33) to give a closed-form expression for the sidewash V as:

56
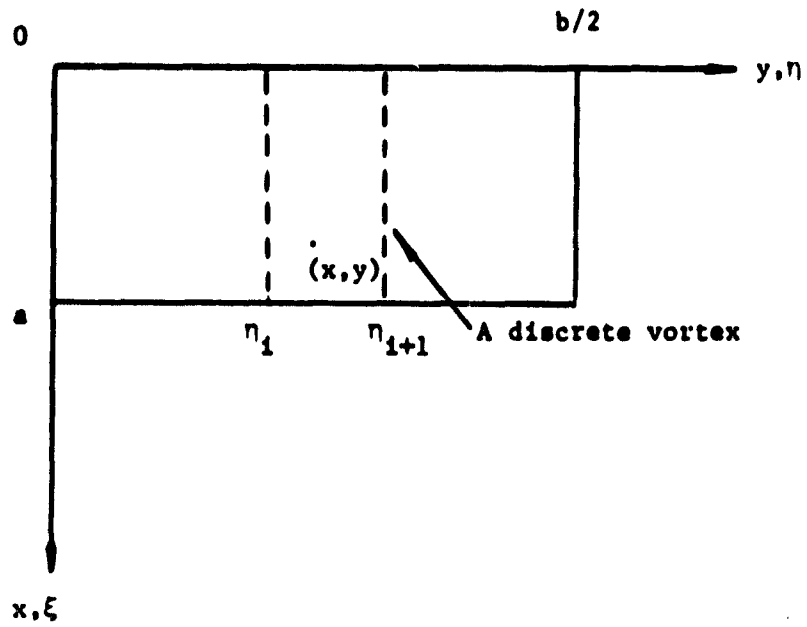
Figure B1.- Vortex distribution in a rectangular region
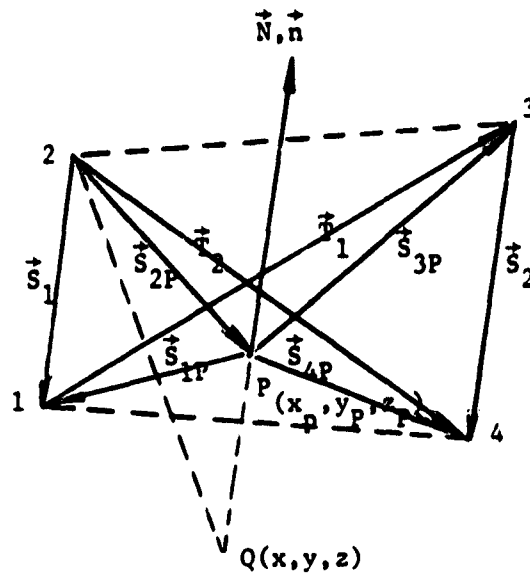
$\overline{21}$ and $\overline{34}$ are vortex segments of a strip

Figure B2.- Local panel geometry

$$v = \frac{\omega \beta^2}{4\pi} \left\{ \text{Tan}^{-1} \frac{(\frac{b}{2} - y)(a - x)}{|\zeta - z| \left[(a - x)^2 + \beta^2 (\frac{b}{2} - y)^2 + \beta^2 (\zeta - z)^2 \right]^{\frac{1}{2}}} \right.$$

$$- \text{Tan}^{-1} \frac{(-y)(a - x)}{|\zeta - z| \left[(a - x)^2 + \beta^2 y^2 + \beta^2 (\zeta - z)^2 \right]^{\frac{1}{2}}}$$

$$+ \text{Tan}^{-1} \frac{(\frac{b}{2} - y)(x)}{|\zeta - z| \left[x^2 + \beta^2 (\frac{b}{2} - y)^2 + \beta^2 (\zeta - z)^2 \right]^{\frac{1}{2}}}$$

$$\left. - \text{Tan}^{-1} \frac{(-x)(y)}{|\zeta - z| \left[x^2 + \beta^2 y^2 + \beta^2 (\zeta - z)^2 \right]^{\frac{1}{2}}} \right\} \qquad (B.2)$$

Equation (B.2) will be used to check the accuracy of approximate methods of calculating the integrals in equation (B.1).

B.2 Approximate Methods

The chordwise integration in equation (B.1) is performed exactly so that the sidewash component becomes:

$$v = \frac{(\zeta - z) \beta^2}{4\pi} \int_0^{b/2} \frac{\omega(\eta) \, d\eta}{(\eta - y)^2 + (\zeta - z)^2} \left\{ \frac{a - x}{\left[(a - x)^2 + \beta^2 (\eta - y)^2 \right.}\right.$$

$$\left. \left. + \beta^2 (\zeta - z)^2 \right]^{\frac{1}{2}} + \frac{x}{\left[x^2 + \beta^2 (\eta - y)^2 + \beta^2 (\zeta - z)^2 \right]^{\frac{1}{2}}} \right\} \qquad (B.3)$$

In conventional discretized approximation, equation (B.3) is reduced to:

$$v = \frac{(\zeta - z) \beta^2}{4\pi} \sum_{k=1}^{N} \frac{\omega_k \, \Delta\eta_k}{(\eta_k - y)^2 + (\zeta - z)^2} \left\{ \frac{a - x}{\left[(a - x)^2 + \beta^2 (\eta_k - y)^2 \right.}\right.$$

$$\left. \left. + \beta^2 (\zeta - z)^2 \right]^{\frac{1}{2}} + \frac{x}{\left[x^2 + \beta^2 (\eta_k - y)^2 + \beta^2 (\zeta - z)^2 \right]^{\frac{1}{2}}} \right\} \qquad (B.4)$$

The results in equation (B.4) are equivalent to applying mid-point trapezoidal rule to evaluating the spanwise integral in equation (B.3). However, when $(\zeta - z)$ is small, the integrand in equation (B.3) contains a second-order singularity at $\eta = y$, so that equation (B.4) is expected to be inaccurate. To improve equation (B.4) and yet keep the method as simple as possible, the following consideration is applied.

58

For convenience, let

$$f(\eta) = \frac{a - x}{\left[(a - x)^2 + \beta^2 (\eta - y)^2 + \beta^2 (\zeta - z)^2\right]^{\frac{1}{2}}}$$

$$+ \frac{x}{\left[x^2 + \beta^2 (\eta - y)^2 + \beta^2 (\zeta - z)^2\right]^{\frac{1}{2}}} \tag{B.5}$$

If $\eta_i < y < \eta_{i+1}$, equation (B.3) can be rewritten as:

$$v = \frac{(\zeta - z)\beta^2}{4\pi}\left[\left(\int_0^{\eta_i} + \int_{\eta_i}^{\eta_{i+1}} + \int_{\eta_{i+1}}^{b/2}\right) \frac{\omega(\eta)\, f(\eta)}{(\eta - y)^2 + (\zeta - z)^2}\, d\eta\right] \tag{B.6}$$

The first and the last integrals can be reduced to finite sums as usual:

$$v \approx \frac{(\zeta - z)\beta^2}{4\pi}\left[\sum_{k=1}^{i-1} \frac{\omega_k\, f(\eta_k)\, \Delta\eta_k}{(\eta_k - y)^2 + (\zeta - z)^2} + \frac{1}{2}\frac{\omega_i\, f(\eta_i)\, \Delta\eta_i}{(\eta_i - y)^2 + (\zeta - z)^2}\right.$$

$$\left. + \frac{1}{2}\frac{\omega_{i+1}\, f(\eta_{i+1})\, \Delta\eta_{i+1}}{(\eta_{i+1} - y)^2 + (\zeta - z)^2} + \sum_{k=i+1}^{N} \frac{\omega_k\, f(\eta_k)\, \Delta\eta_k}{(\eta_k - y)^2 + (\zeta - z)^2} + E\right] \tag{B.7}$$

where

$$E = \int_{\eta_i}^{\eta_{i+1}} \frac{\omega(\eta)\, f(\eta)}{(\eta - y)^2 + (\zeta - z)^2}\, d\eta$$

$$= \int_{\eta_i}^{\eta_{i+1}} \frac{\omega(\eta)\, f(\eta) - \omega(y)\, f(y)}{(\eta - y)^2 + (\zeta - z)^2}\, d\eta + \omega(y)\, f(y) \int_{\eta_i}^{\eta_{i+1}} \frac{d\eta}{(\eta - y)^2 + (\zeta - z)^2}$$

$$\approx \frac{1}{2}\frac{\omega(\eta_i)\, f(\eta_i) - \omega(y)\, f(y)}{(\eta_i - y)^2 + (\zeta - z)^2}\Delta\eta_i + \frac{1}{2}\frac{\omega(\eta_{i+1})\, f(\eta_{i+1}) - \omega(y)\, f(y)}{(\eta_{i+1} - y)^2 + (\zeta - z)^2}\Delta\eta_{i+1}$$

$$+ \frac{\omega(y)\, f(y)}{|\zeta - z|}\left[\text{Tan}^{-1}\frac{\eta_{i+1} - y}{|\zeta - z|} - \text{Tan}^{-1}\frac{\eta_i - y}{|\zeta - z|}\right] \tag{B.8}$$

In equation (B.8), the first integral was evaluated by conventional trapezoidal rule which is probably not accurate in this case. However, this is necessary to keep the method simple so that it is easily extendable to more general applications. A correction factor may be applied, as will be indicated later (see equation (B.10)).

59

Substituting equation (B.8) into equation (2.7) results in:

$$v \cong \frac{(\zeta - z)\beta^2}{4\pi}\left[\sum_{k=1}^{N} \frac{\omega_k\, f\,(\eta_k)\, \Delta\eta_k}{(\eta_k - y)^2 + (\zeta - z)^2} - \tfrac{1}{2}\frac{\omega(y)\, f\,(y)\, \Delta\eta_1}{(\eta_1 - y)^2 + (\zeta - z)^2}\right.$$

$$\left. - \tfrac{1}{2}\frac{\omega\,(y)\, f\,(y)\, \Delta\eta_{1+1}}{(\eta_{1+1} - y)^2 + (\zeta - z)^2}\right] + \frac{\omega\,(y)\, f\,(y)\,\beta^2}{|\zeta - z|} \cdot$$

$$\left[\mathrm{Tan}^{-1}\frac{\eta_{1+1} - y}{|\zeta - z|} - \mathrm{Tan}^{-1}\frac{\eta_1 - y}{|\zeta - z|}\right] \qquad (B.9)$$

The first term in equation (B.9) represents exactly what would be given by the conventional discretized approximation (see equation (B.4)). Therefore, the remaining terms represent a correction C:

$$C = -\frac{G}{2}\left(\frac{(\zeta - z)\beta^2}{4\pi}\right)\left\{\frac{\omega(y)\, f(y)\, \Delta\eta_1}{(\eta_1 - y)^2 + (\zeta - z)^2} + \frac{\omega(y)\, f(y)\, \Delta\eta_{1+1}}{(\eta_{1+1} - y)^2 + (\zeta - z)^2}\right\}$$

$$+ \frac{(\zeta - z)}{|\zeta - z|}\left(\frac{\omega(y)\, f(y)\,\beta^2}{4\pi}\right)\left\{\mathrm{Tan}^{-1}\frac{\eta_{1+1} - y}{|\zeta - z|} - \mathrm{Tan}^{-1}\frac{\eta_1 - y}{|\zeta - z|}\right\} \qquad (B.10)$$

where G is a correction factor mentioned above and is taken to be 1.1 in the following numerical study.

B.3 General Applications

To apply equation (B.10) to general situations involving such as leading-edge vortex sheet, trailing-vortex mutual interaction, etc., all geometric quantities involved in equation (B.10) should be evaluated based on local panel coordinate system. To illustrate this, consider two vortex segments $\overline{21}$ and $\overline{34}$ in Fig. B2 and "P" is a point on a plane normal to two diagonal vectors ($\vec{T}_1$ and $\vec{T}_2$) and is obtained by projecting the control point Q along the normal vector. The vectors $\vec{T}_1$ and $\vec{T}_2$ can be calculated as:

$$\vec{T}_1 = (x_3 - x_1)\,\vec{i} + (y_3 - y_1)\,\vec{j} + (z_3 - z_1)\,\vec{k} \qquad (B.11)$$

$$\vec{T}_2 = (x_4 - x_2)\,\vec{i} + (y_4 - y_2)\,\vec{j} + (z_4 - z_2)\,\vec{k} \qquad (B.12)$$

60

It follows that a normal vector $\vec{N}$ may be defined as:

$$\vec{N} = \vec{T}_1 \times \vec{T}_2 = \begin{vmatrix} \vec{I} & \vec{J} & \vec{k} \\ x_3 - x_1 & y_3 - y_1 & z_3 - z_1 \\ x_4 - x_2 & y_4 - y_2 & z_4 - z_2 \end{vmatrix}$$

$$= \vec{I} \left[(y_3 - y_1)(z_4 - z_2) - (z_3 - z_1)(y_4 - y_2) \right]$$

$$+ \vec{J} \left[(z_3 - z_1)(x_4 - x_2) - (x_3 - x_1)(z_4 - z_2) \right]$$

$$+ \vec{k} \left[(x_3 - x_1)(y_4 - y_2) - (y_3 - y_1)(x_4 - x_2) \right]$$

$$= N_x \vec{I} + N_y \vec{J} + N_z \vec{k} \tag{B.13}$$

A unit vector associated with $\vec{N}$ can be defined as:

$$\vec{n} = \frac{\vec{N}}{|\vec{N}|} \tag{B.14}$$

To determine the coordinate of "P", the distance $\overline{PQ}$ is needed. However, $\overline{PQ}$ is just the projection of vector $\overline{2Q}$ onto the normal vector $\vec{n}$:

$$\overline{PQ} = \overline{2Q} \cdot \vec{n}$$

$$= (x - x_2) n_x + (y - y_2) n_y + (z - z_2) n_z \tag{B.15}$$

It follows that the coordinates of point P are:

$$x_p = (x - x_2)n_x$$

$$y_p = (y - y_2)n_y$$

$$z_p = (z - z_2)n_z \tag{B.16}$$

To find the distances "x" and "a - x" in equation (B.10) (through f(y)), the unit vectors $\vec{u}_{21}$ and $\vec{u}_{34}$ are needed:

$$\vec{u}_{21} = \frac{(x_1 - x_2) \vec{I} + (y_1 - y_2) \vec{J} + (z_1 - z_2) \vec{k}}{\left[(x_1 - x_2)^2 + (y_1 - y_2)^2 + (z_1 - z_2)^2 \right]^{\frac{1}{2}}} \tag{B.17}$$

$$\vec{u}_{34} = \frac{(x_4 - x_3) \vec{I} + (y_4 - y_3) \vec{J} + (z_4 - z_3) \vec{k}}{\left[(x_4 - x_3)^2 + (y_4 - y_3)^2 + (z_4 - z_3)^2 \right]^{\frac{1}{2}}} \tag{B.18}$$

Then, the "x" distance in equation (B.10) can be replaced by:

$$x_R = \tfrac{1}{2} (\vec{S}_{2p} \cdot \vec{u}_{21} + \vec{S}_{3p} \cdot \vec{u}_{34}) \tag{B.19}$$

61

where

$$\vec{S}_{2p} = (x_p - x_2)\,\vec{I} + (y_p - y_2)\,\vec{J} + (z_p - z_2)\,\vec{k} \tag{B.20}$$

$$\vec{S}_{3p} = (x_p - x_3)\,\vec{I} + (y_p - y_3)\,\vec{J} + (z_p - z_3)\,\vec{k} \tag{B.21}$$

On the other hand, the "a - x" distance in equation (B.10) can be replaced by:

$$x_R' = \tfrac{1}{2}\,(\vec{S}_{1p}\cdot \vec{u}_{21} + \vec{S}_{4p}\cdot \vec{u}_{34}) \tag{B.22}$$

where

$$\vec{S}_{1p} = (x_1 - x_p)\,\vec{I} + (y_1 - y_p)\,\vec{J} + (z_1 - z_p)\,\vec{k} \tag{B.23}$$

$$\vec{S}_{4p} = (x_4 - x_p)\,\vec{I} + (y_4 - y_p)\,\vec{J} + (z_4 - z_p)\,\vec{k} \tag{B.24}$$

To determine "$y - \eta_i$" and "$\eta_{i+1} - y$" in equation (B.10), cross products of $\vec{S}_{2p}$ with $\vec{u}_{21}$ and $\vec{S}_{3p}$ with $\vec{u}_{34}$ are needed. Hence, "$y - \eta_i$" will be replaced by:

$$y_R = |\vec{S}_{2p} \times \vec{u}_{21}| \tag{B.25}$$

Similarly, "$\eta_{i+1} - y$" will be replaced by:

$$y_R' = |\vec{S}_{3p} \times \vec{u}_{34}| \tag{B.26}$$

Finally, "$\zeta - z$" in equation (B.10) must be determined. It is simply replaced by $-\overline{PQ}$ in equation (B.16):

$$\zeta - y = -\left[(x_p - x)^2 + (y_p - y)^2 + (z_p - z)^2\right]^{\frac{1}{2}} \tag{B.27}$$

B.4 Numerical Results

The locations of control points chosen for illustration are indicated in Fig. B3. The results are compared in Figs. B4 through B7 for M=0. Except for the case where the control point is directly under one of the discrete vortices (i.e. point B), all results with the derived correction terms "C" in equation (B.10) appear to be good. In applications to free vortex-filament program, the control points on the concentrated vortex core are chosen to be nearly at the middle of vortex strips formed by the leading-edge free vortex filaments.

62
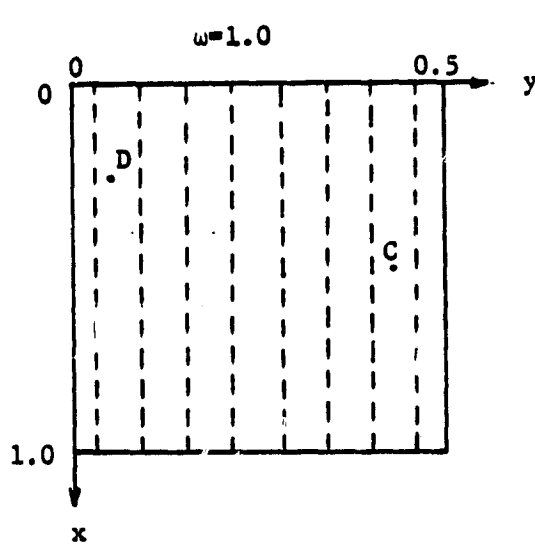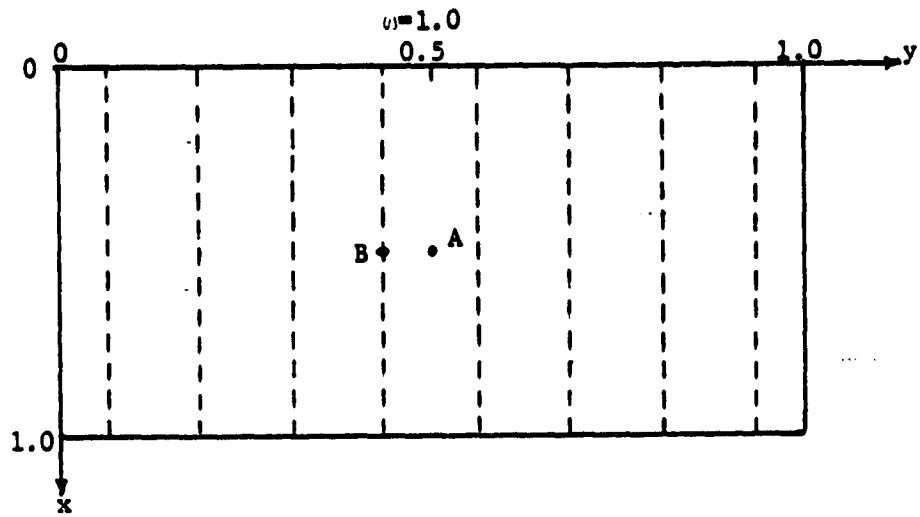
A:(0.5,0.5)
B:(0.5,0.4375)
C:(0.5,0.43)
D:(0.25,0.05)

Figure B3.- Control Point Locations for Figures B4-B7
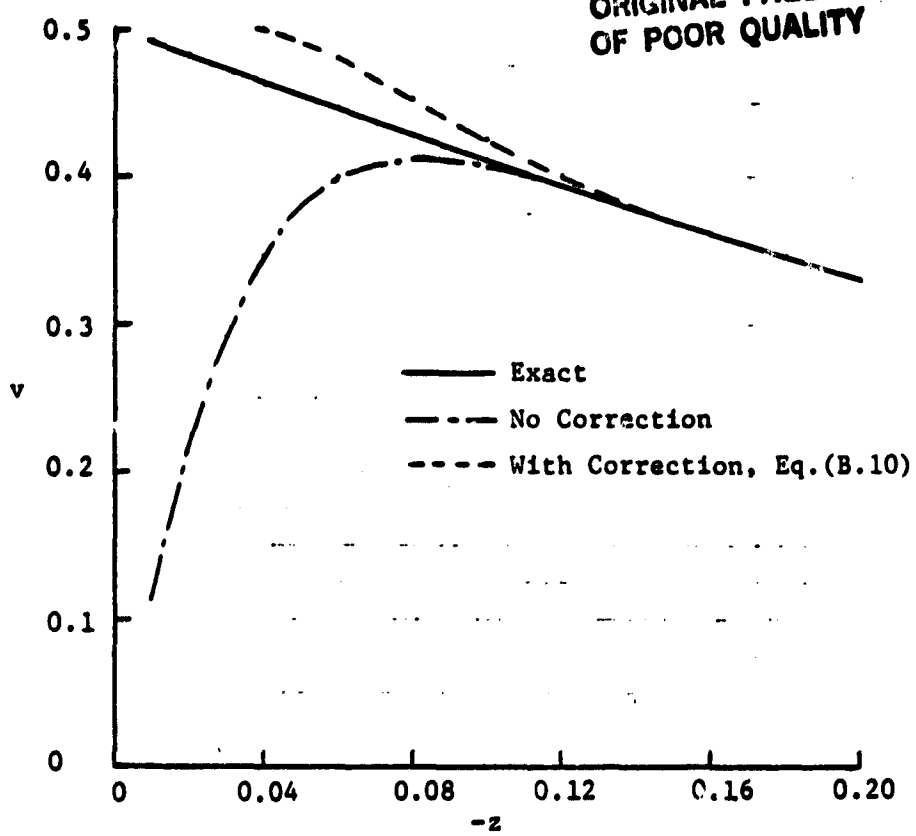
Figure B4.- Comparison of calculated induced
sidewash at point A. N = 8
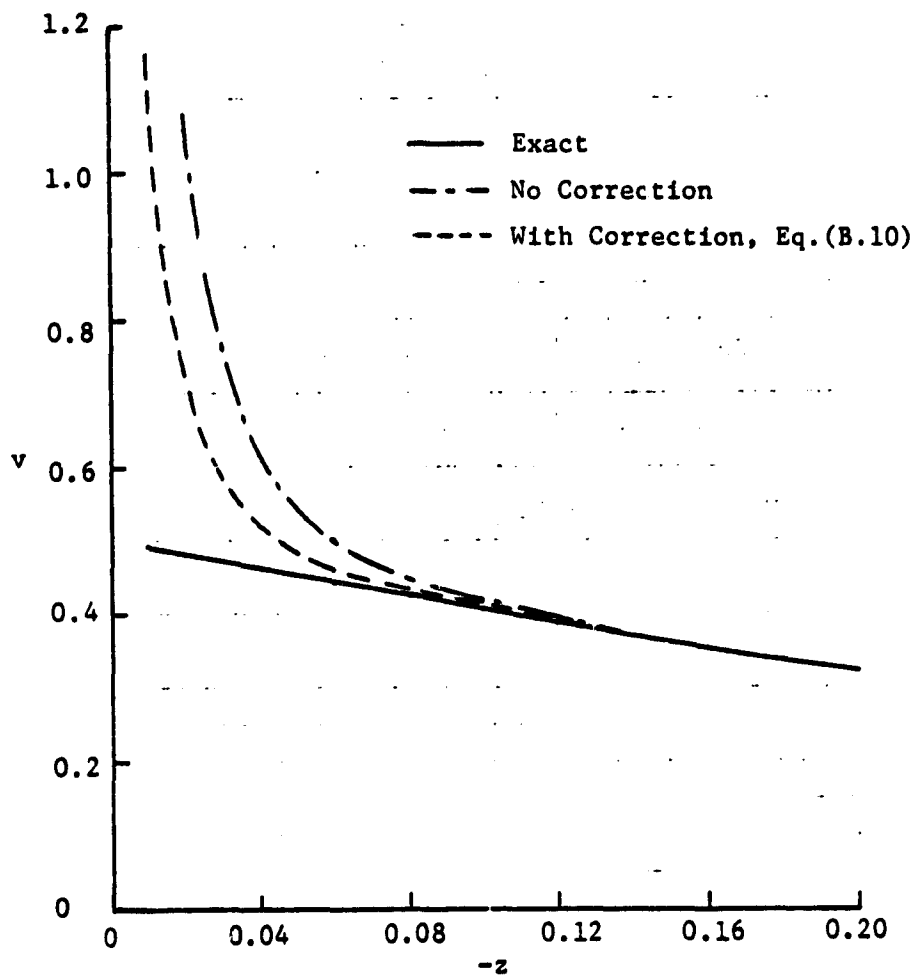
Figure B5.- Comparison of calculated induced
sidewash at point B. N = 8

64
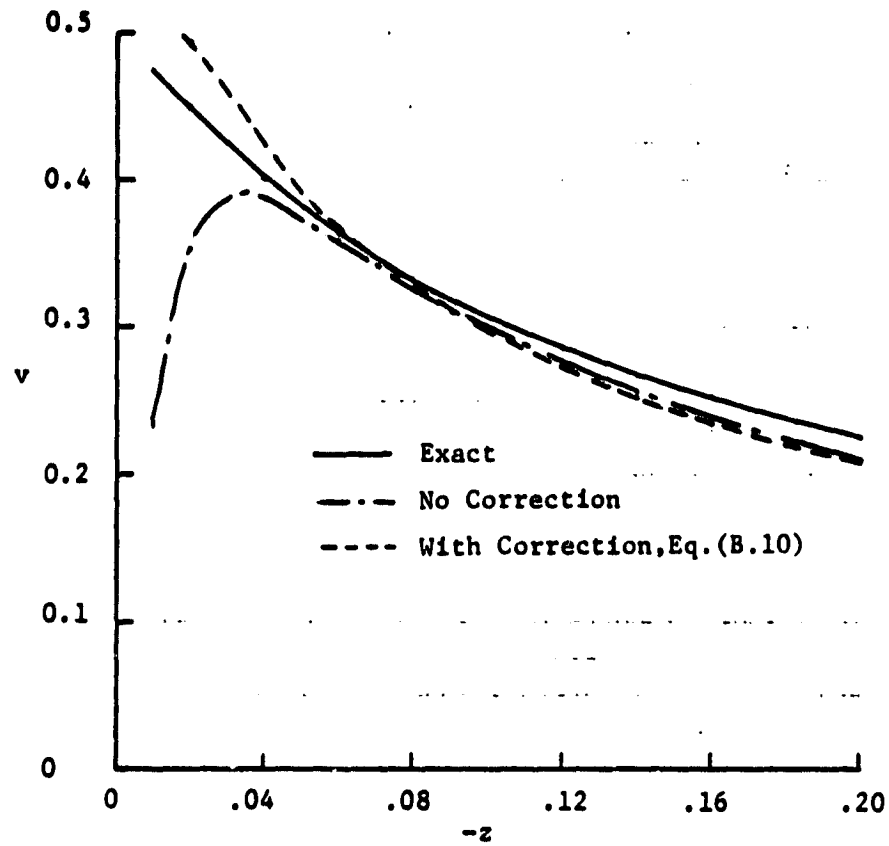
Figure B6.- Comparison of calculated induced
sidewash at point C. N = 8
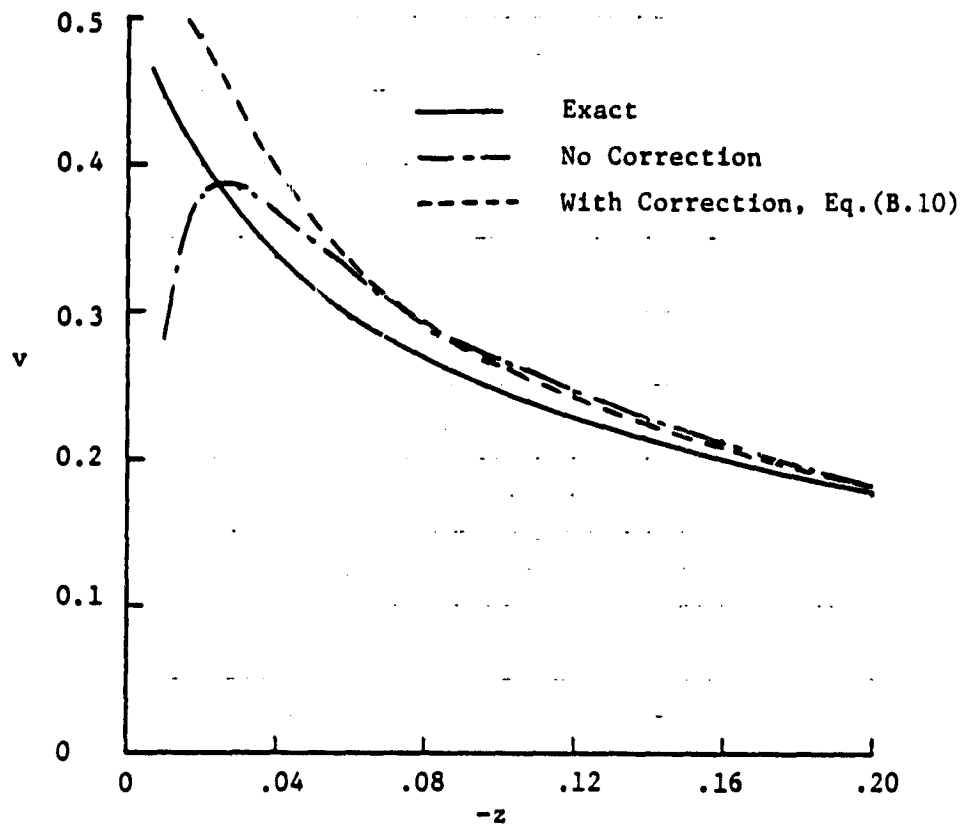
Figure B7.- Comparison of calculated induced
sidewash at point D. N = 8

Appendix C

Determining Initial Core Location by Vector Analysis

After exercising Mehrotra's code (ref. 18) through two iterations and establishing the entire leading-edge vortex element system, the centroid of the leading-edge vortex filament system is determined from equations (81) and (82). Therefore, the initial configuration of leading-edge vortex filament system and its centroid are as shown in Fig. C1.

Based on the vector analysis of the cross product, the procedures of finding the intersection between the leading-edge vortex filament system and its line of centroid are discussed in the following.

Note that each leading-edge vortex filament consists of a series of short straight segments. It is desired to find the intersection point between the leading-edge vortex element system and its line of centroid on the X-Y plane. Thus, only x and y coordinates of each segment will be considered in the cross product analysis. Assume that $\vec{S}_{12}$ is a segment along the leading-edge vortex filament system and $\vec{S}_{34}$ is a segment along the line of centroid. Then, $\vec{S}_{12}$ and $\vec{S}_{34}$ have an intersection if the following conditions are satisfied:

(1) Resulting vectors of $\vec{S}_{31} \times \vec{S}_{34}$ and $\vec{S}_{32} \times \vec{S}_{34}$ are in the opposite direction.

(2) Resulting vectors of $\vec{S}_{13} \times \vec{S}_{12}$ and $\vec{S}_{14} \times \vec{S}_{12}$ are in the opposite direction.

For example, in Fig. C2, by using the right hand rule and cross product analysis, $\vec{S}_{12}$ and $\vec{S}_{34}$ have an intersection point. Similarly, $\vec{S}_{12}$ and $\vec{S}_{34}$ have no intersections in Fig. C3.

66
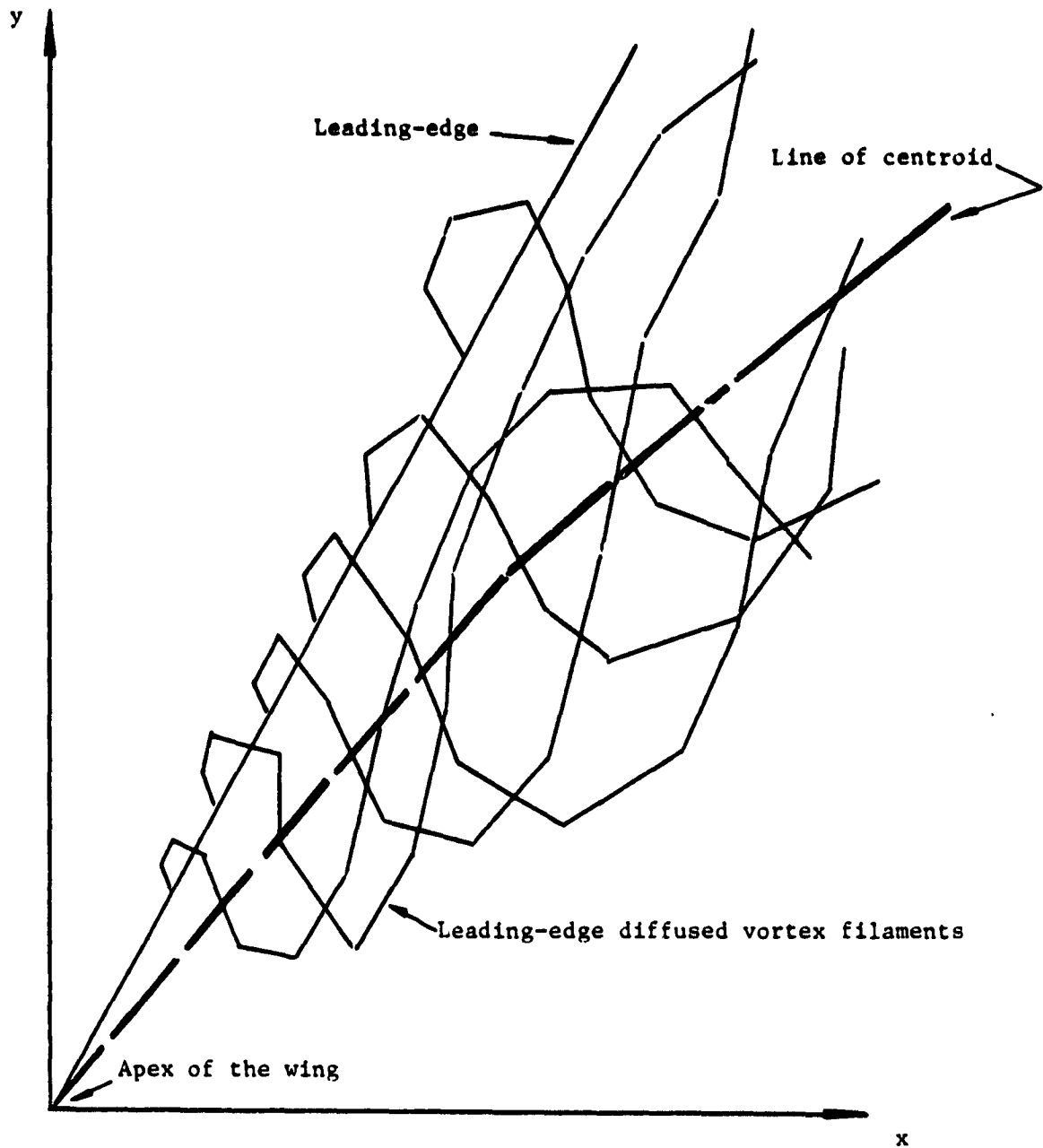
Figure C1.- Leading-edge vortex filament system and its line of centroid
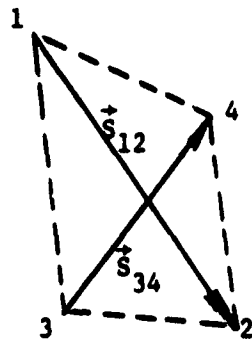
Figure C2.- $\vec{S}_{12}$ and $\vec{S}_{34}$ has intersection
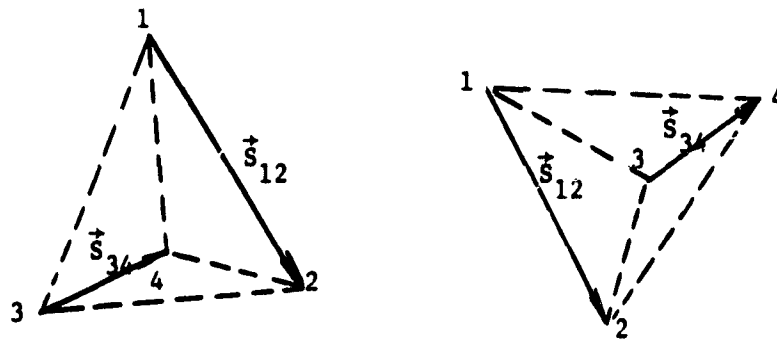
Figure C3.- $\vec{S}_{12}$ and $\vec{S}_{34}$ has no intersection

Appendix D

Corrections to Induced Velocities Due to Vortex Core

It is clear from Appendix A that the lifting pressure at the wing bound
element will not be predicted accurately, if the computation of sidewash due
to the vortex core is not treated properly. In fact, a very large sidewash
would result whenever the vortex core is too close to the wing surface. To
improve the sidewash computation due to the vortex core, and hence, the
lifting pressure and the aerodynamic characteristics, the computed sidewash
due to the vortex core will be corrected as follows.

In reference 34 (on page 592), Sir Horace Lamb showed that the circum-
ferential velocity around a circle with radius r due to a line vortex of
strength Γ is:

$$v_\theta = \frac{\Gamma}{2\pi r} (1 - e^{-r^2/4\nu t}) \tag{D.1}$$

Later, Kutler in reference 35 defined the approximate radius as:

$$r_c = 4\nu t_o \tag{D.2}$$

Thus, the tangential velocity in equation (D.1) becomes:

$$v_\theta = \frac{\Gamma}{2\pi r} (1 - e^{-r^2/r_c^2}) \tag{D.3}$$

In equation (D.1) through (D.3), r is the radial distance from the center of
the concentrated line vortex, Γ the circulation strength, r_c the approximate
core radius, ν the kinematic viscosity, and t_o the initial time.

From equation (D.3), after expanding the exponential term, the tangential
velocity becomes:

$$v_\theta = \frac{\Gamma}{2\pi r} (1 - e^{-r^2/r_c^2}) \cong \frac{\Gamma}{2\pi r} (\frac{r}{r_c})^2 \tag{D.4}$$

The above equation is obtained from the assumption that the ratio r/r_c is less than one. In the present analysis, the term of $\frac{\Gamma}{2\pi r}$ is to be regarded as the computed sidewash without correction, and all terms in equation (D.4) are defined as follows.

In Fig. D1, the vortex core segment $\vec{S}_{34}$ is on the right wing and $\vec{S}_{78}$ on the left wing. $\vec{S}_{12}$ is a leading-edge vector. Point 5 is the wing bound element location where the induced velocities due to vortex core segments $\vec{S}_{34}$ and $\vec{S}_{78}$ are to be calculated. For the right core segment $\vec{S}_{34}$, the characteristic core radius r_c is defined as 3/4 of the perpendicular distance from point 4 to line $\vec{S}_{12}$:

$$r_c = \frac{3}{4} \left| \vec{S}_{14} \times \frac{\vec{S}_{12}}{|\vec{S}_{12}|} \right| \tag{D.5}$$

The numerical factor, 3/4, in equation (D.5) is an assumed empirical value. The radial distance r of the wing bound element at point 5 to the vortex core segment $\vec{S}_{34}$ is calculated as:

$$r = \left| \vec{S}_{54} \times \frac{\vec{S}_{34}}{|\vec{S}_{34}|} \right| \tag{D.6}$$

Thus, the radial distance r is the perpendicular distance from point 5 to $\vec{S}_{34}$.

Based on the assumption in equation (D.4), the computed induced side-wash v' is to be modified only when the ratio r/r_c is less than one. The corrected induced sidewash is:

$$v = v' \left(\frac{r}{r_c} \right)^2 \quad , \quad r/r_c \leq 1.0 \tag{D.7}$$

that is the location at which the induced velocity is to be computed is inside the vortex core region.

Similarly, at the right wing bound element at point 5, the sidewash due to the left core segment $\vec{S}_{78}$ is calculated, based on the following r_c and r:

70

" r " in Eq.(D.9)

" r " in Eq.(D.6)

" r_c " in Eq.(D.8)

" r_c " in Eq.(D.5)

y

Left wing vortex core

Right wing vortex core

x
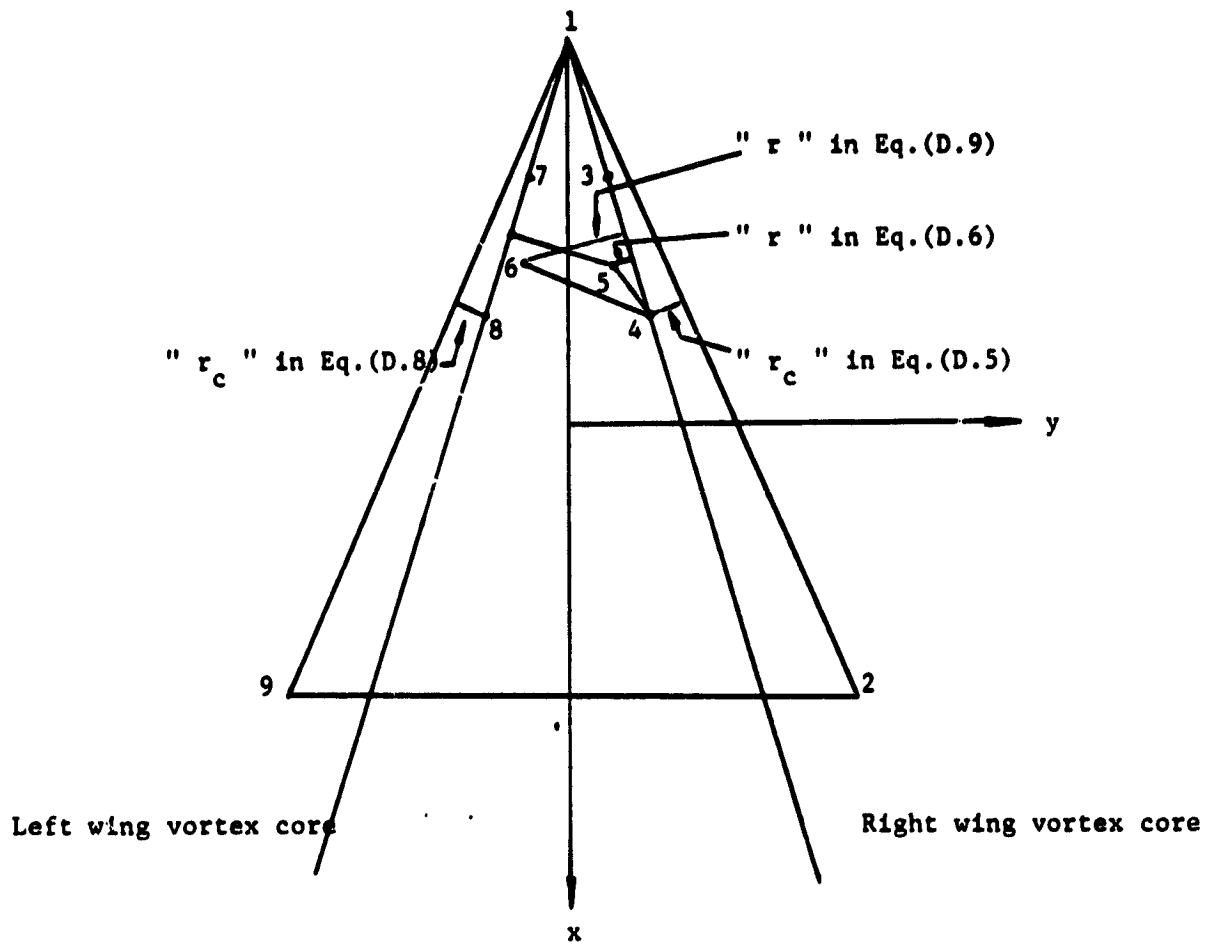
Figure D1.- Geometry of " r " and " r_c "

71

$$r_c = \frac{3}{4} \left| \vec{S}_{18} \times \frac{\vec{S}_{19}}{|\vec{S}_{19}|} \right| = \frac{3}{4} \left| \vec{S}_{14} \times \frac{\vec{S}_{12}}{|\vec{S}_{12}|} \right| \qquad (D.8)$$

$$r = \left| \vec{S}_{58} \times \frac{\vec{S}_{78}}{|\vec{S}_{78}|} \right| = \left| \vec{S}_{64} \times \frac{\vec{S}_{34}}{|\vec{S}_{34}|} \right| \qquad (D.9)$$

Again, the correction of the computed sidewash will be applied only to those points inside the vortex core region, and the modified sidewash has the same expression as that of equation (D.7). Note that the right wing vortex core segment $\vec{S}_{34}$ and the left wing vortex core segment $\vec{S}_{78}$ are geometrically similar. Therefore, in the actual computation, r_c and r due to $\vec{S}_{78}$ are based on the right wing vortex core segment $\vec{S}_{34}$ with the bound element location switched from point 5 on the right wing to its image point 6 on the left wing.
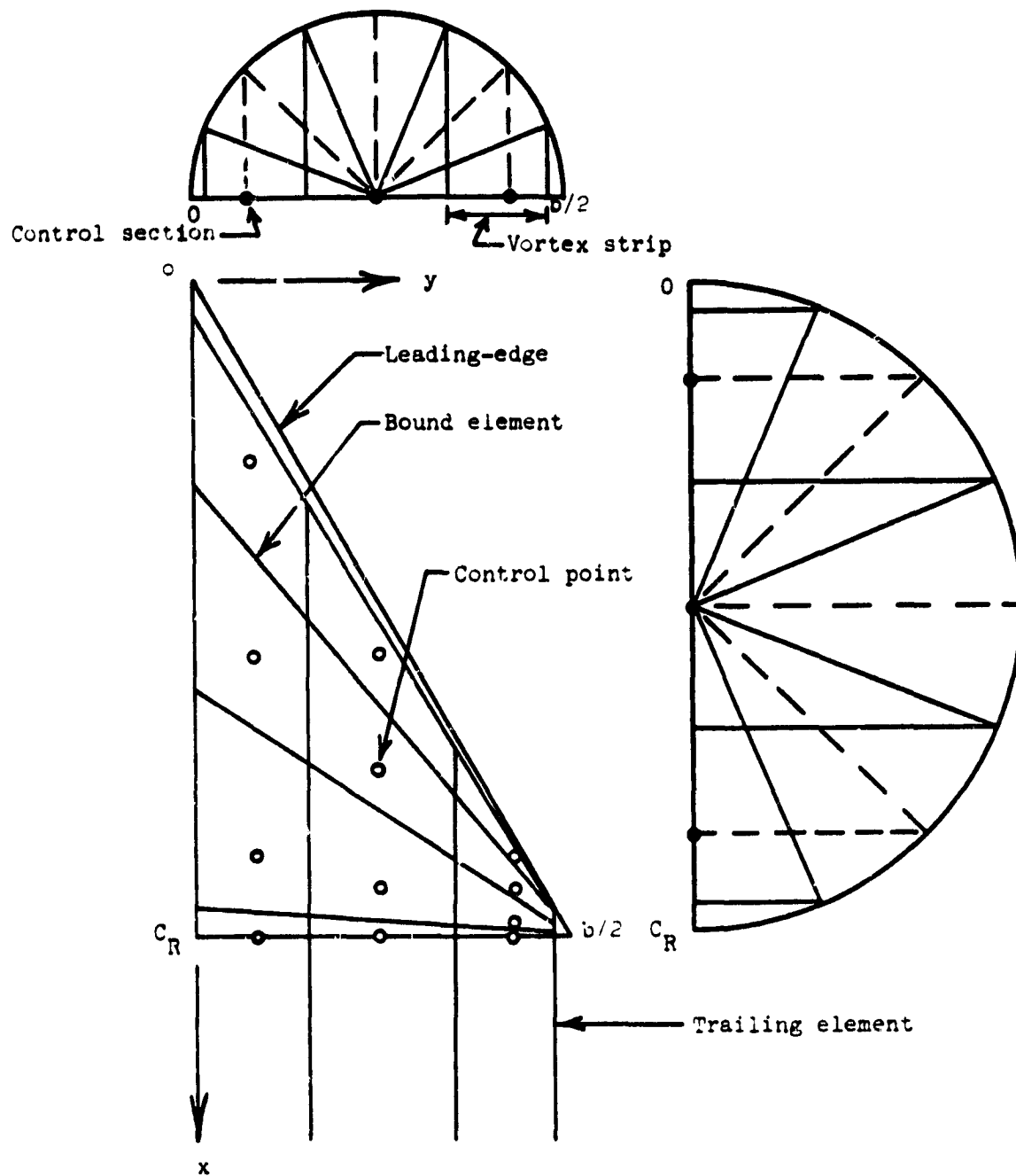
Figure 1.- Simple delta wing geometry without leading-edge vortex system

73
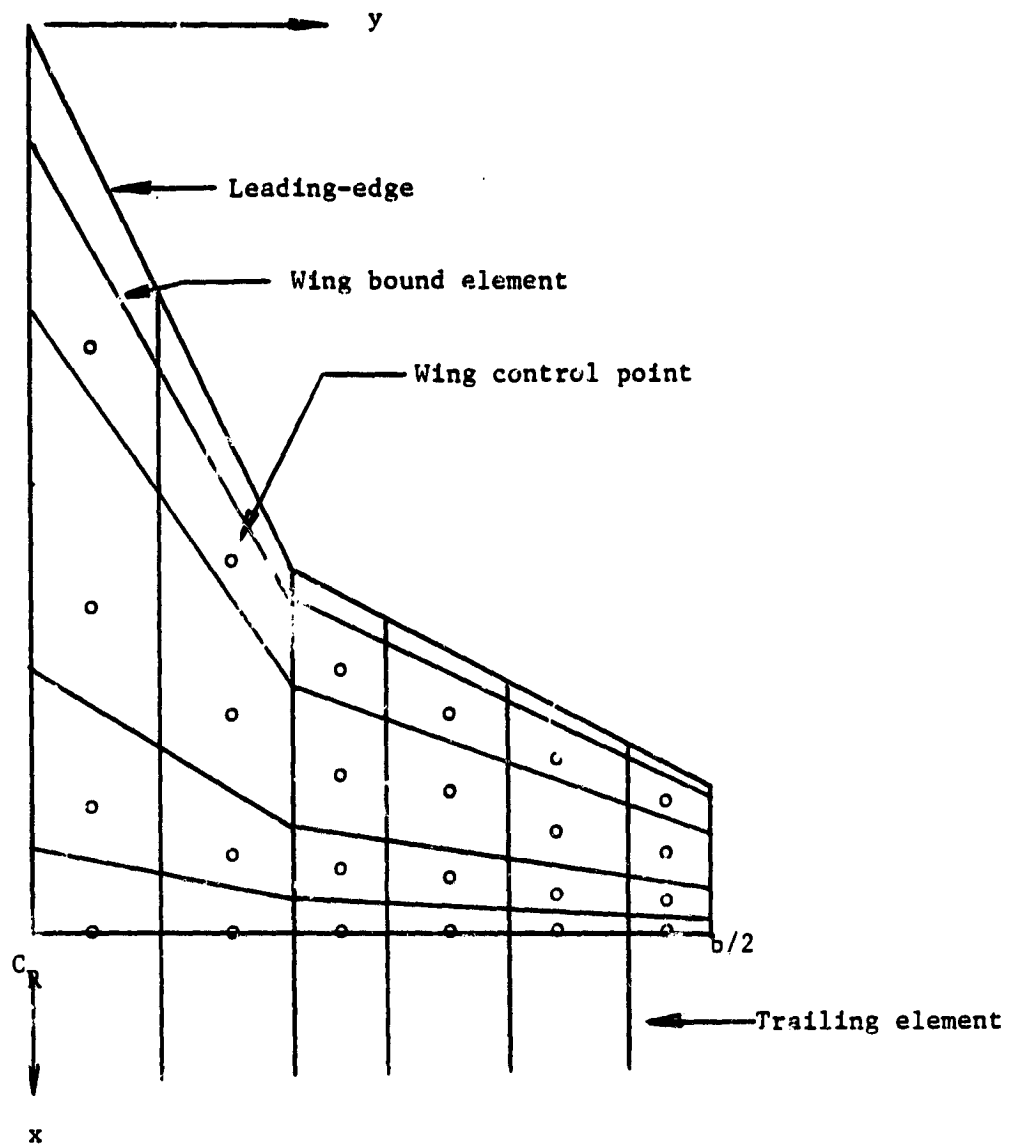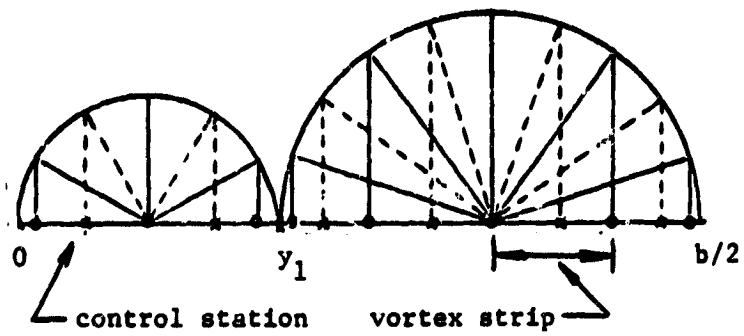
Figure 2.- Strake wing geometry without leading-edge and side-edge
vortex system

74
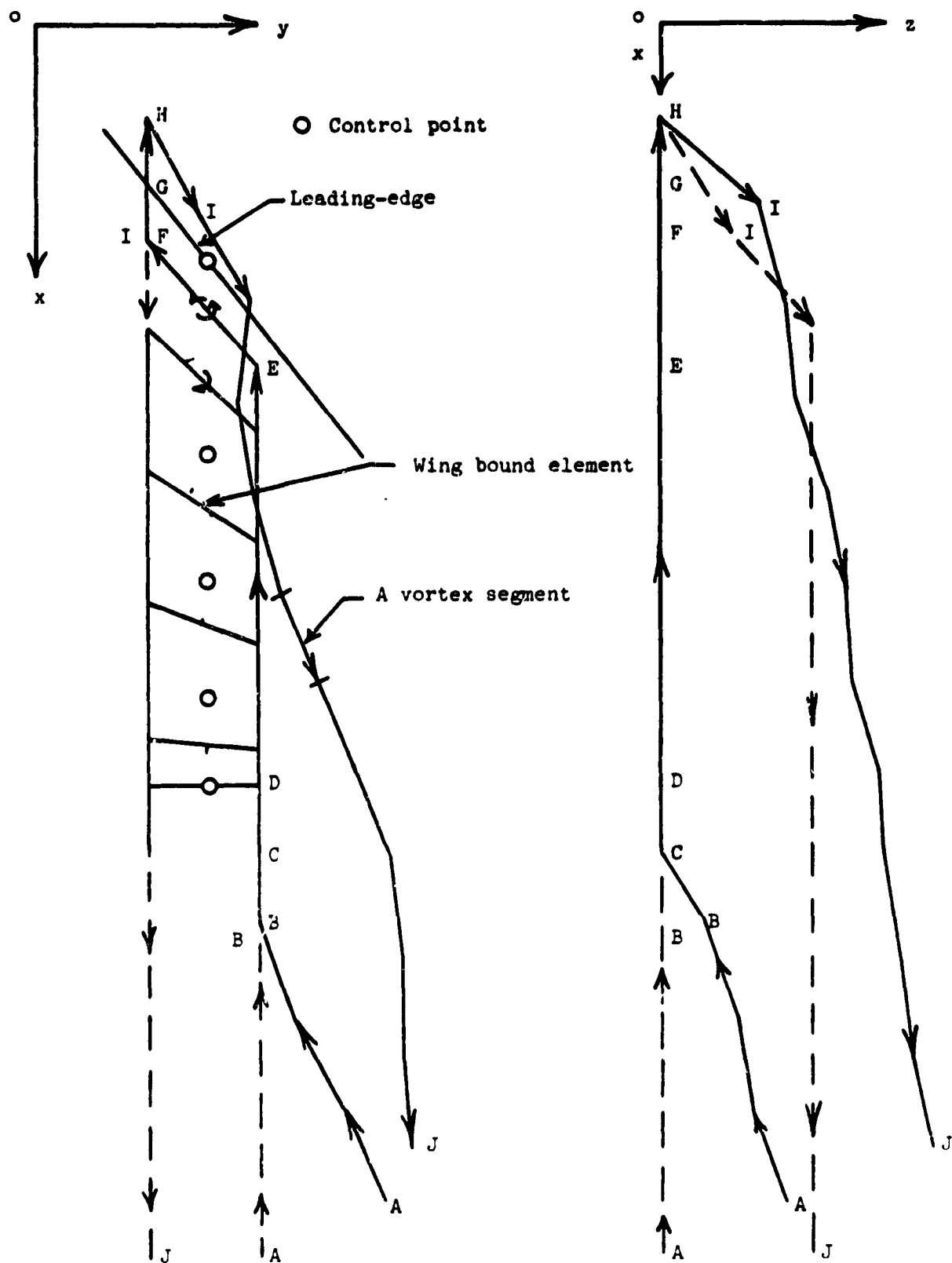
Figure 3.- A typical vortex element of leading-edge vortex system

75
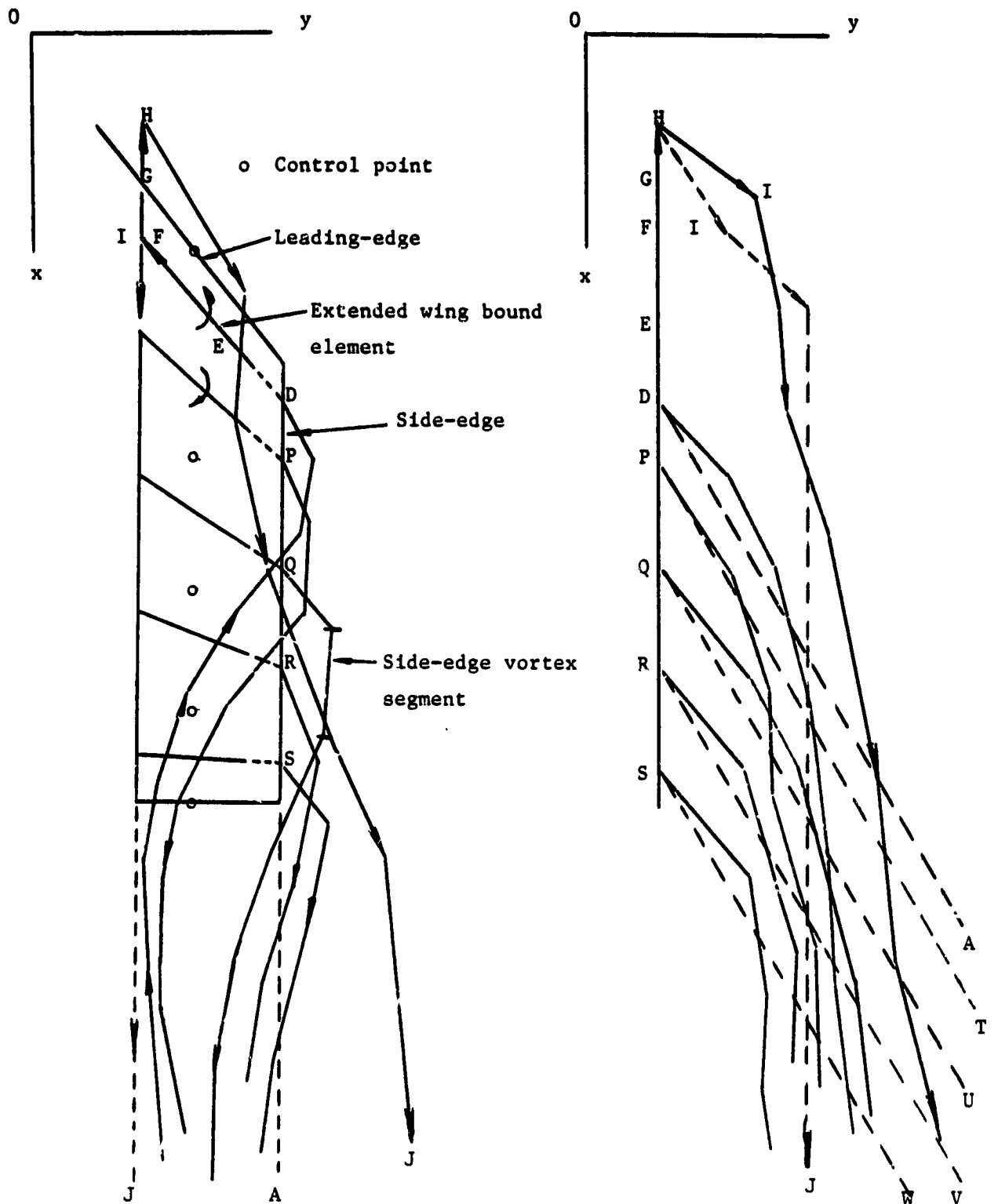
Figure 4.- Side-edge vortex system
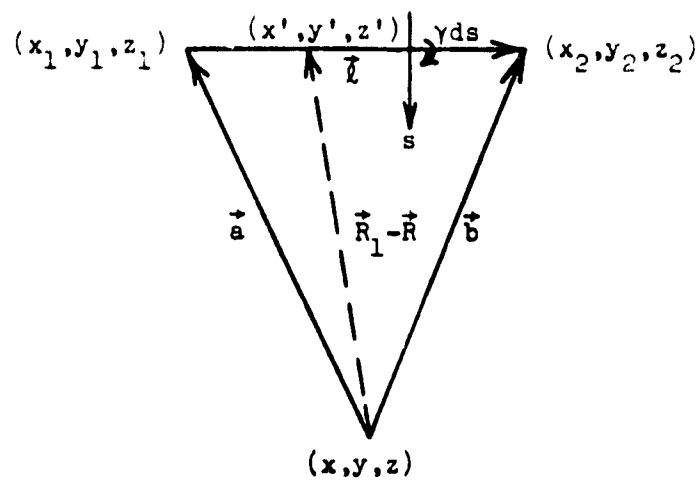
Figure 5.- Vortex segment geometry
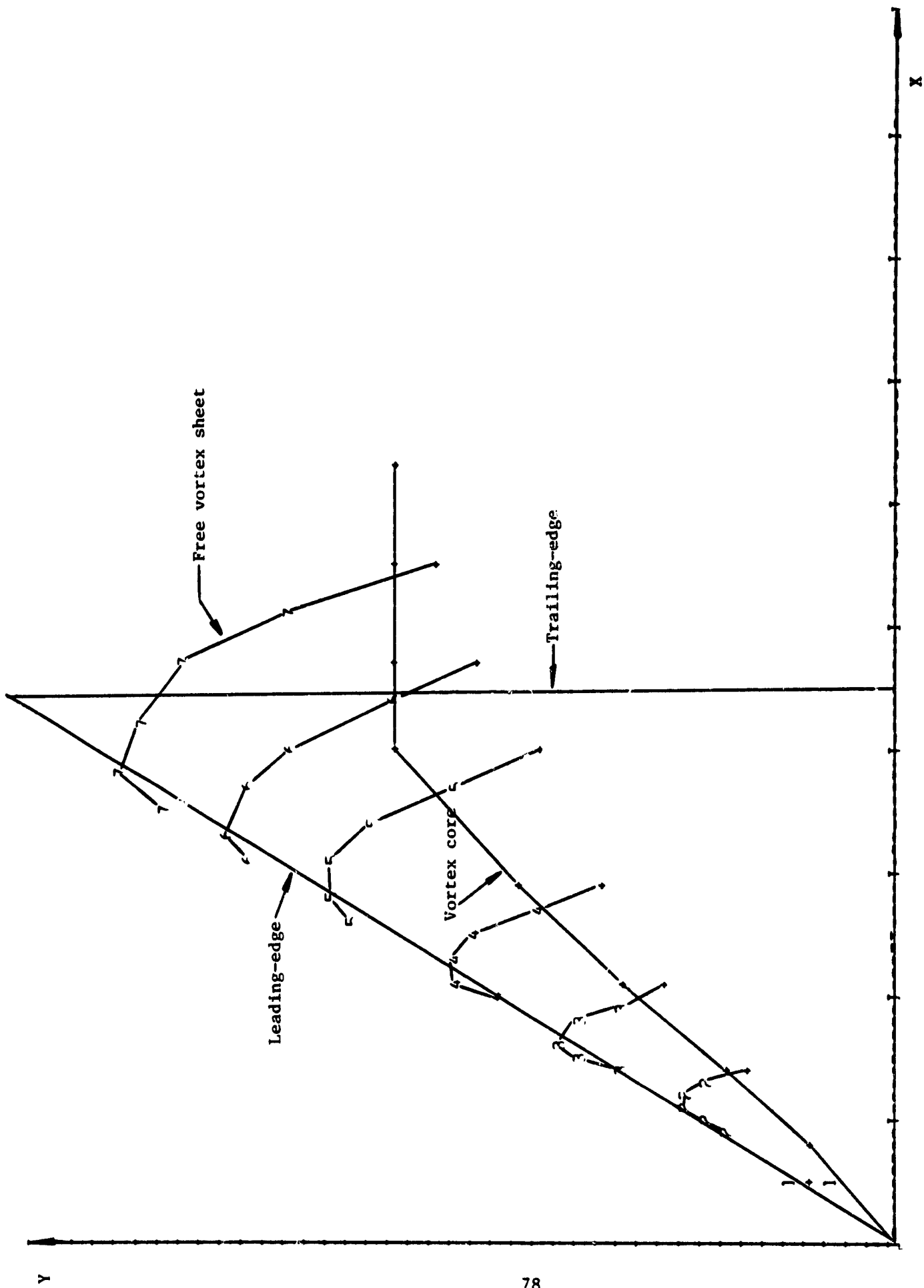
(a) Top view

Figure 6.- Mathematical Model of the initial free sheet and vortex core

78
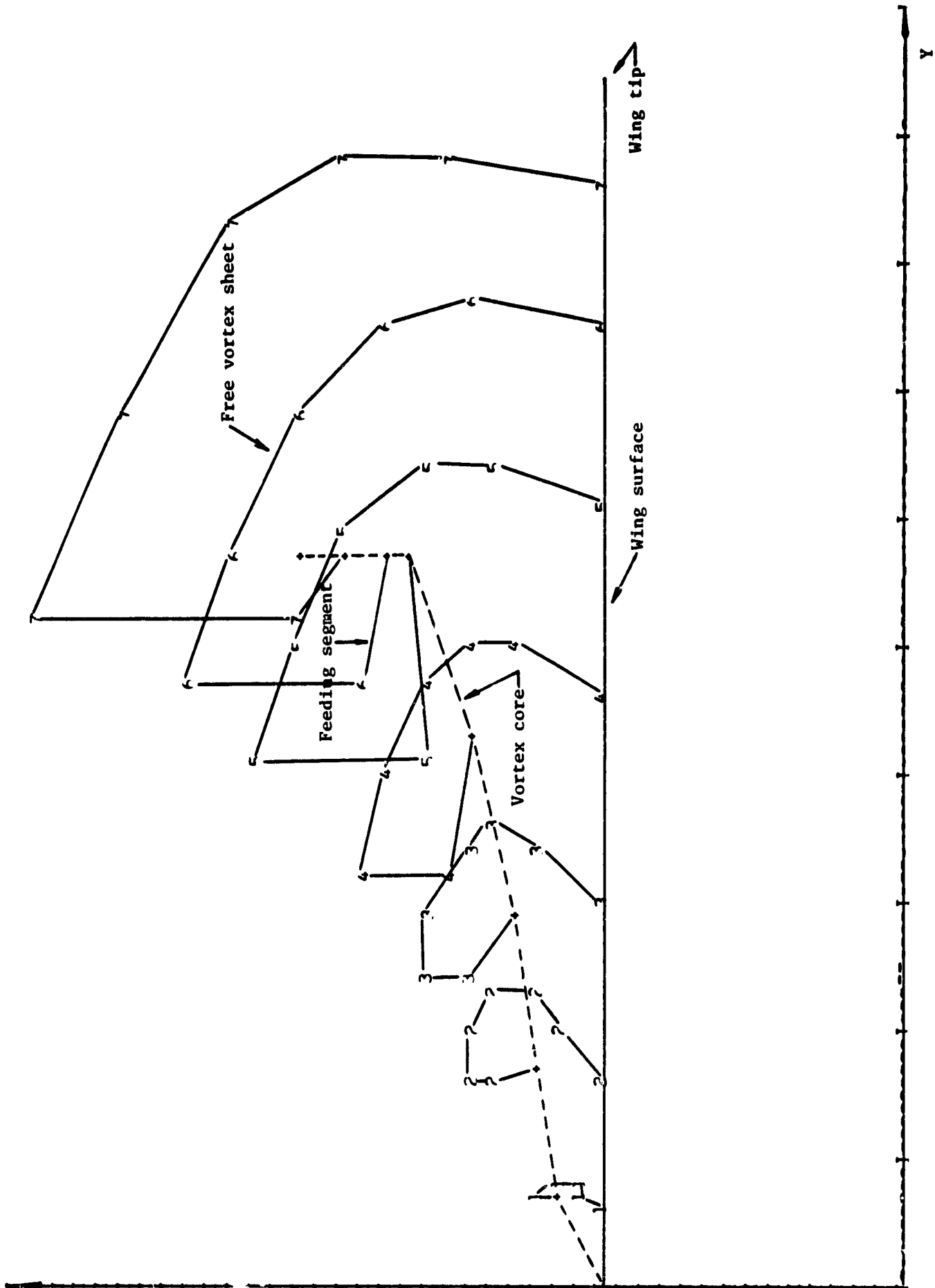
(b) Rear view

Figure 6.- Continued.

79
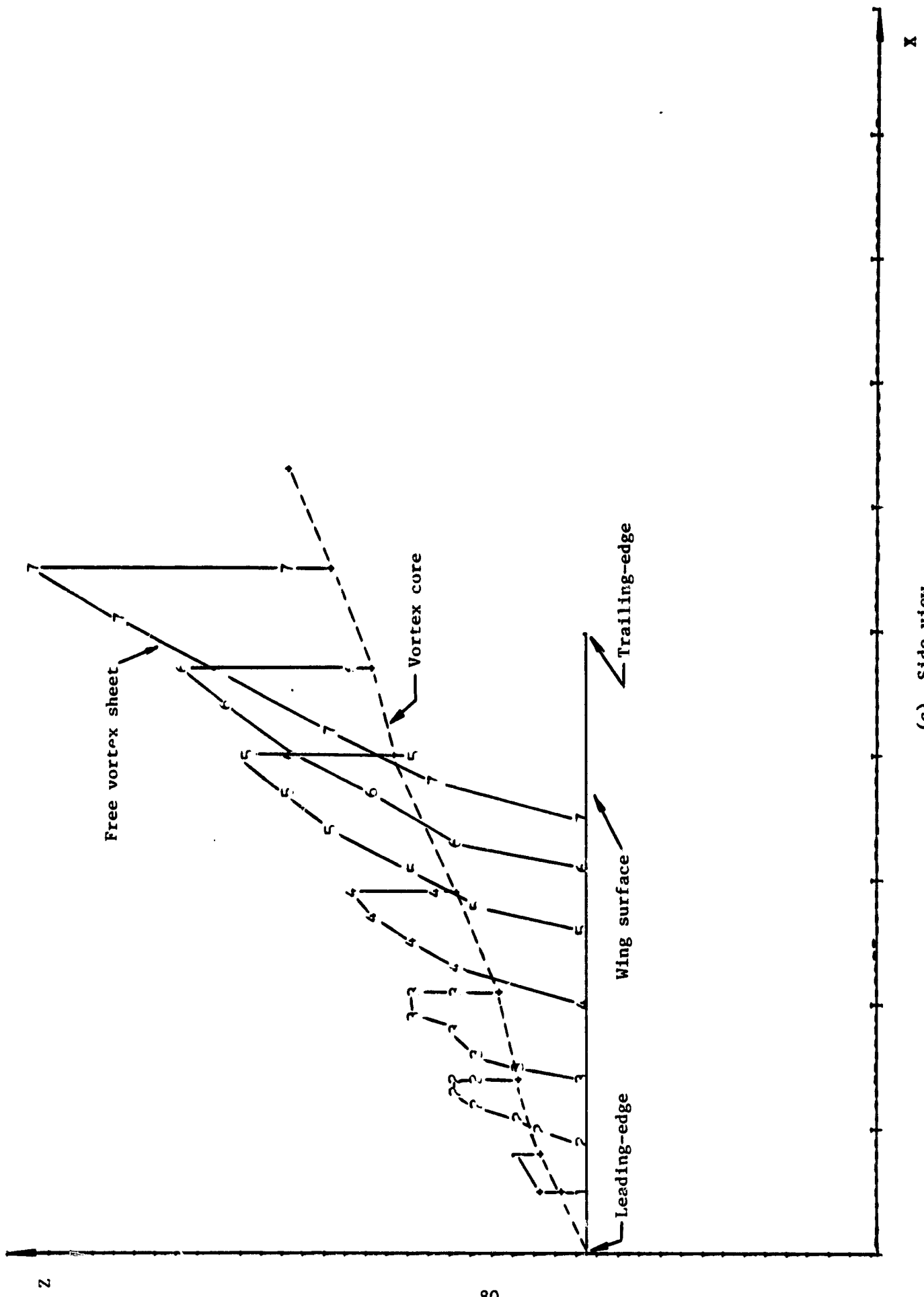
(c) Side view

Figure 6.- Concluded.
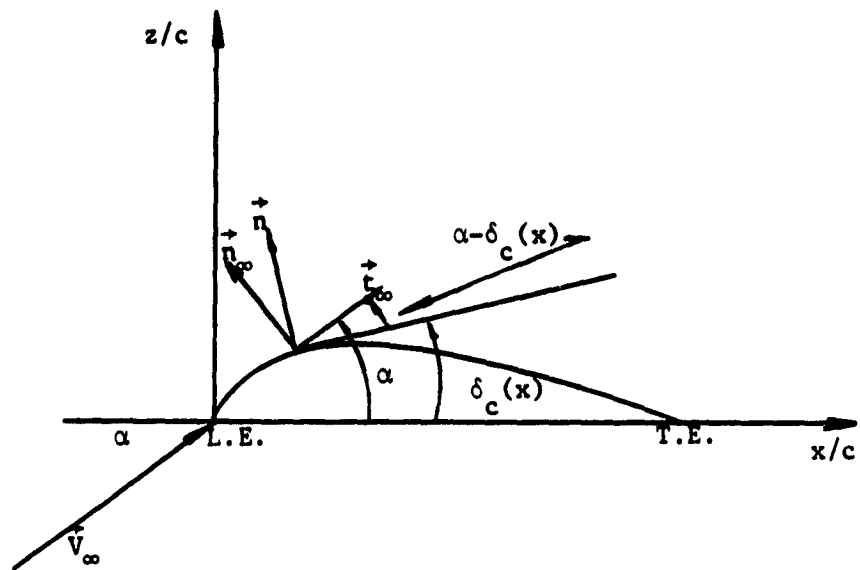
Figure 7.- Lifting pressure components on the wing camber surface
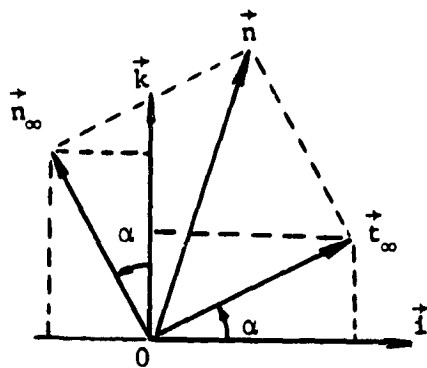
Figure 3.- Definition of $\vec{n}_\infty$ and $\vec{t}_\infty$
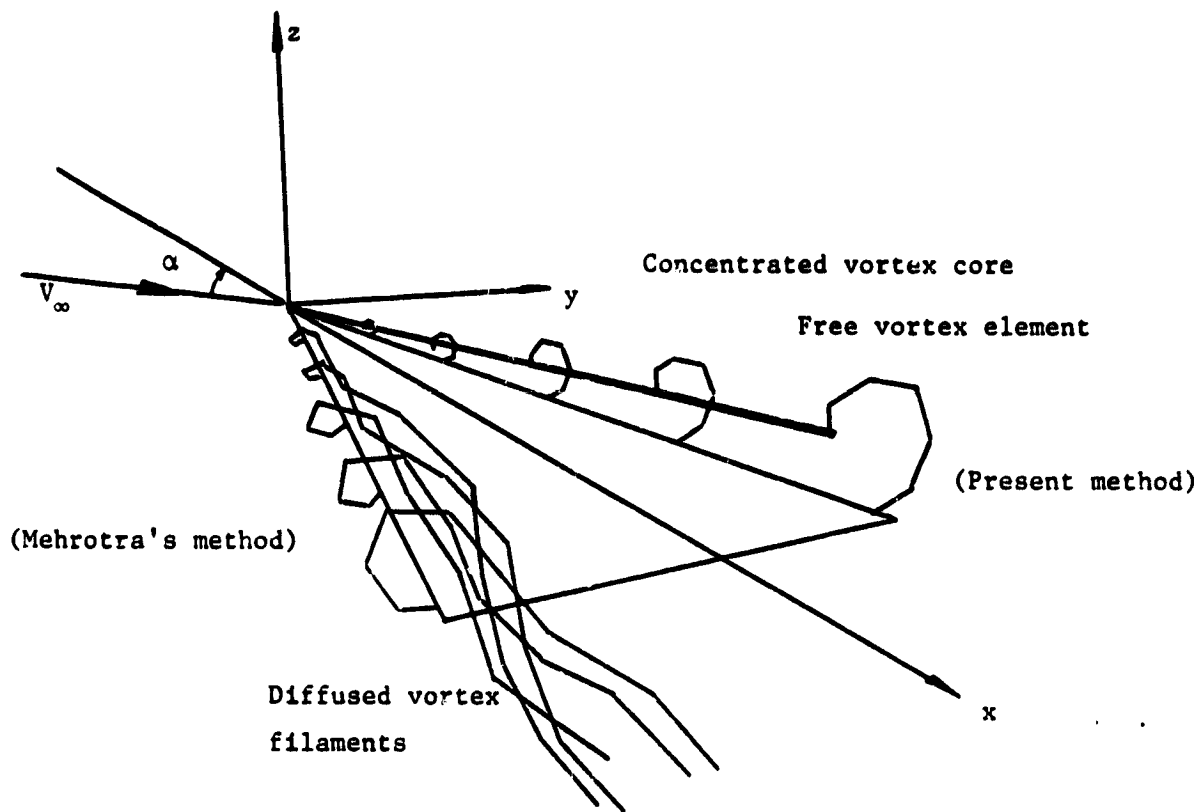
Figure 9.- Sketch of diffused vortex filament and vortex core
models
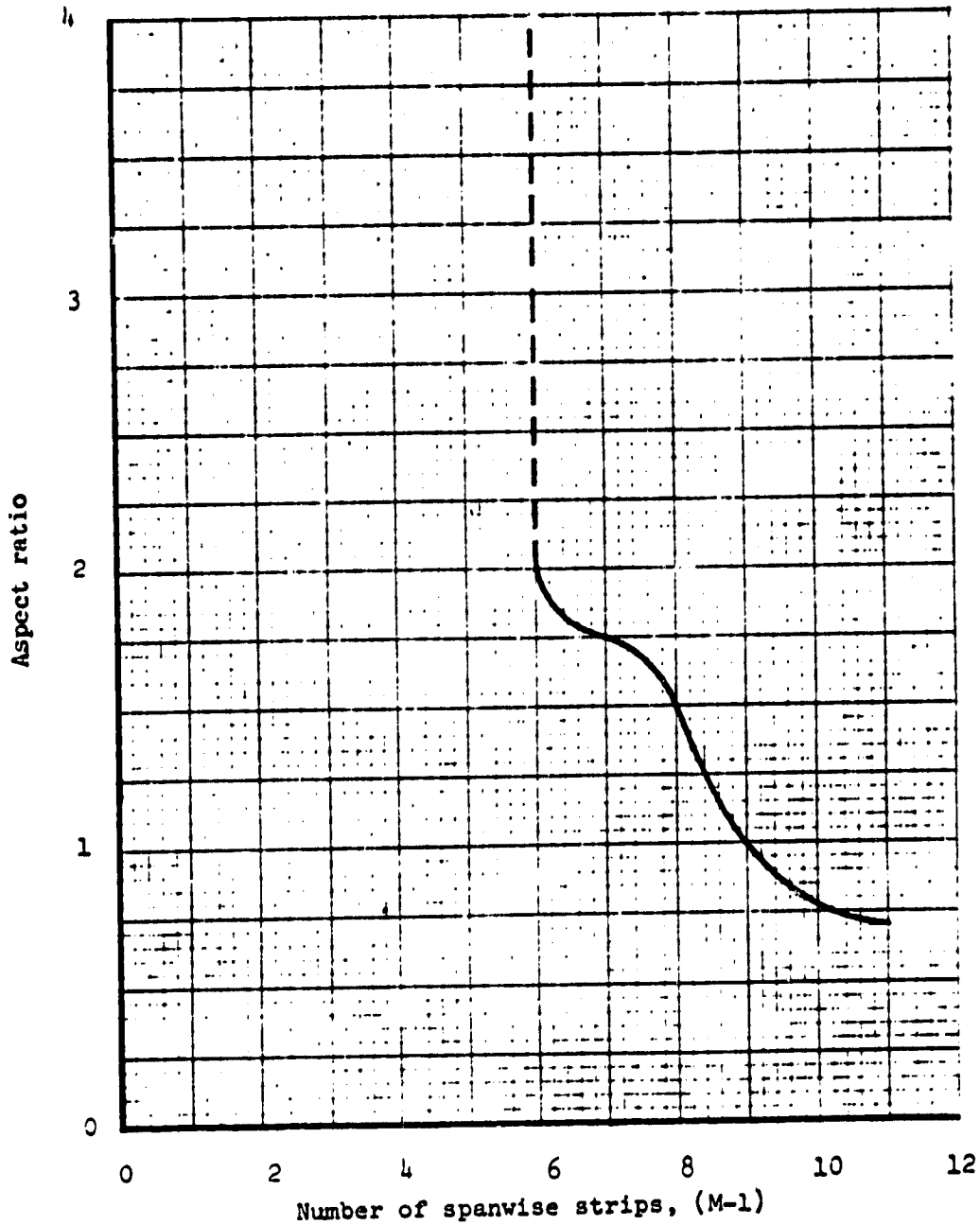
Figure 10.- Variation of number of spanwise strips with aspect ratio for simple delta wings
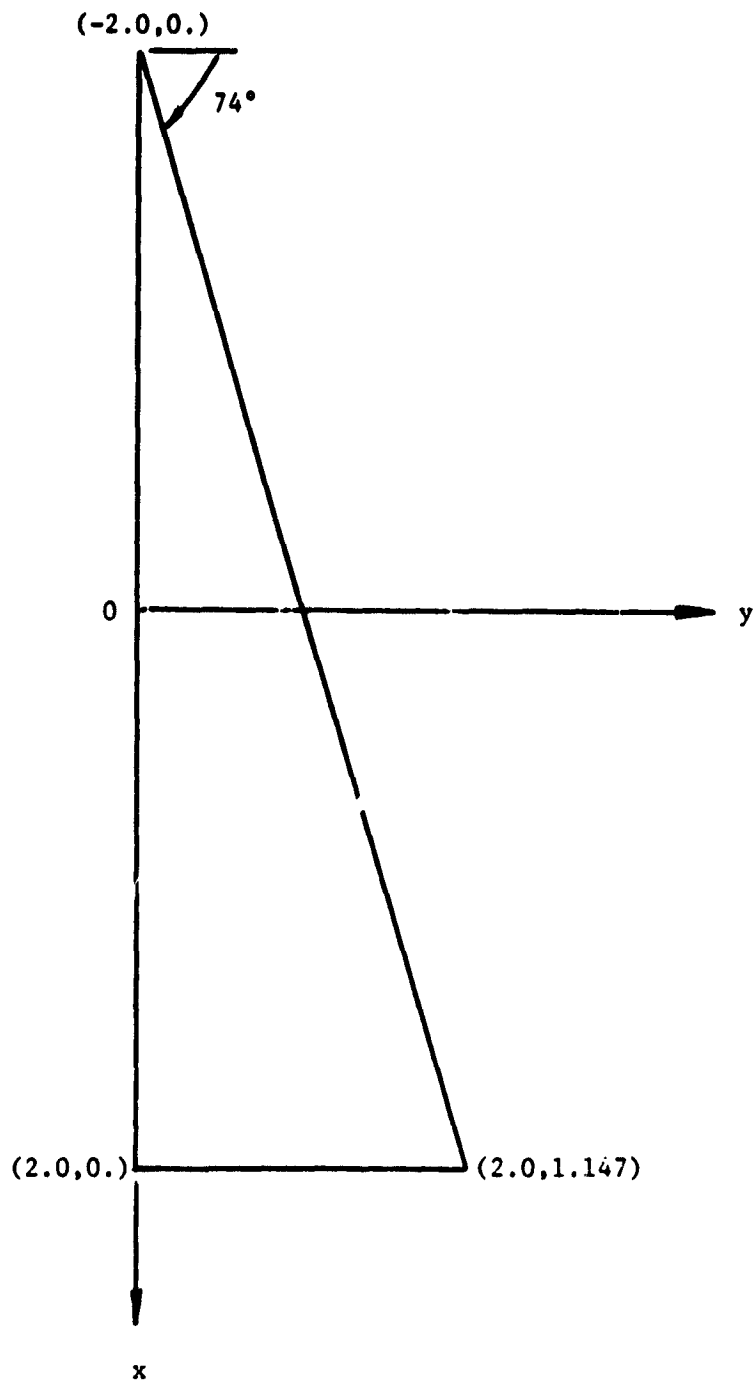
Figure 11.- Geometry of Flat Delta Wing
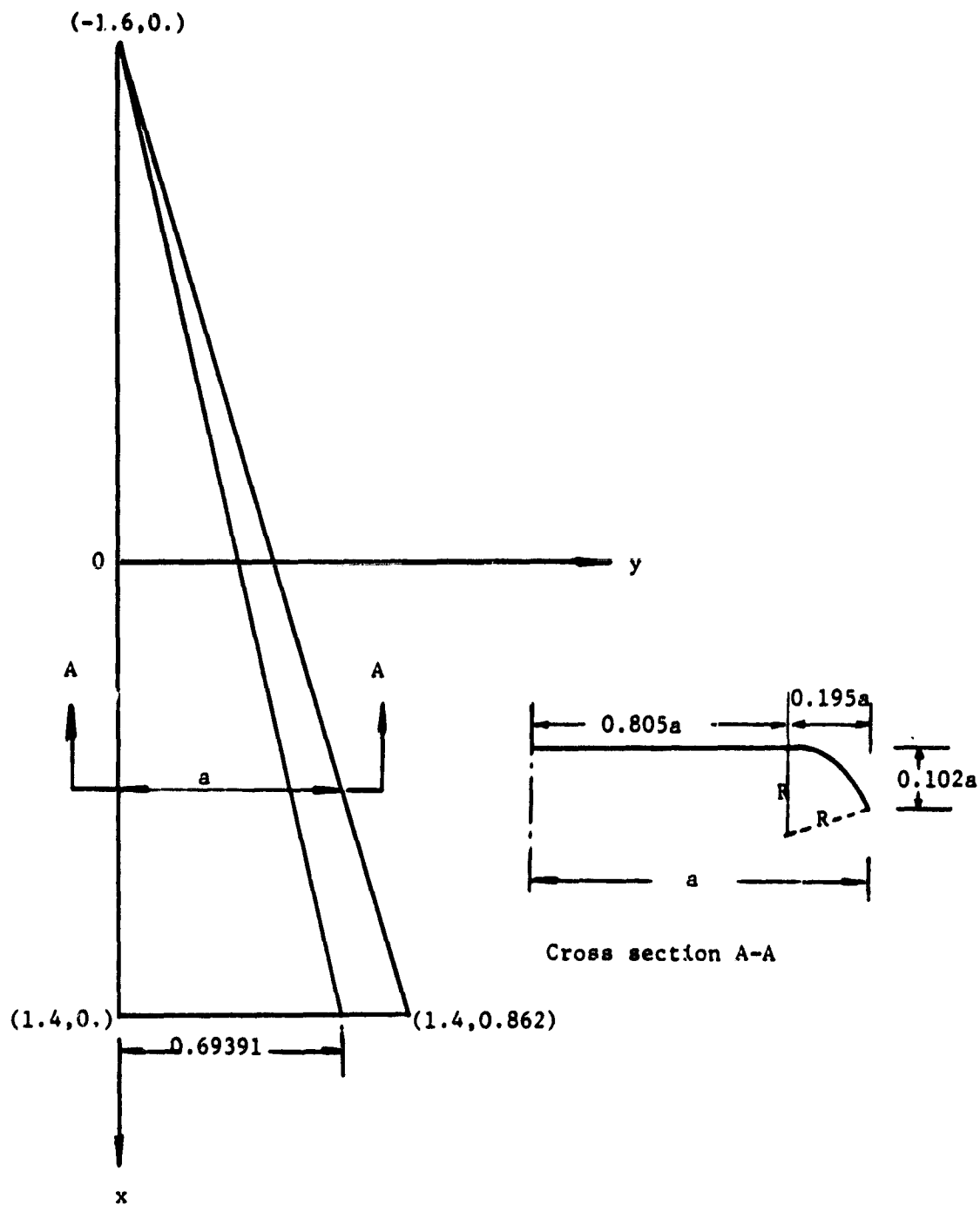
Figure 12.- Geometry of a Delta Wing with Conical Camber
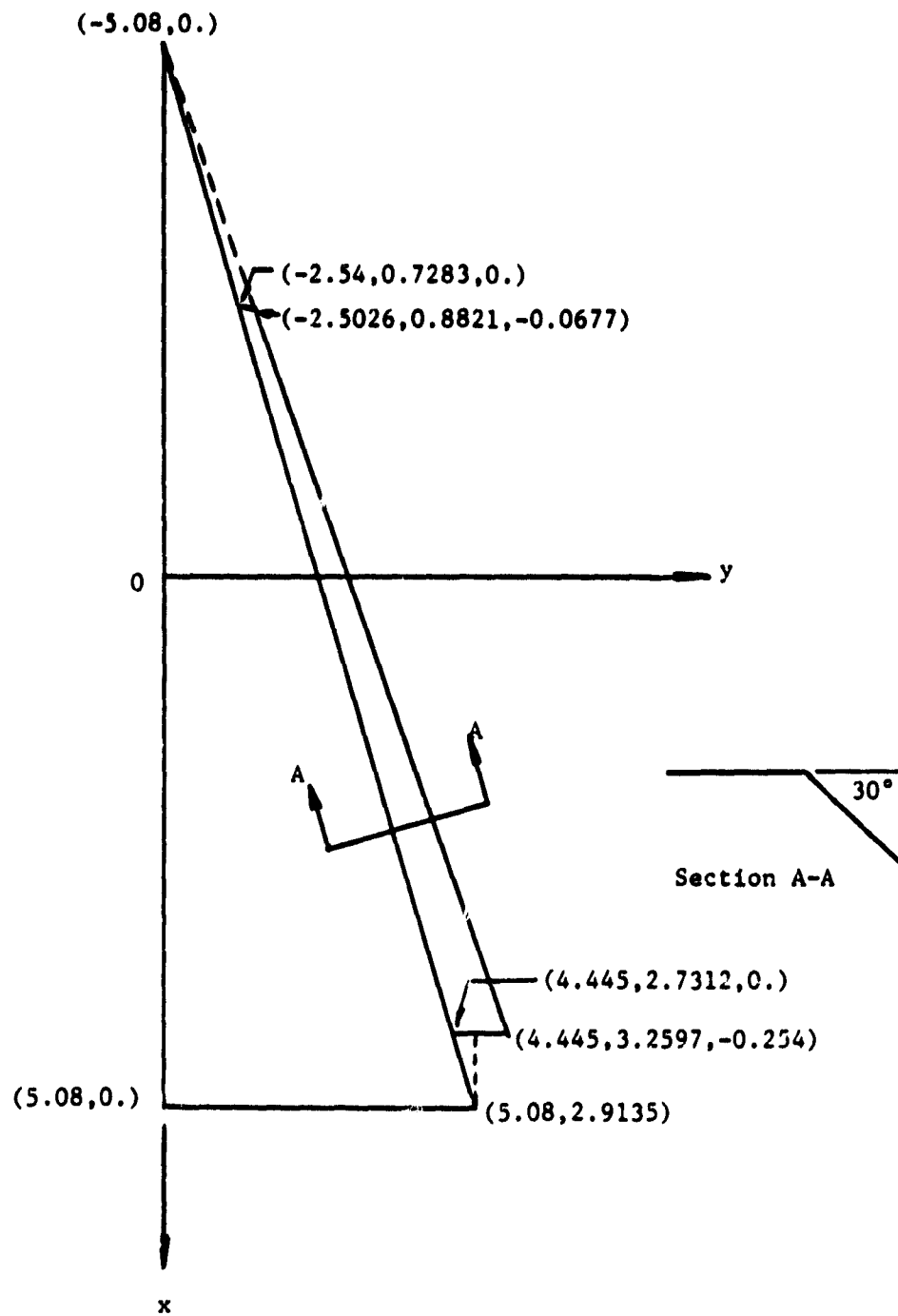
Figure 13.- Geometry of a 74°-Delta Wing with Leading-edge
Vortex Flap
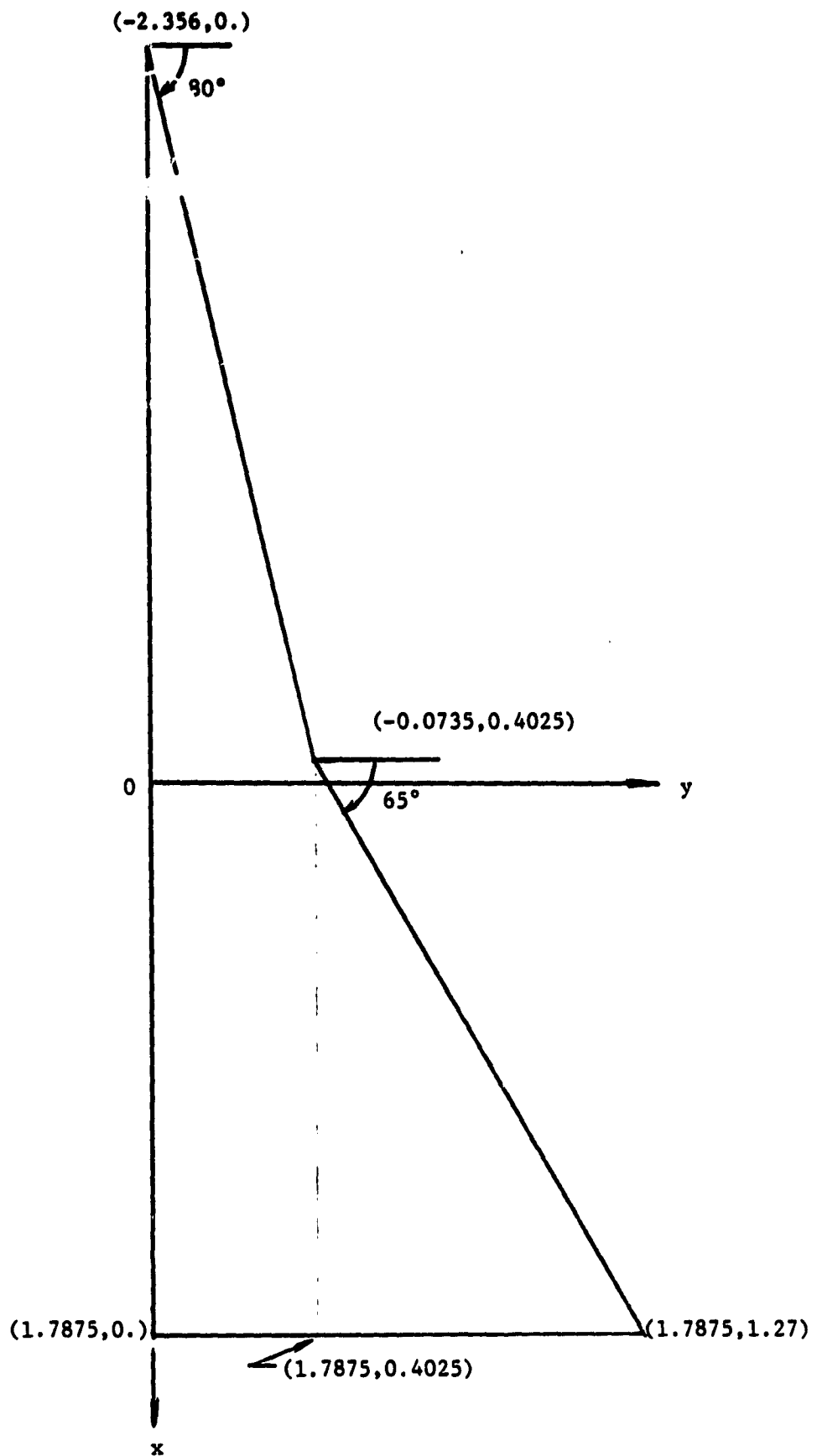
Figure 14.- Geometry of a Double Delta Wing

87
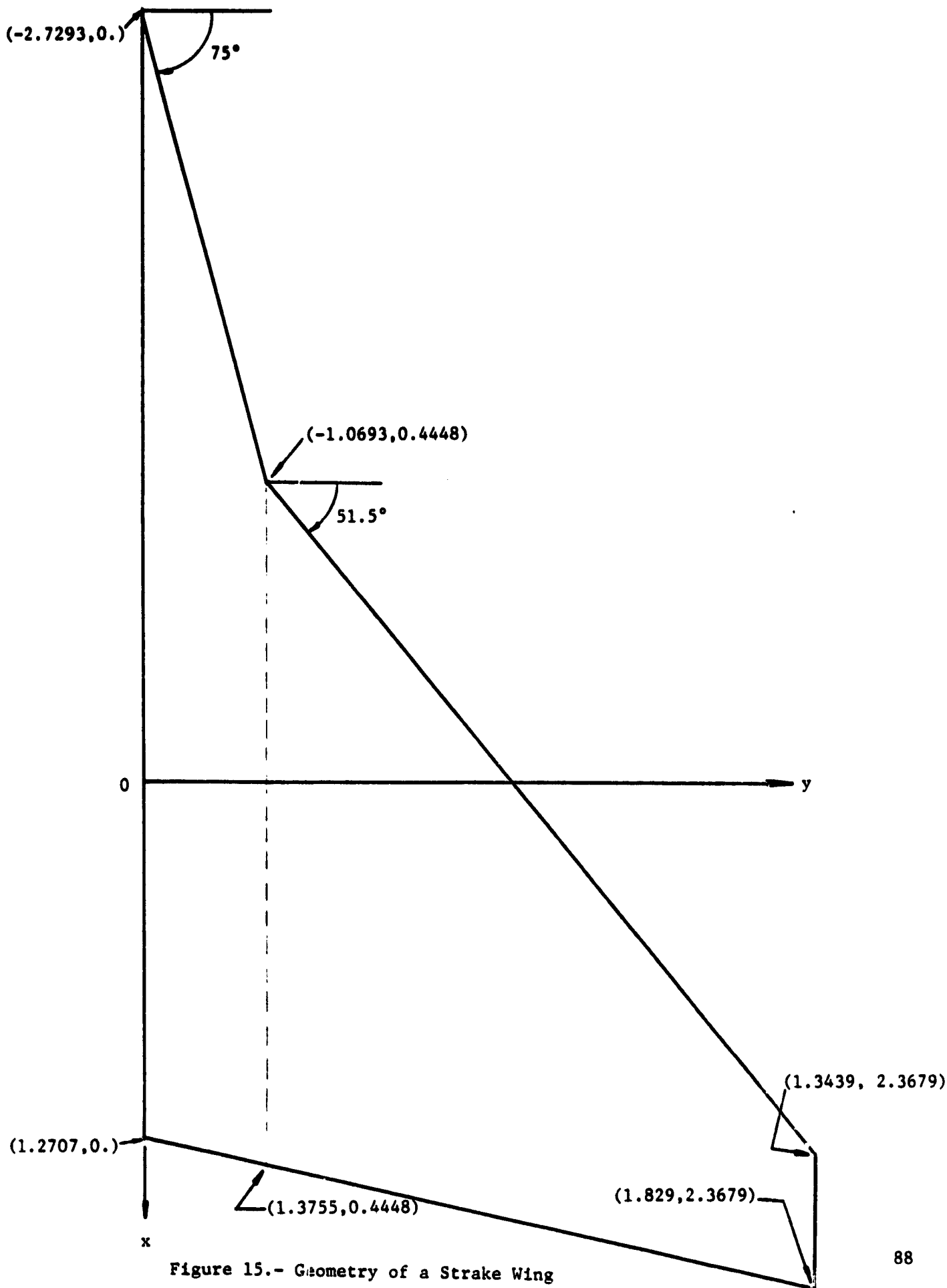
Figure 15.- Geometry of a Strake Wing

88
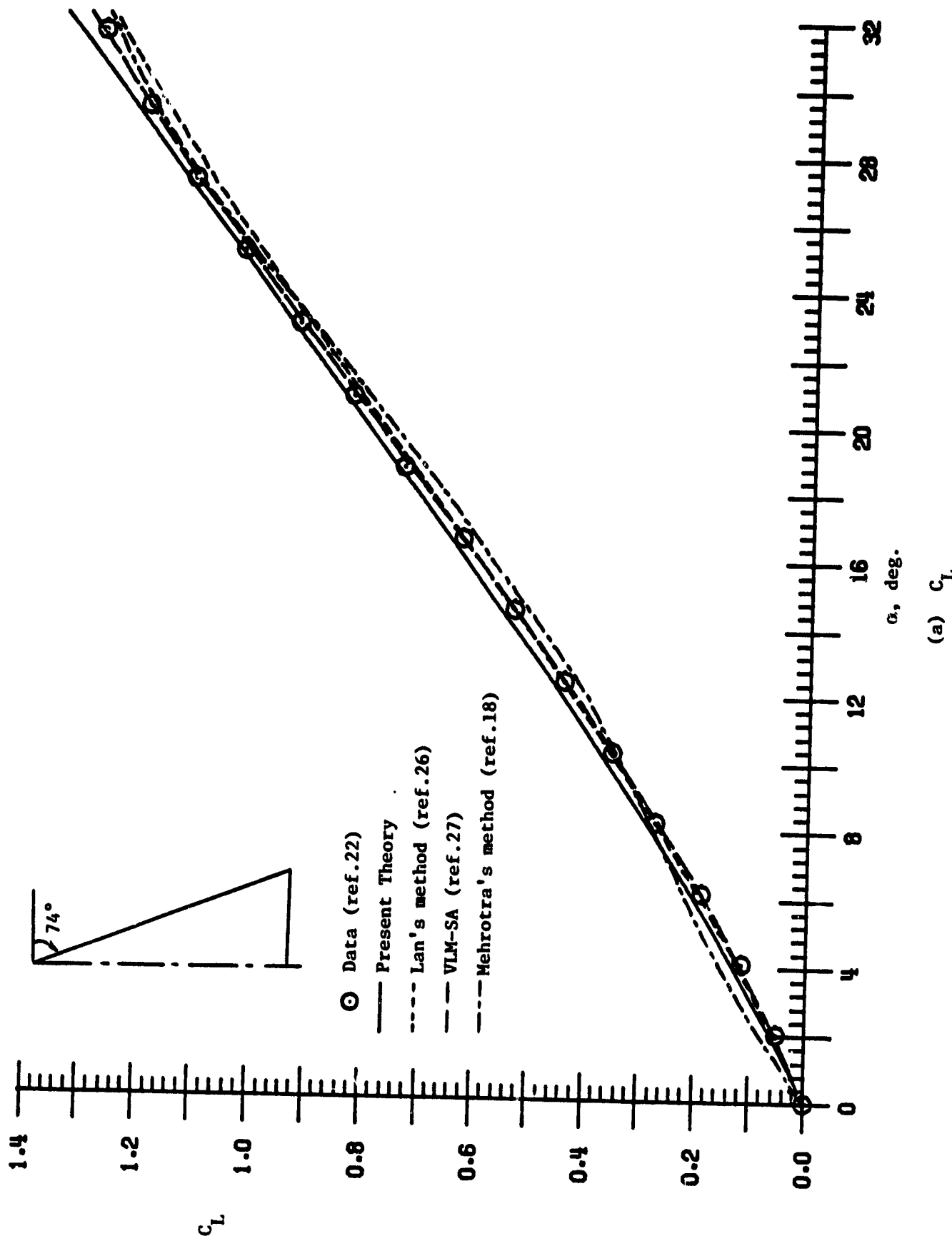
Figure 16.- Longitudinal Aerodynamic Characteristics of a AR = 1.147 Flat Delta wing; M = 0.

(a) C_L

Data (ref.22)
Present Theory
Lan's method (ref.26)
VLM-SA (ref.27)
Mehrotra's method (ref.18)

89
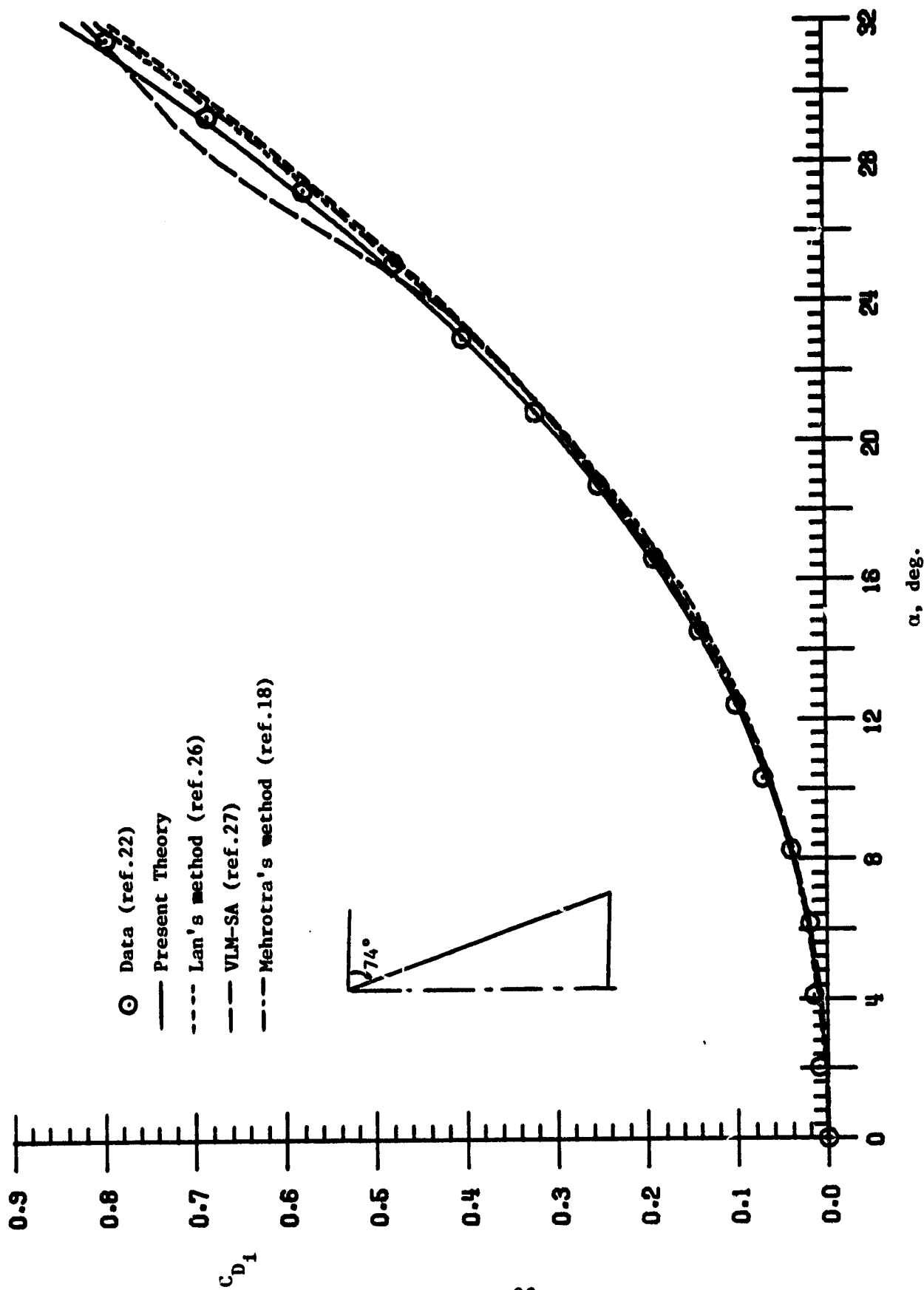
(b) C_{D_1}

Figure 16.- Continued.
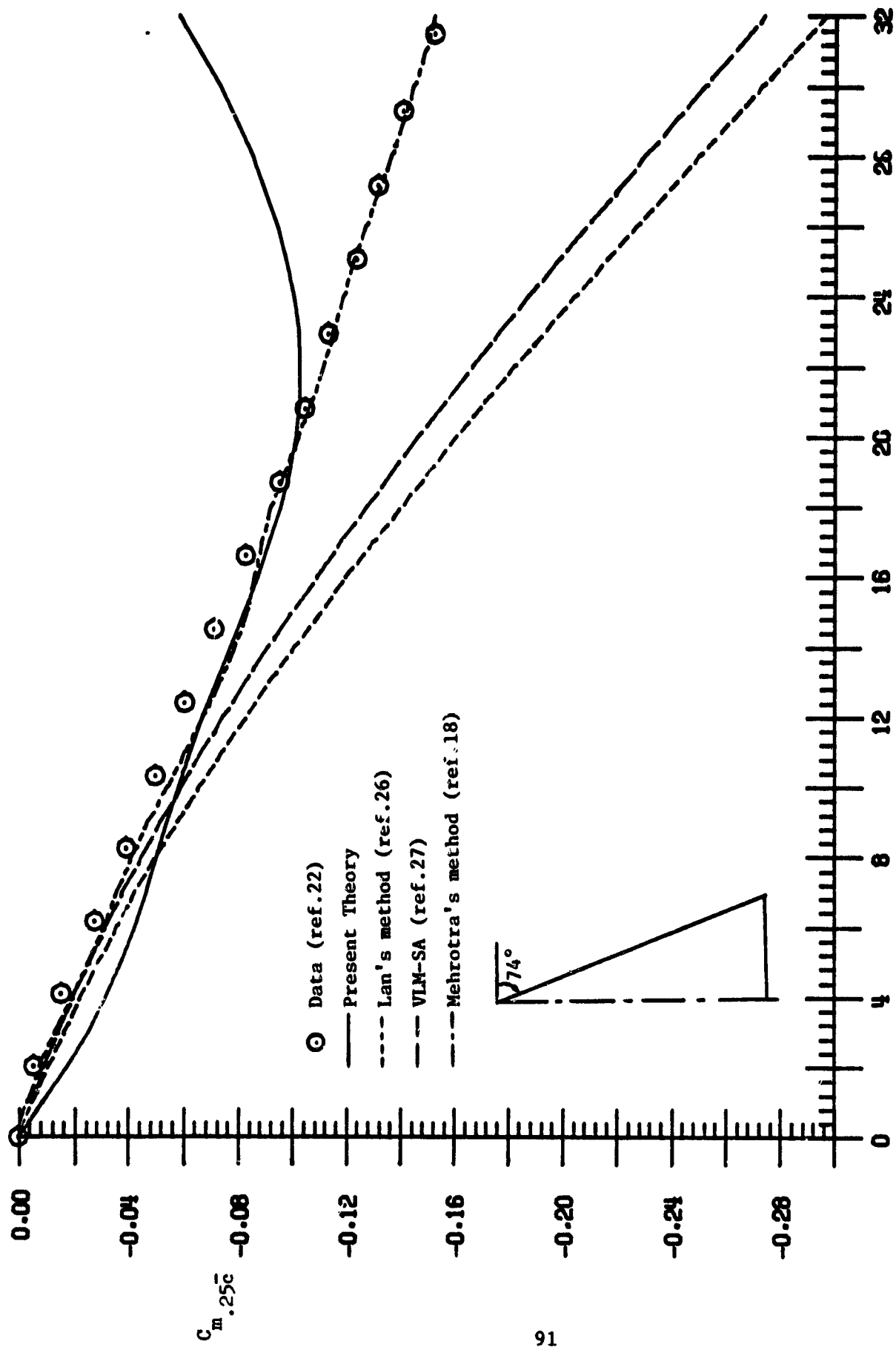
(c) C_m

Figure 16.- Concluded.

91
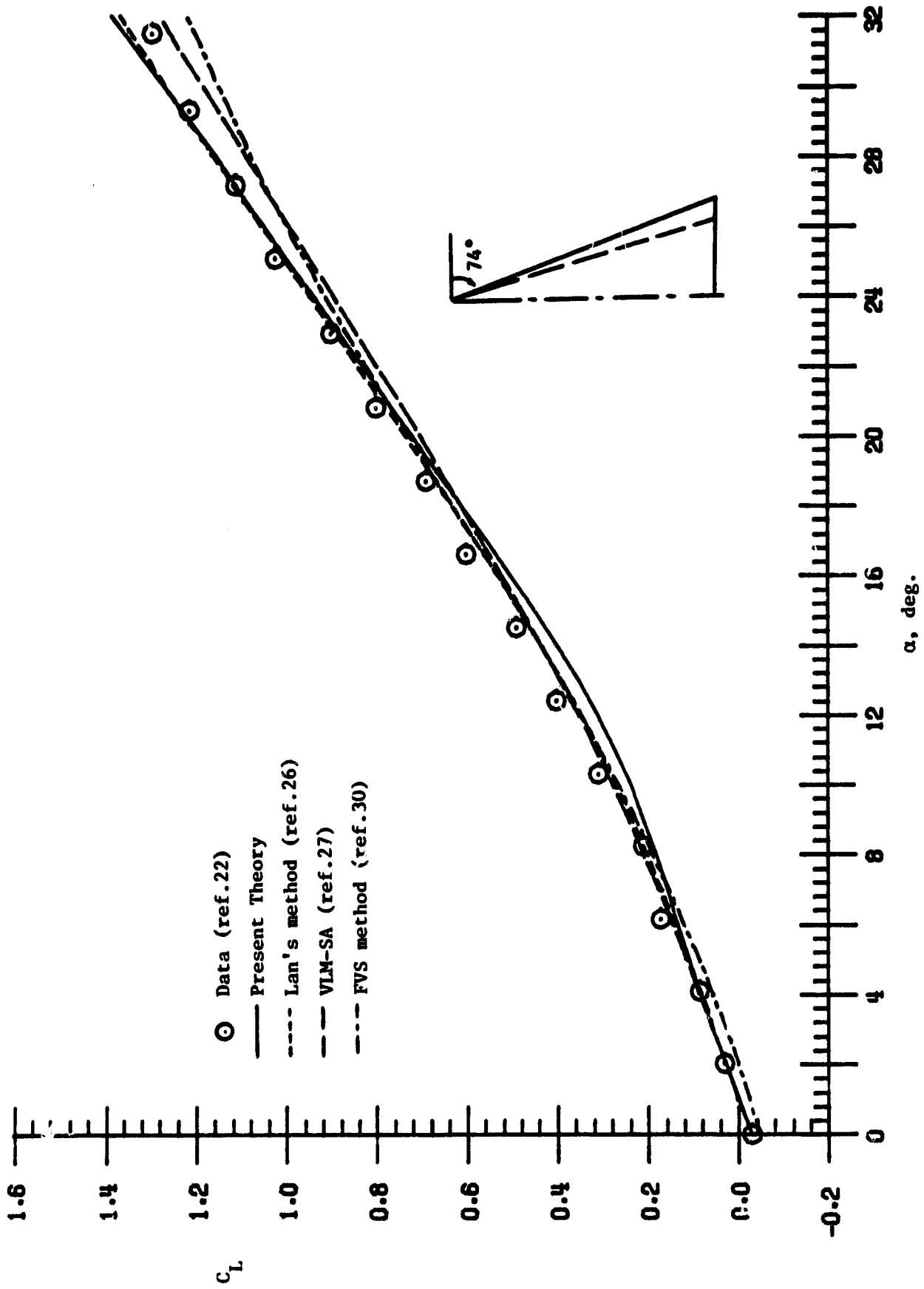
Figure 17.- Longitudinal Aerodynamic Characteristics of a a AR = 1.1493 Conical Cambered Delta;

(a) C_L

$M = 0.$

(b) C_{D_i}
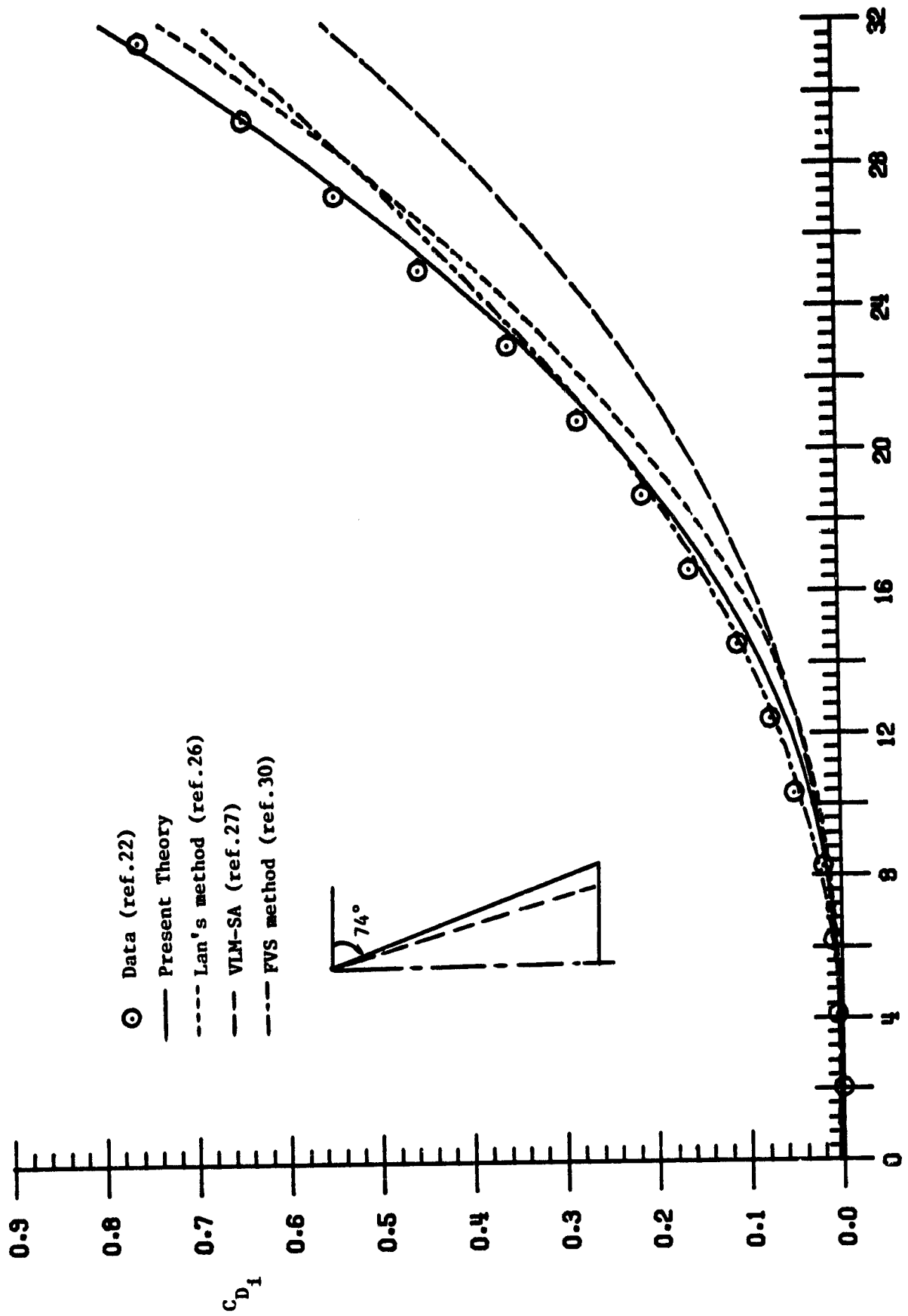
Figure 17.- Continued.

93
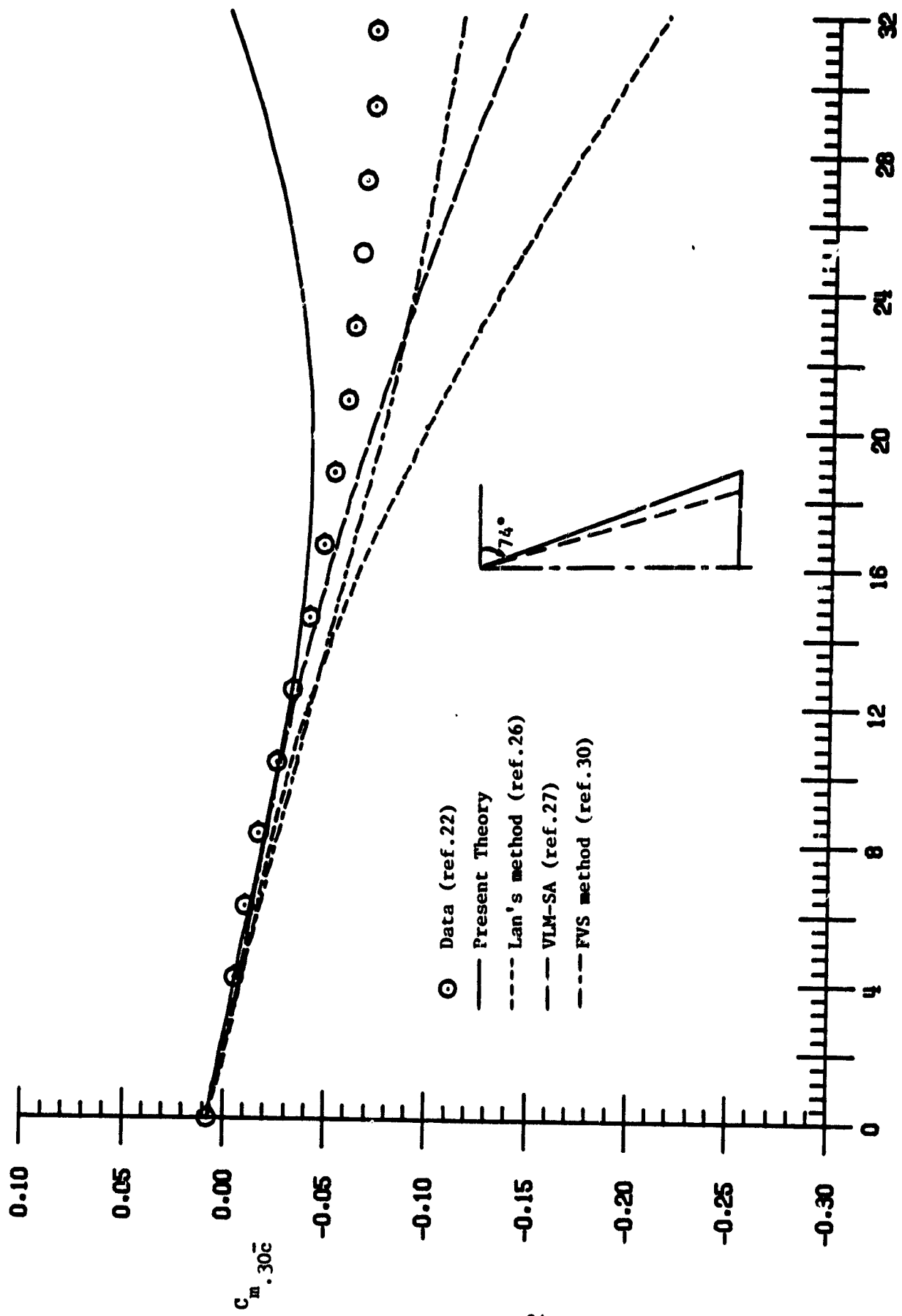
(c) C_m

Figure 17.- Concluded.

94
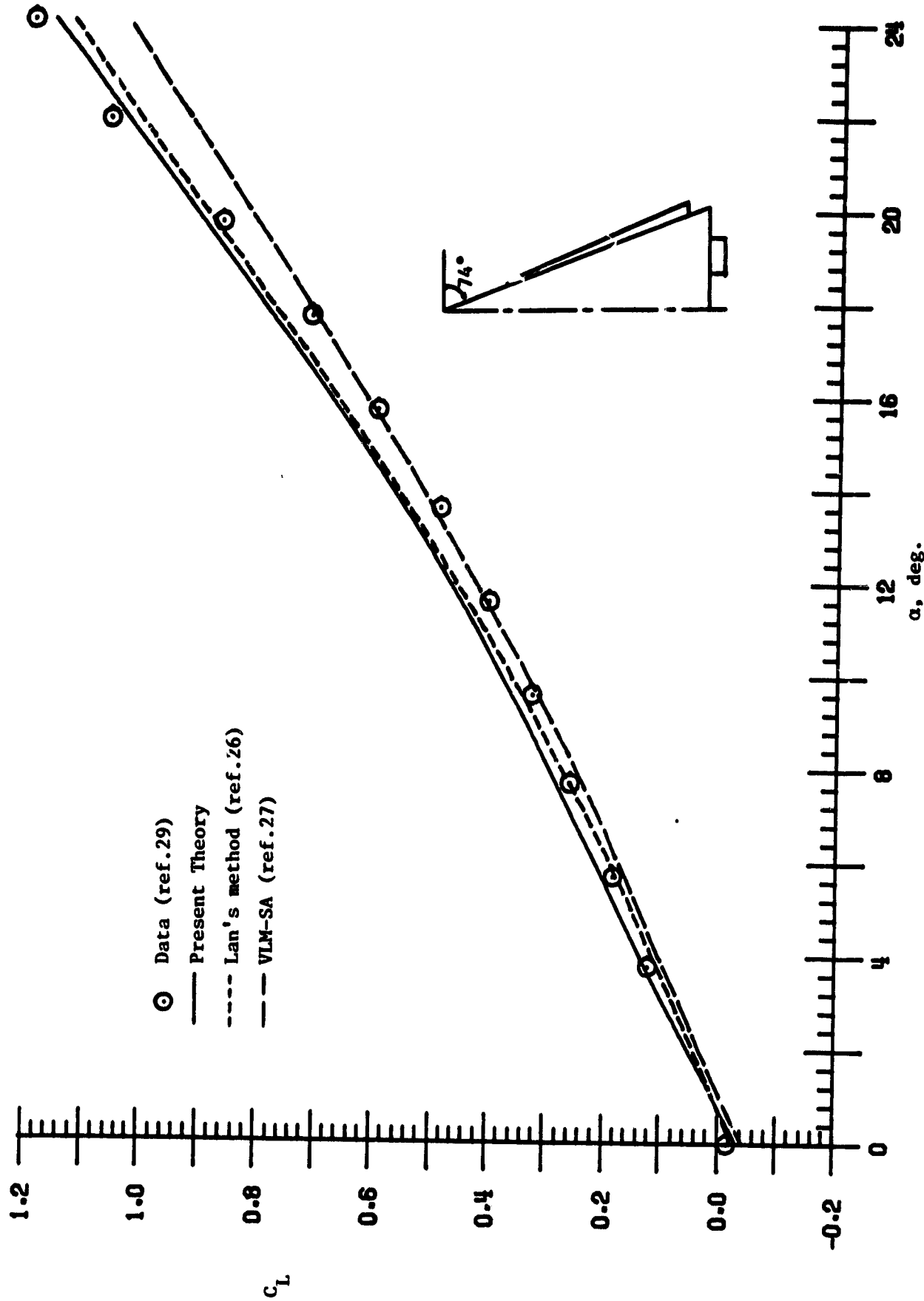
Figure 18.- Longitudinal Aerodynamic Characteristics of a AR = 1.147 Delta Wing with a

○ Data (ref.29)
—— Present Theory
---- Lan's method (ref.26)
—— VLM-SA (ref.27)

(a) C_L

(b) c_{D_i}
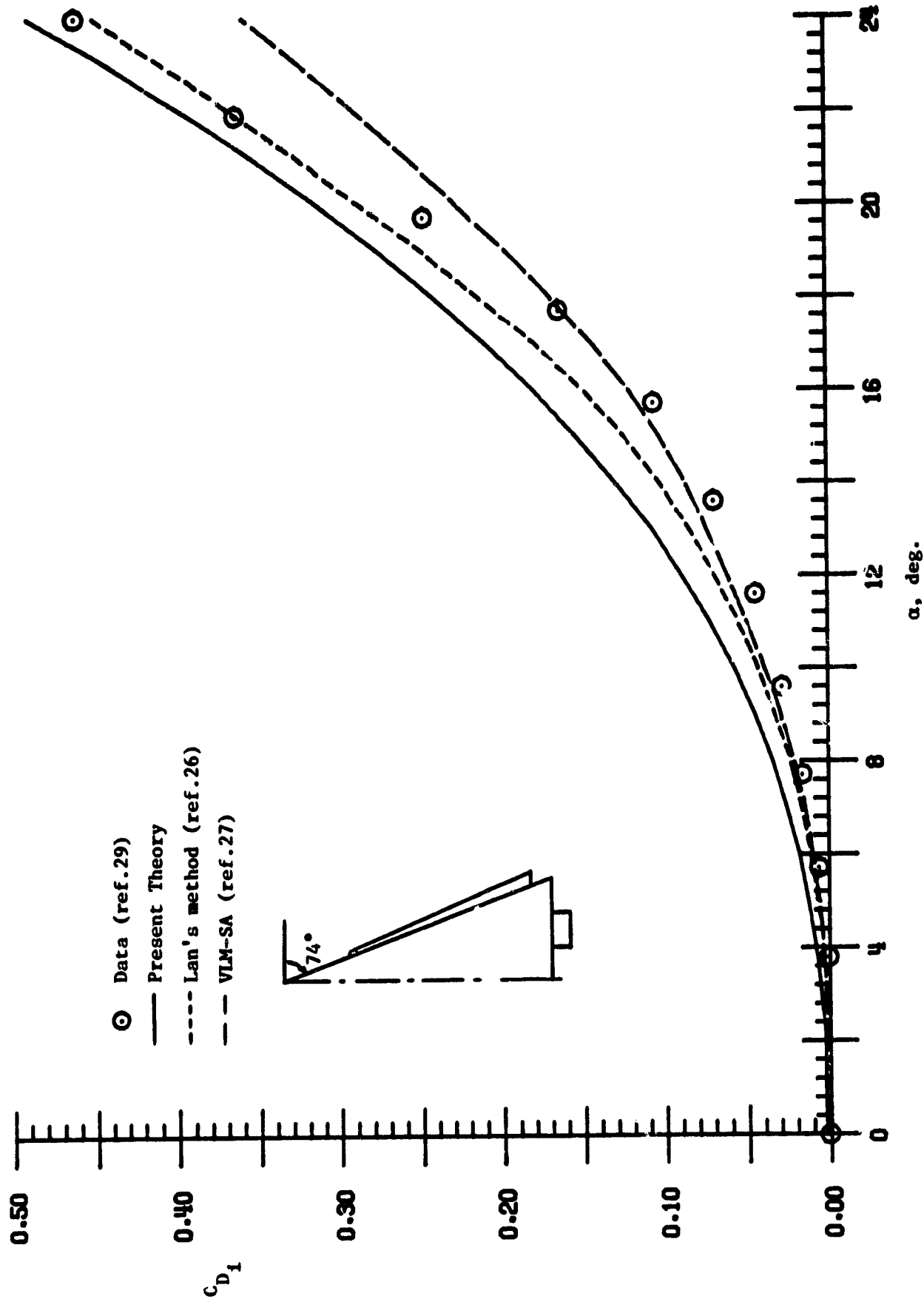
Figure 18.- Continued.

Legend:
⊙ Data (ref.29)
— Present Theory
--- Lan's method (ref.26)
—— VLM-SA (ref.27)
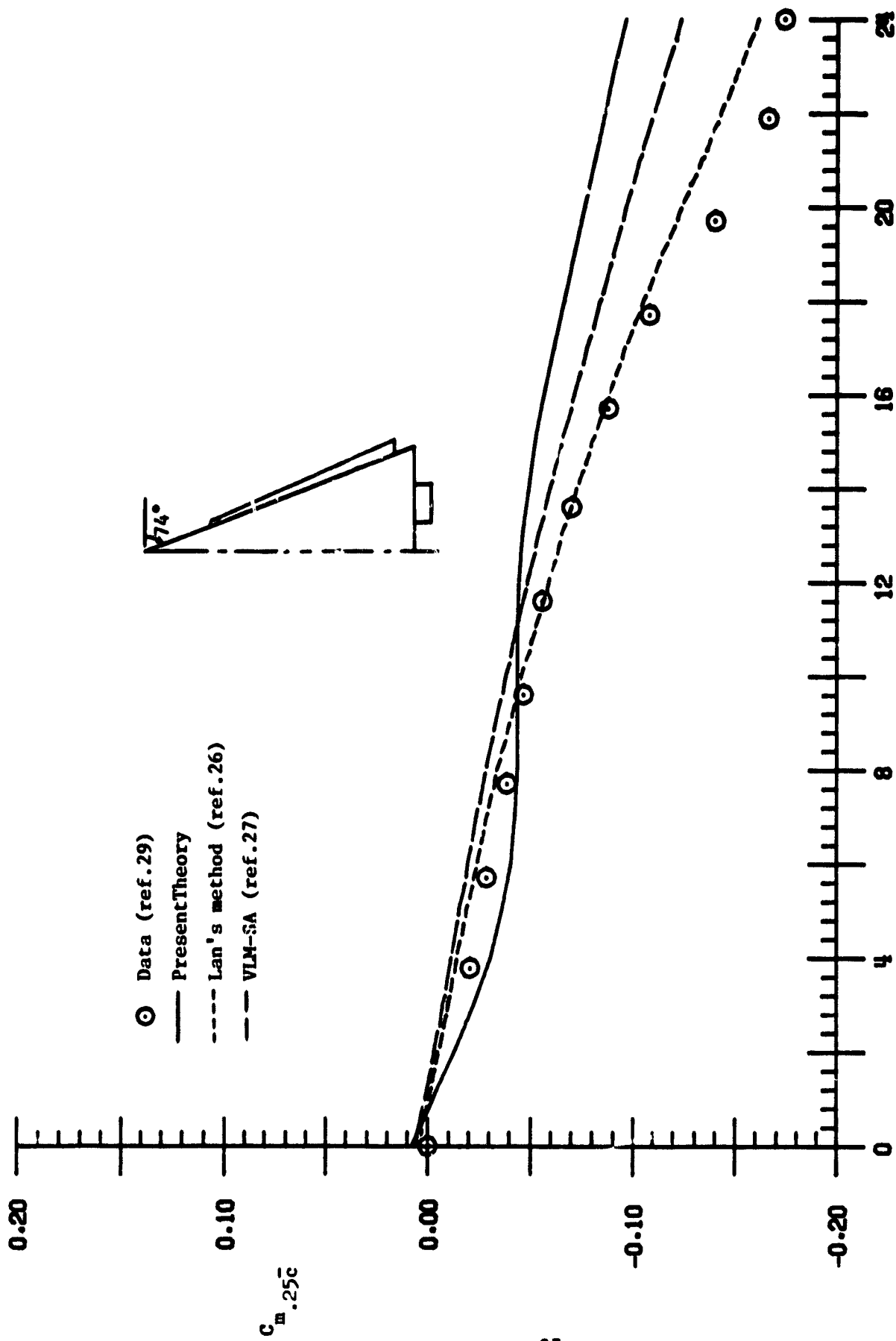
(c) C_m

Figure 18.- Concluded.

97
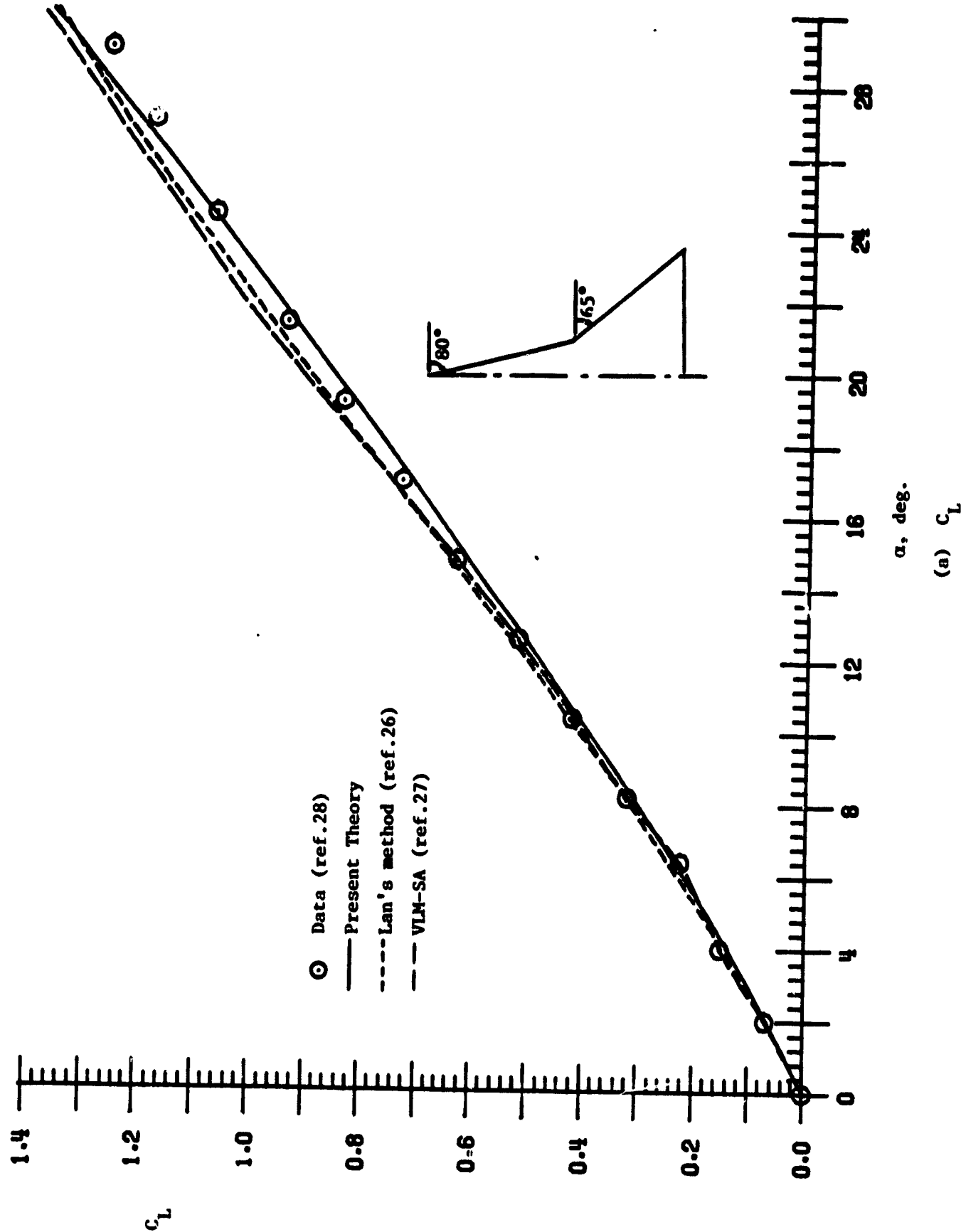
Figure 19.- Longitudinal Aerodynamic Characteristics of a Double Delta Wing; M = 0.

(a) C_L

(b) C_{D_i}

Figure 19.- Continued.

99

Figure 19.- Concluded.

(c) C_m

α, deg.

$C_{m.25\bar{c}}$

○ Data (ref.28)
—— Present Theory
--- Lan's method (ref.26)
——— VLM-SA (ref.27)

100
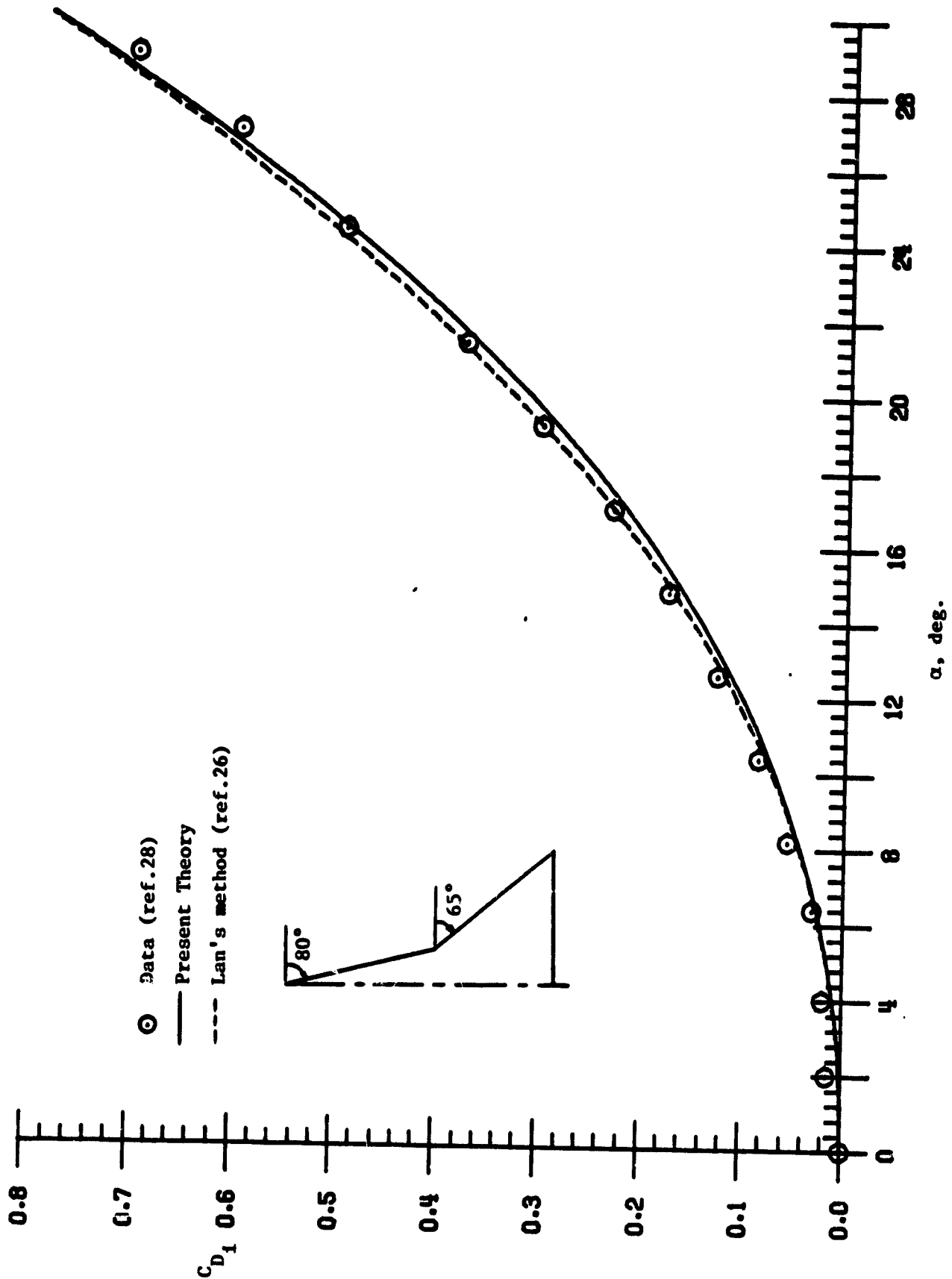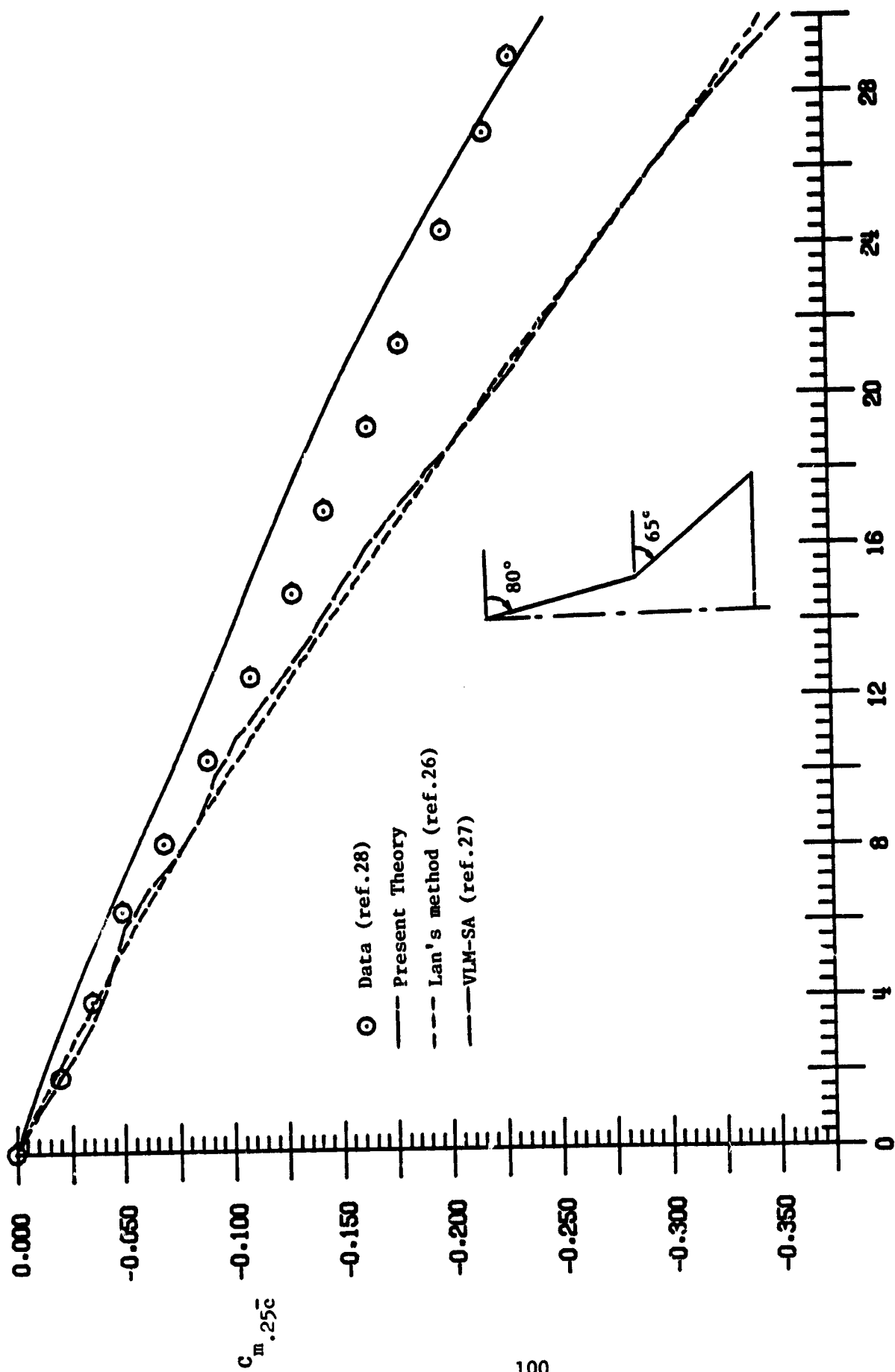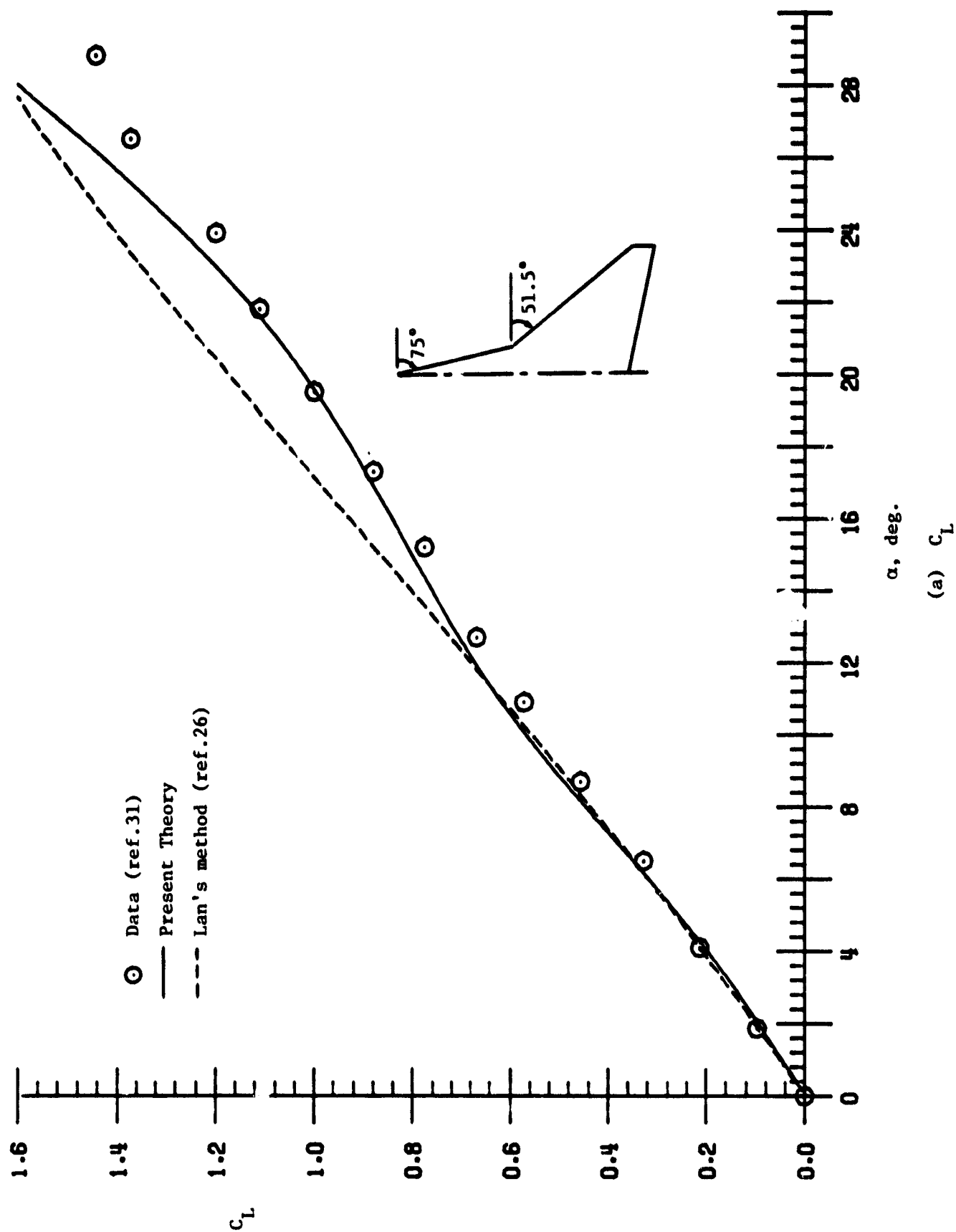
Figure 20.- Longitudinal Aerodynamic Characteristics of a Strake Wing; M = 0.

(a) C_L
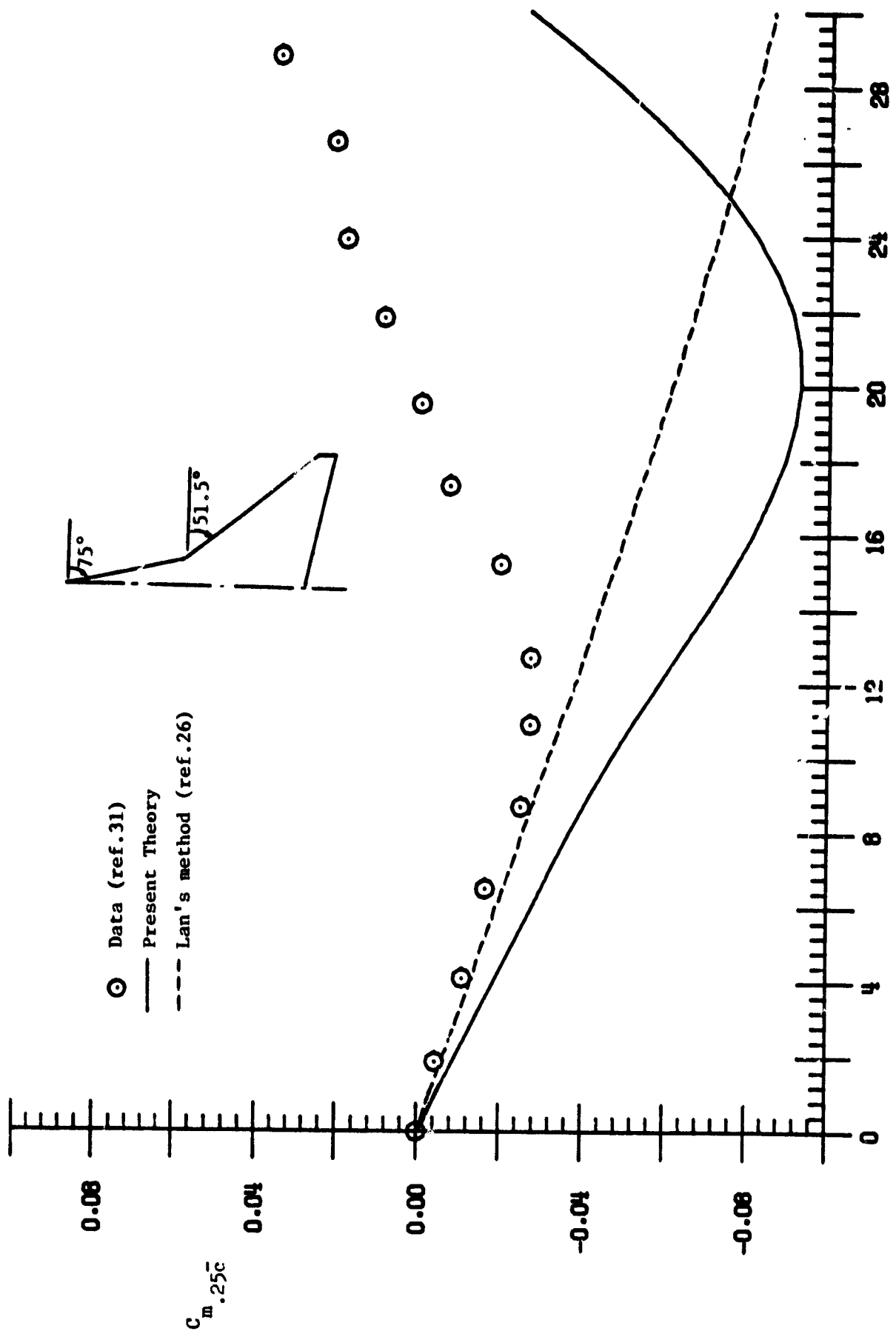
(b) C_m

Figure 20.- Concluded.
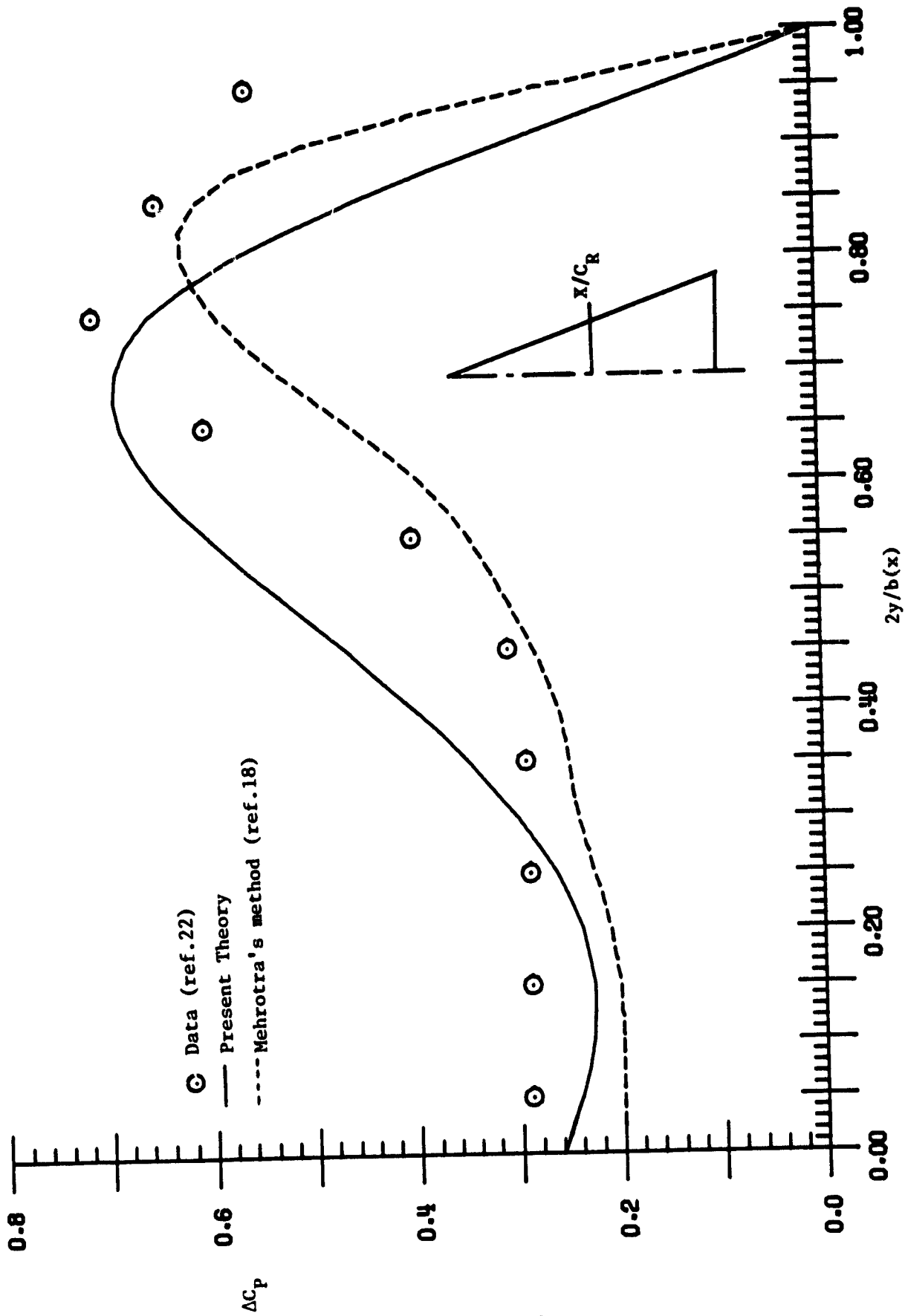
(a) $X/C_R = 0.5333$

Figure 21.- Lifting pressure distribution for AR = 1.147 Flat Delta Wing at
10.2 degree angle of attack; M = 0.

103
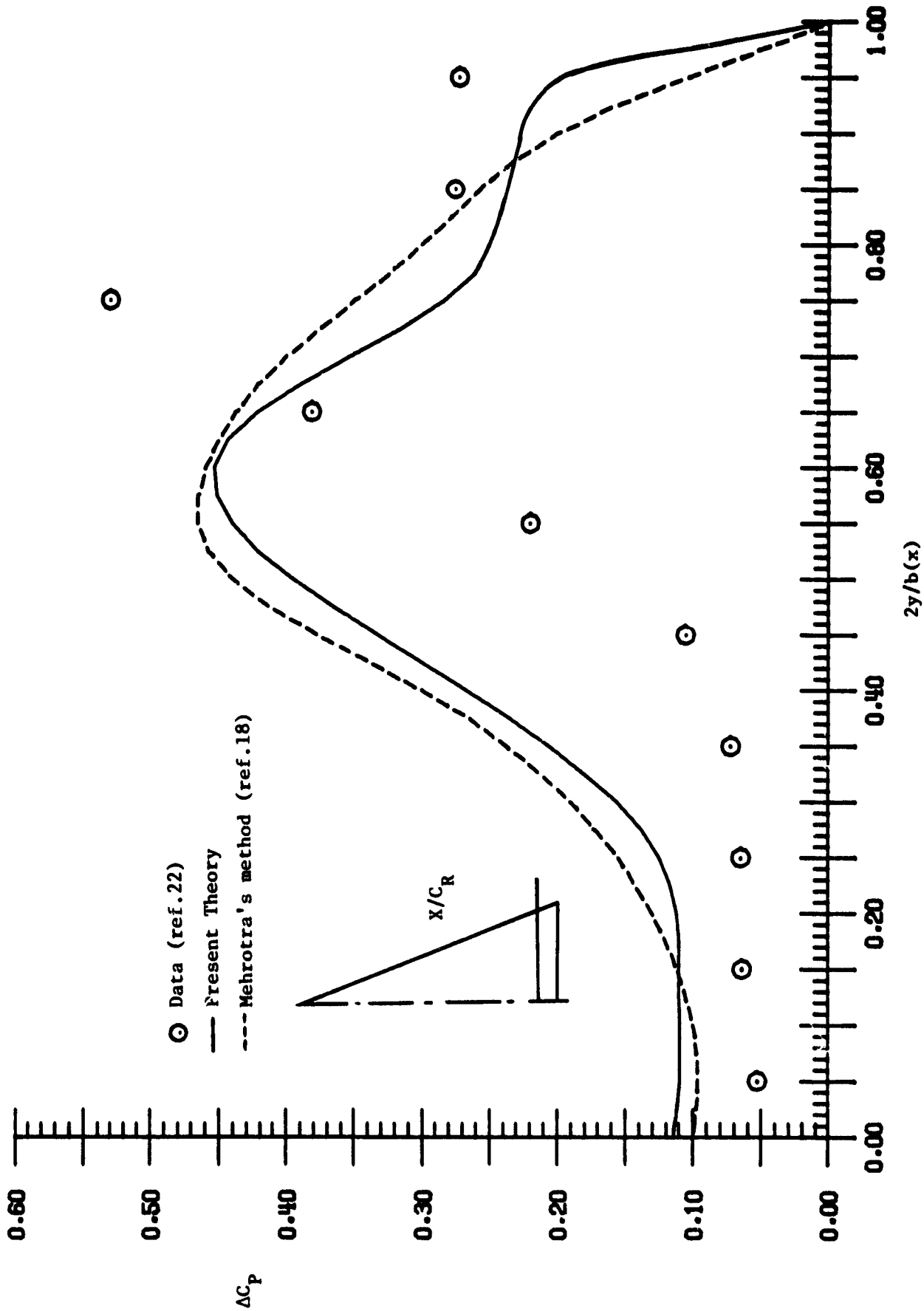
(b) $X/C_R = 0.9333$

Figure 21.- Concluded.
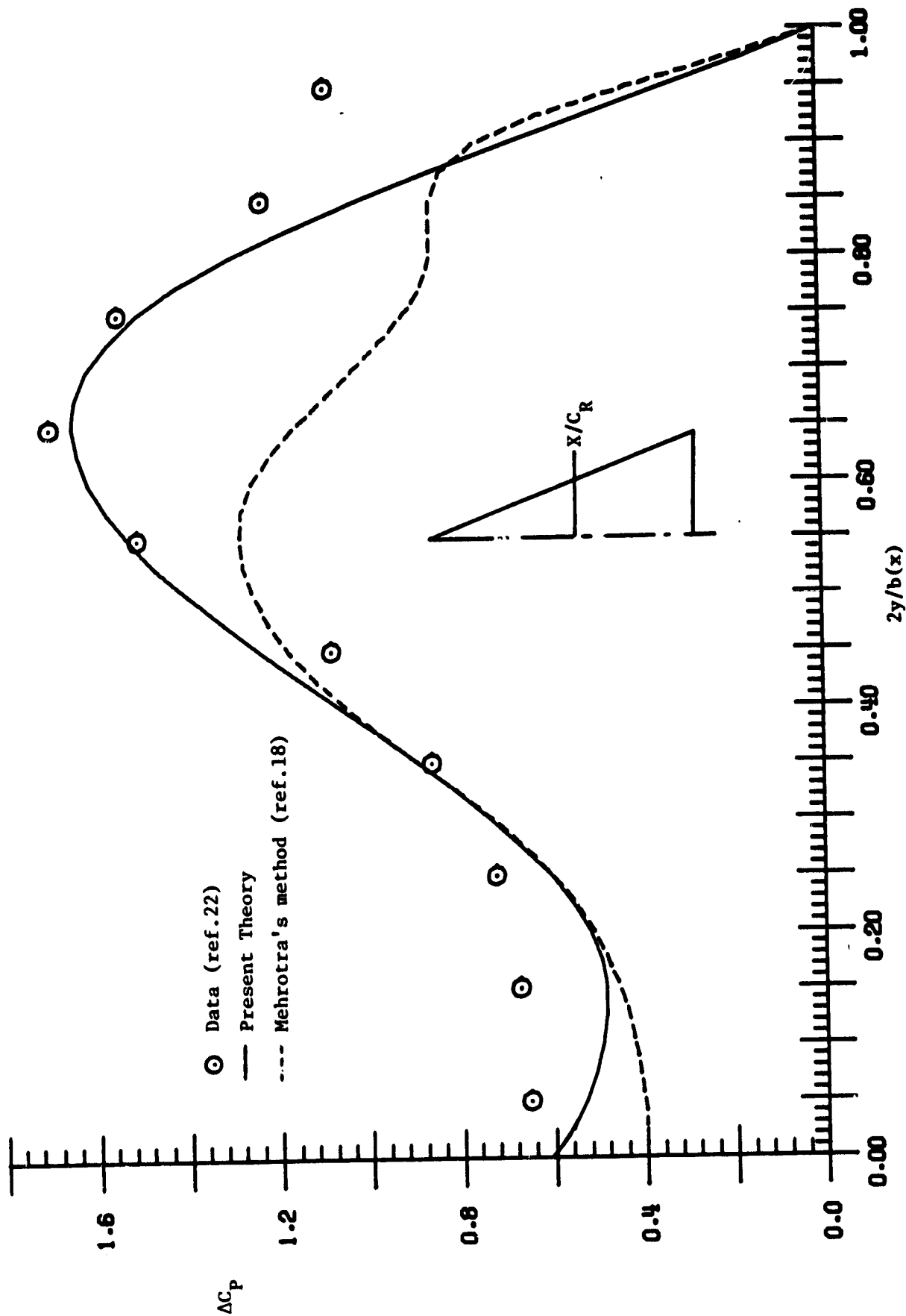
Figure 22.— Lifting pressure distribution for. AR = 1.147 Flat Delta Wing at 20.4 degree angle of attack; M = 0.

(a) $X/C_R = 0.5333$

105
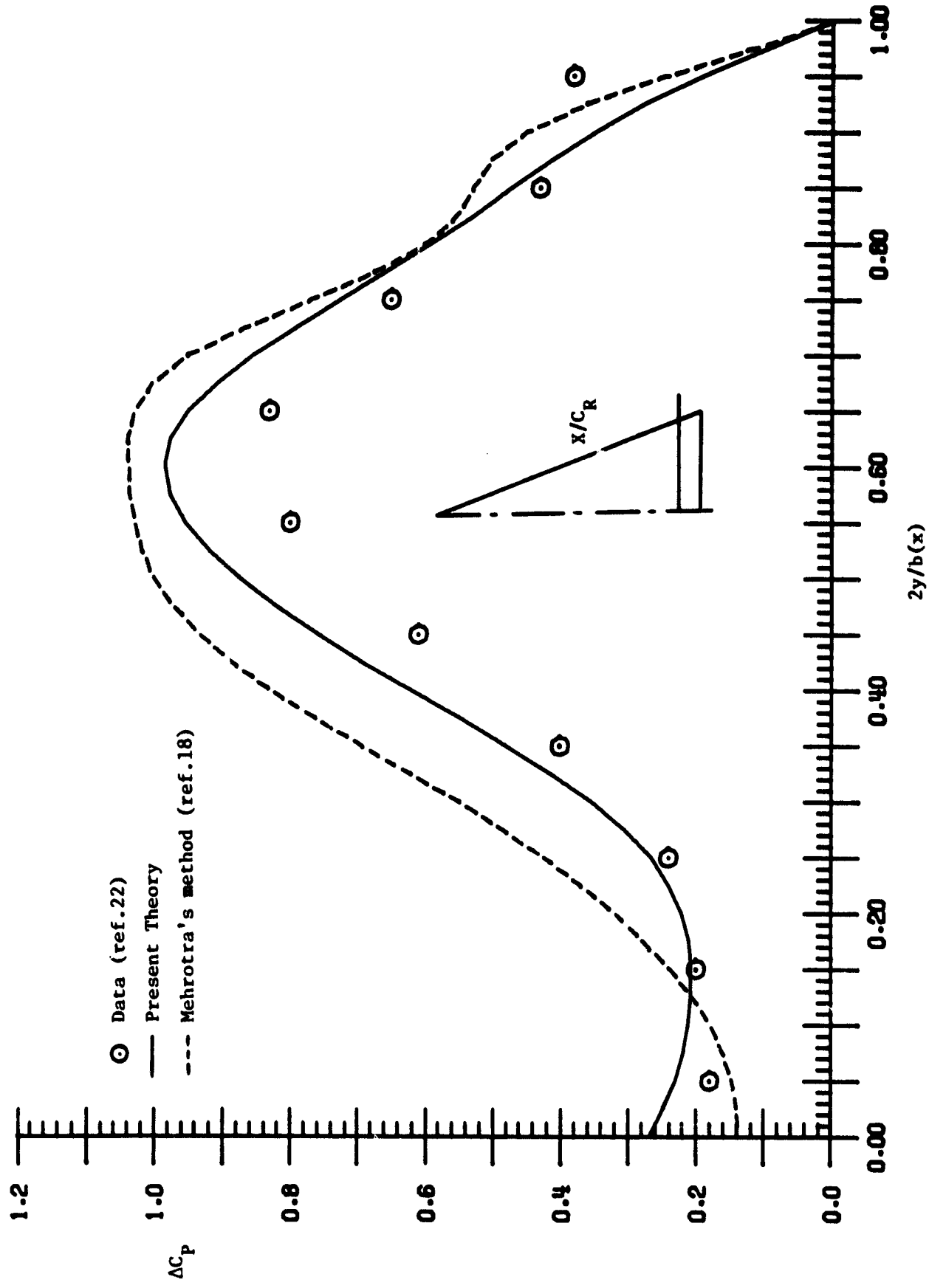
(b) $\bar{x}/C_R = 0.9333$

Figure 22.- Concluded.

106
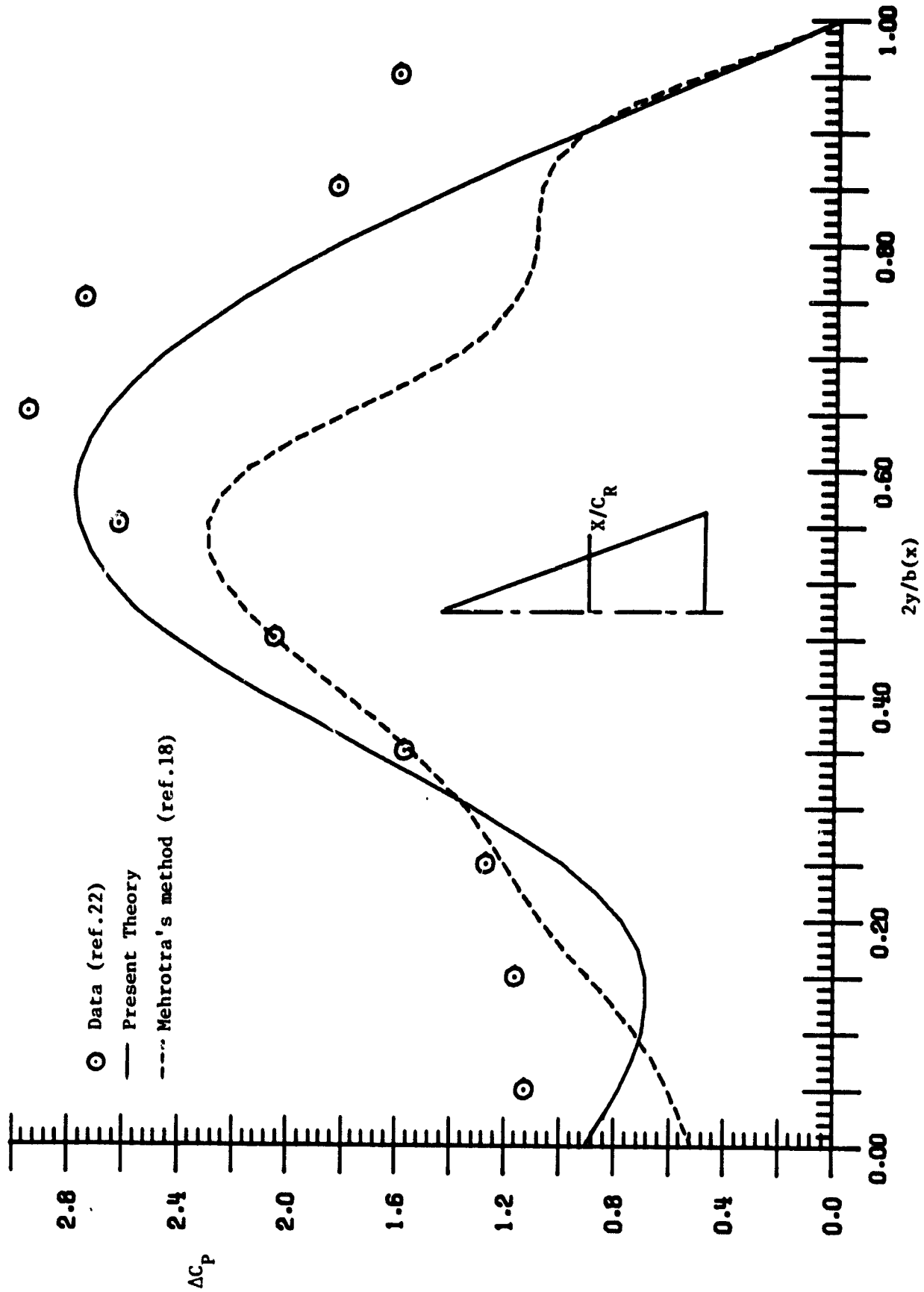
(a) $x/c_R = 0.5333$

Figure 23.- Lifting pressure distribution for AR = 1.147 Flat Delta Wing at 30.7 degree angle of attack; M = 0.

107
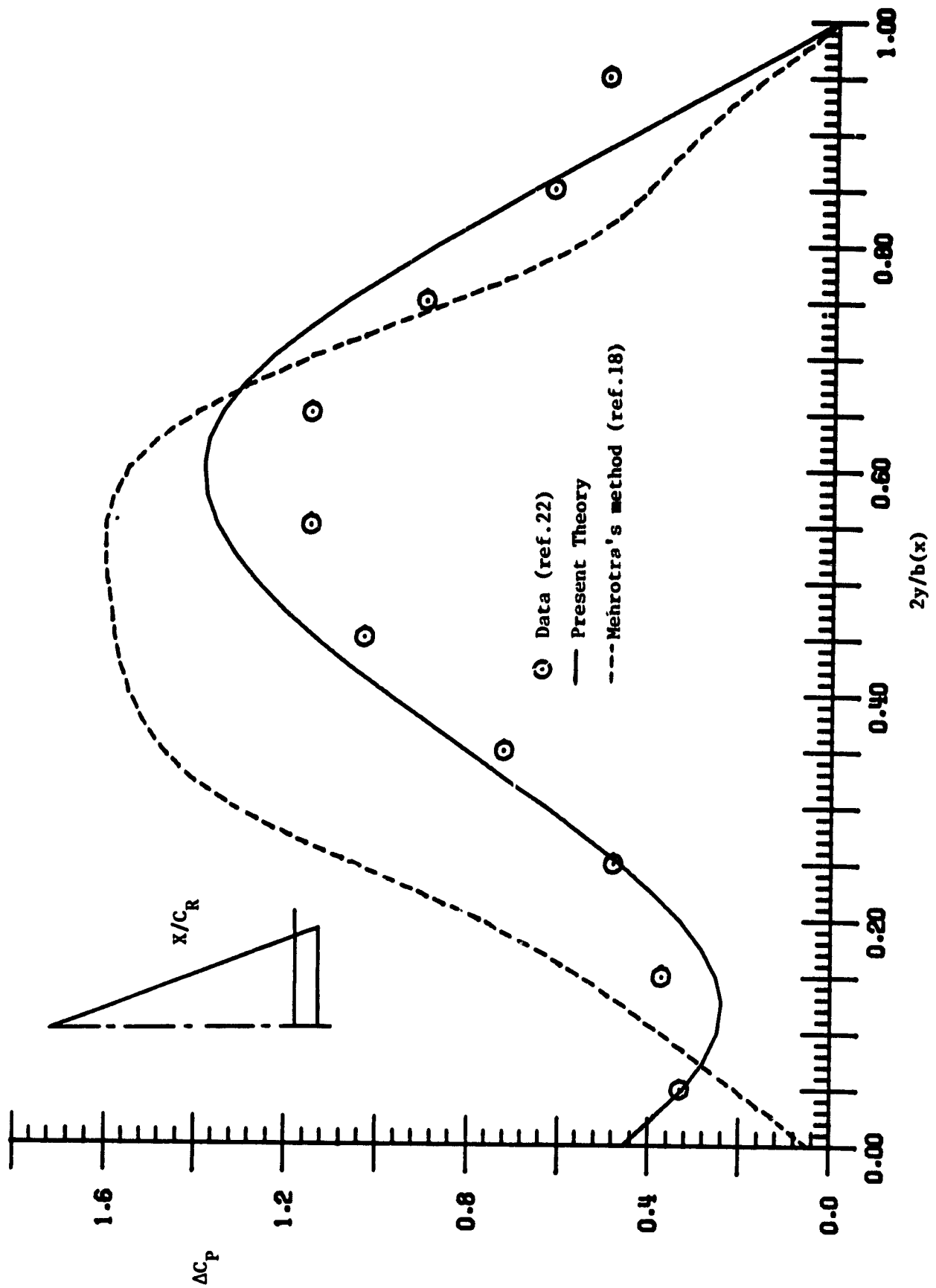
(b) $x/C_R = 0.9333$

Figure 23.- Concluded.

108
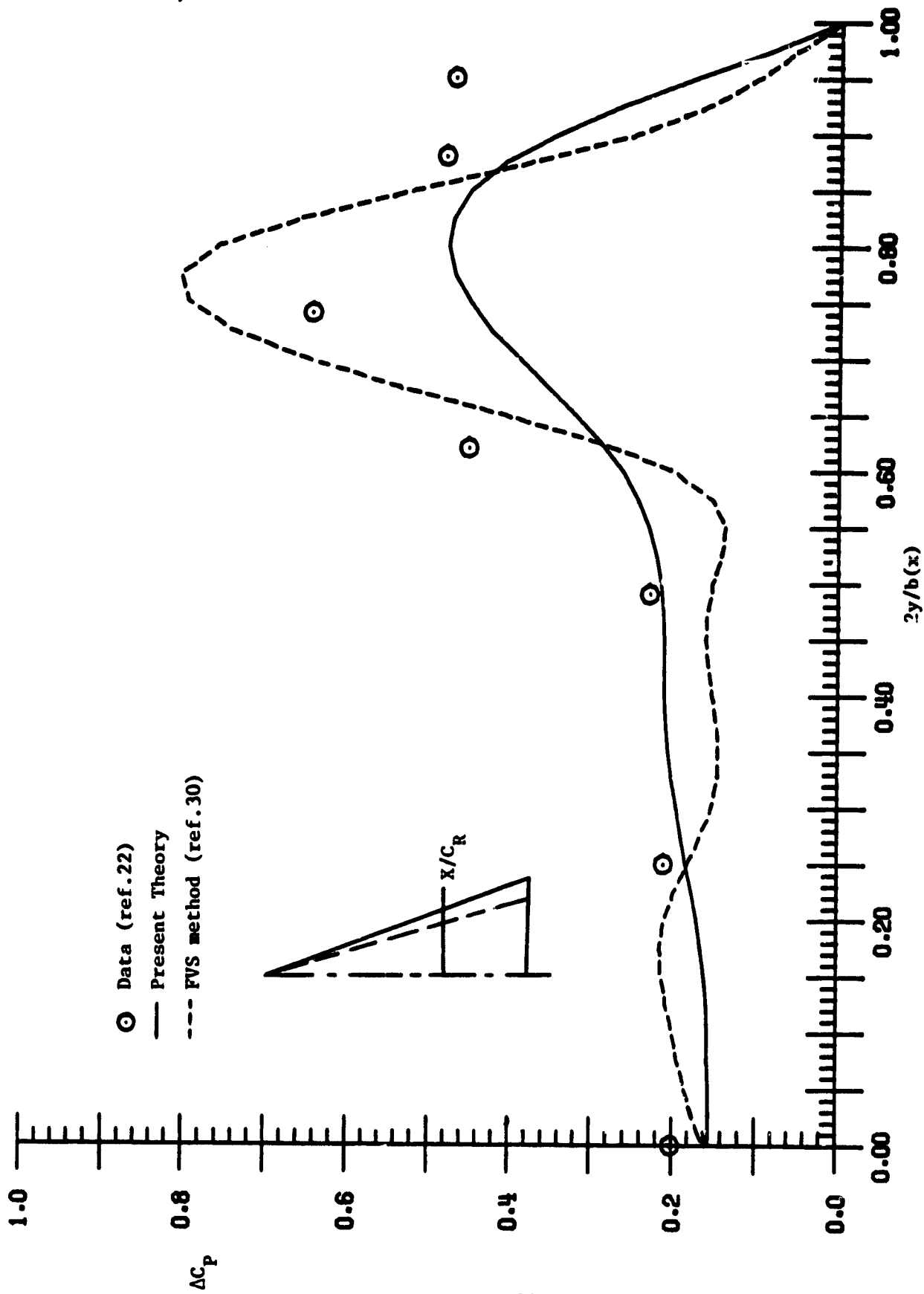
Figure 24.- Lifting pressure distribution for $A_L = 1.1493$ Conical Cambered
Delta at 10.2 degree angle of attack; $M = 0$.

(a) $X/C_R = 0.67$

109
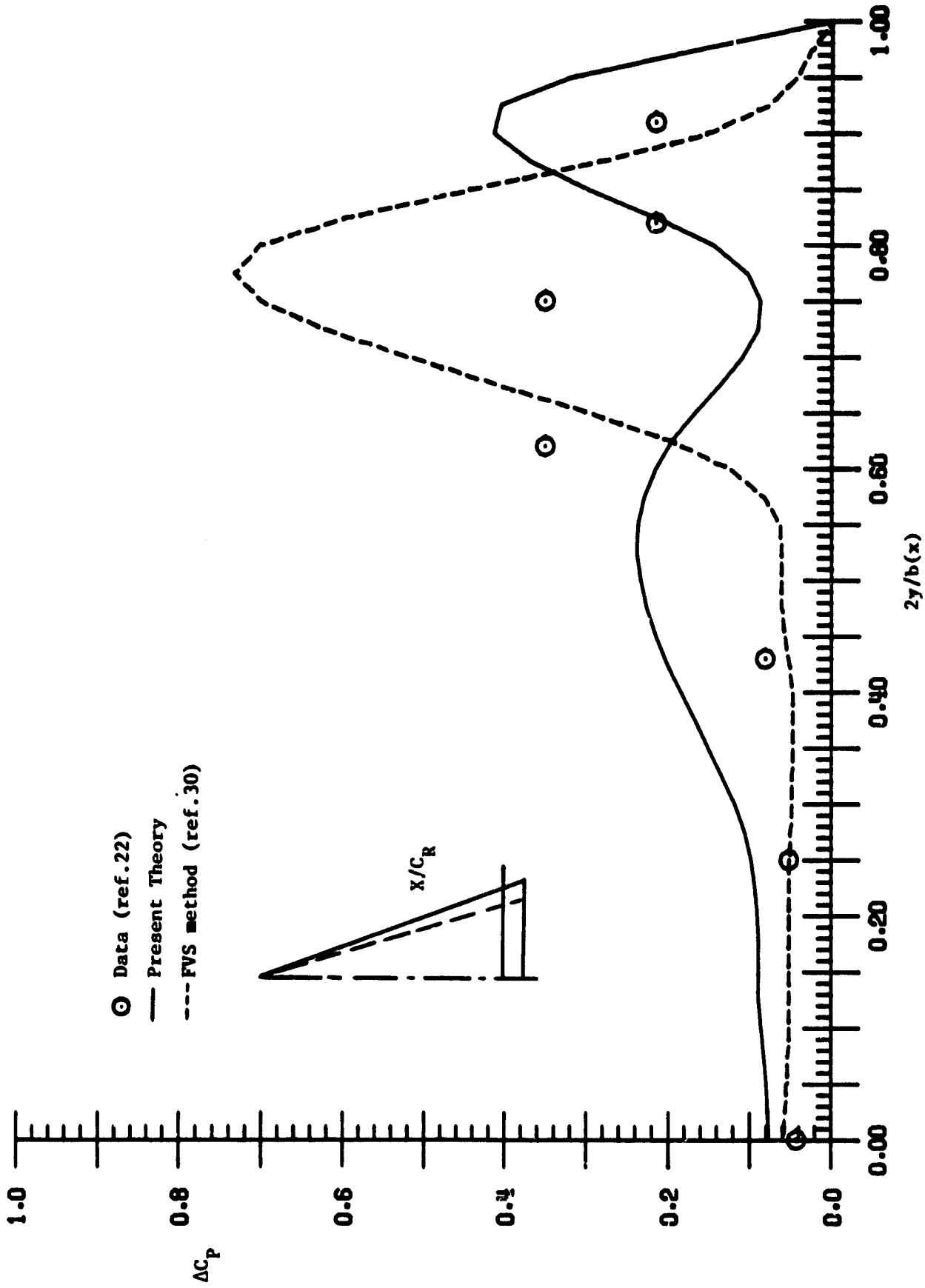
(b) X/C_R = 0.935

Figure 24.- Concluded.

110
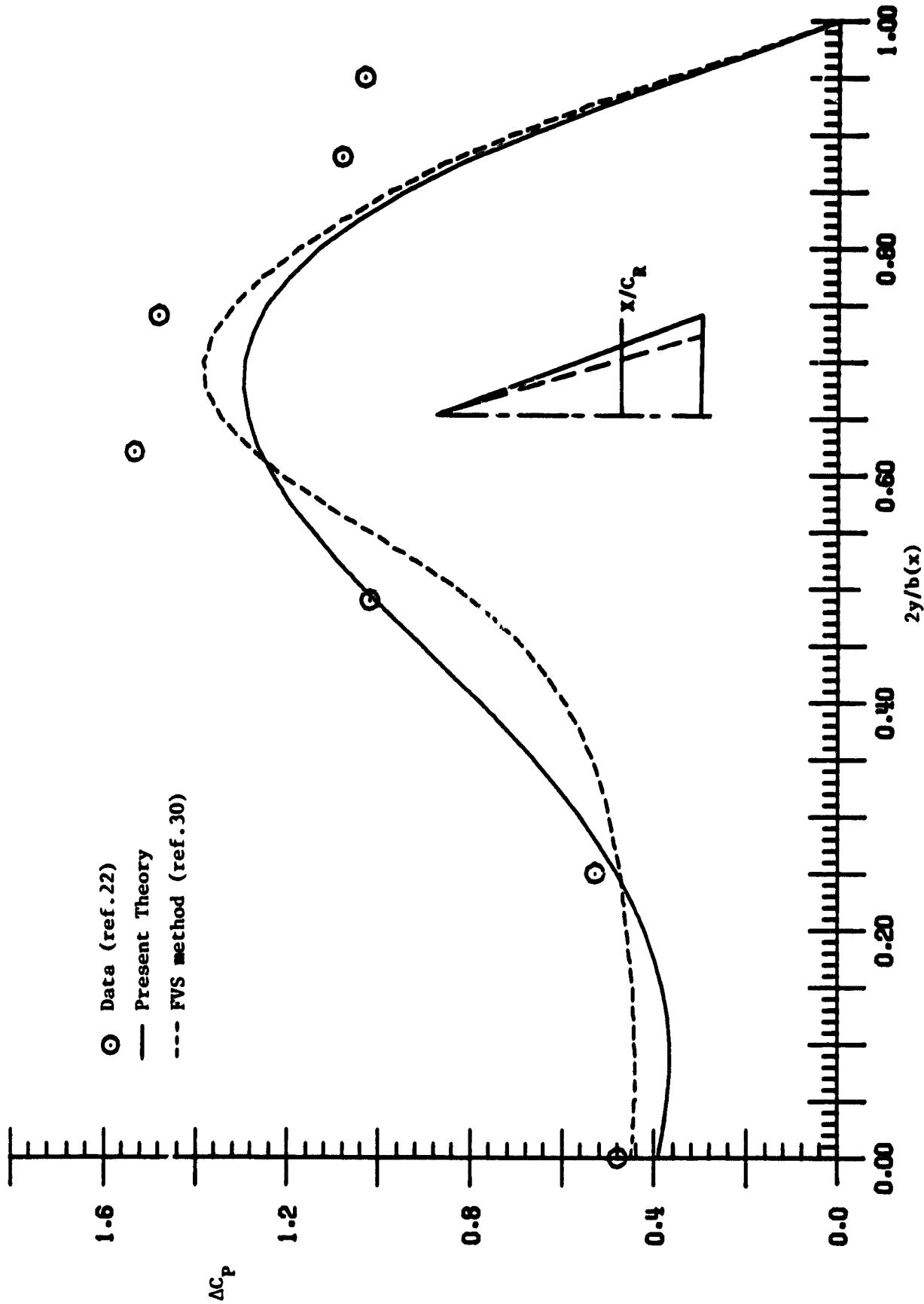
Figure 25.- Lifting pressure distribution for AR = 1.1493 Conical Cambered Delta at 20.4 degree angle of attack; M = 0.

(a) $X/C_R = 0.6/$

ΔC_P

2y/b(x)

⊙ Data (ref.22)
— Present Theory
--- FVS method (ref.30)

$2y/b(x)$

ΔC_P
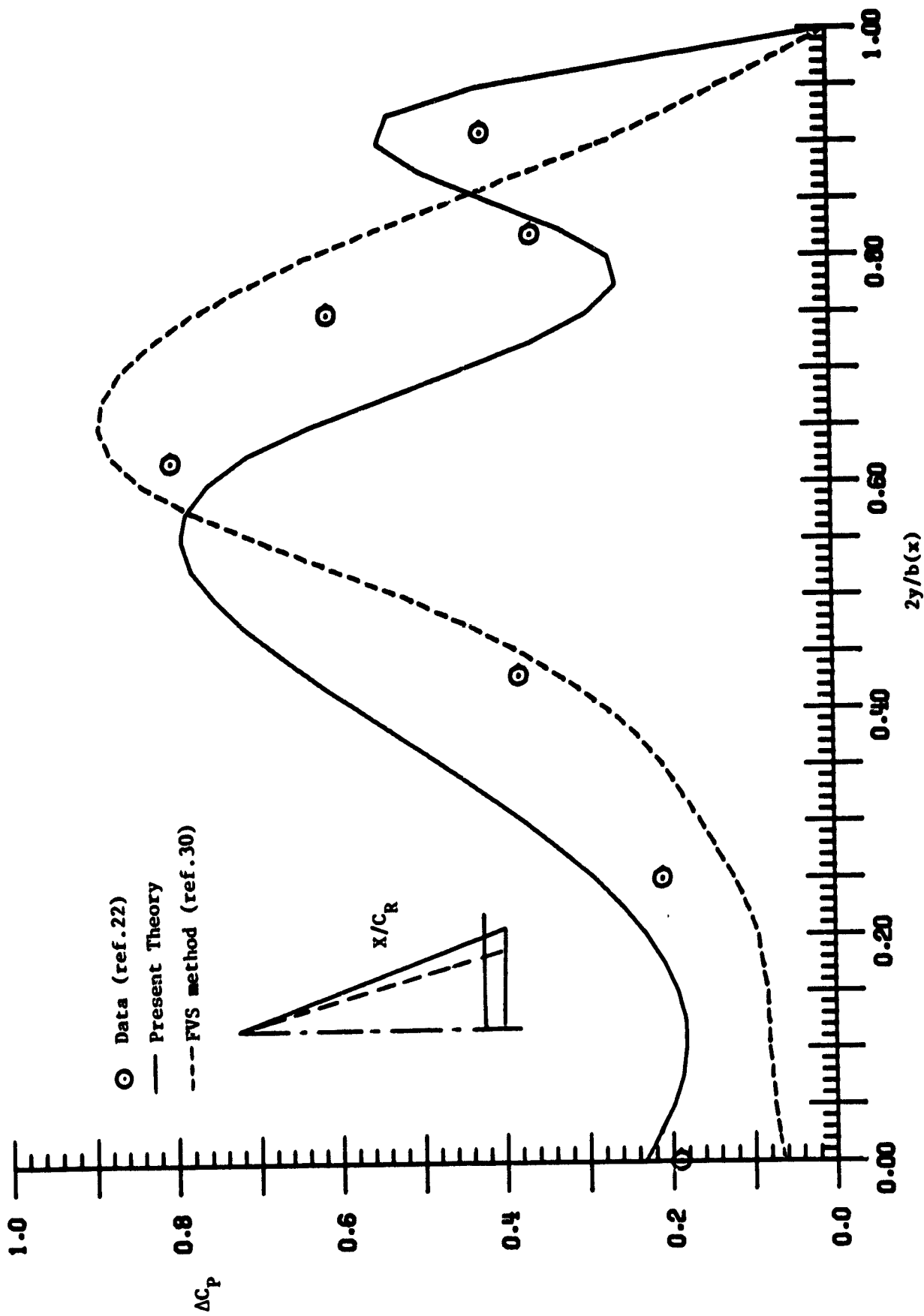
(b) $x/C_R = 0.935$

Figure 25.- Concluded.

112

○ Data (ref.22)
── Present Theory
--- FVS method (ref.30)

ΔC_P

$2y/b(x)$

x/C_R
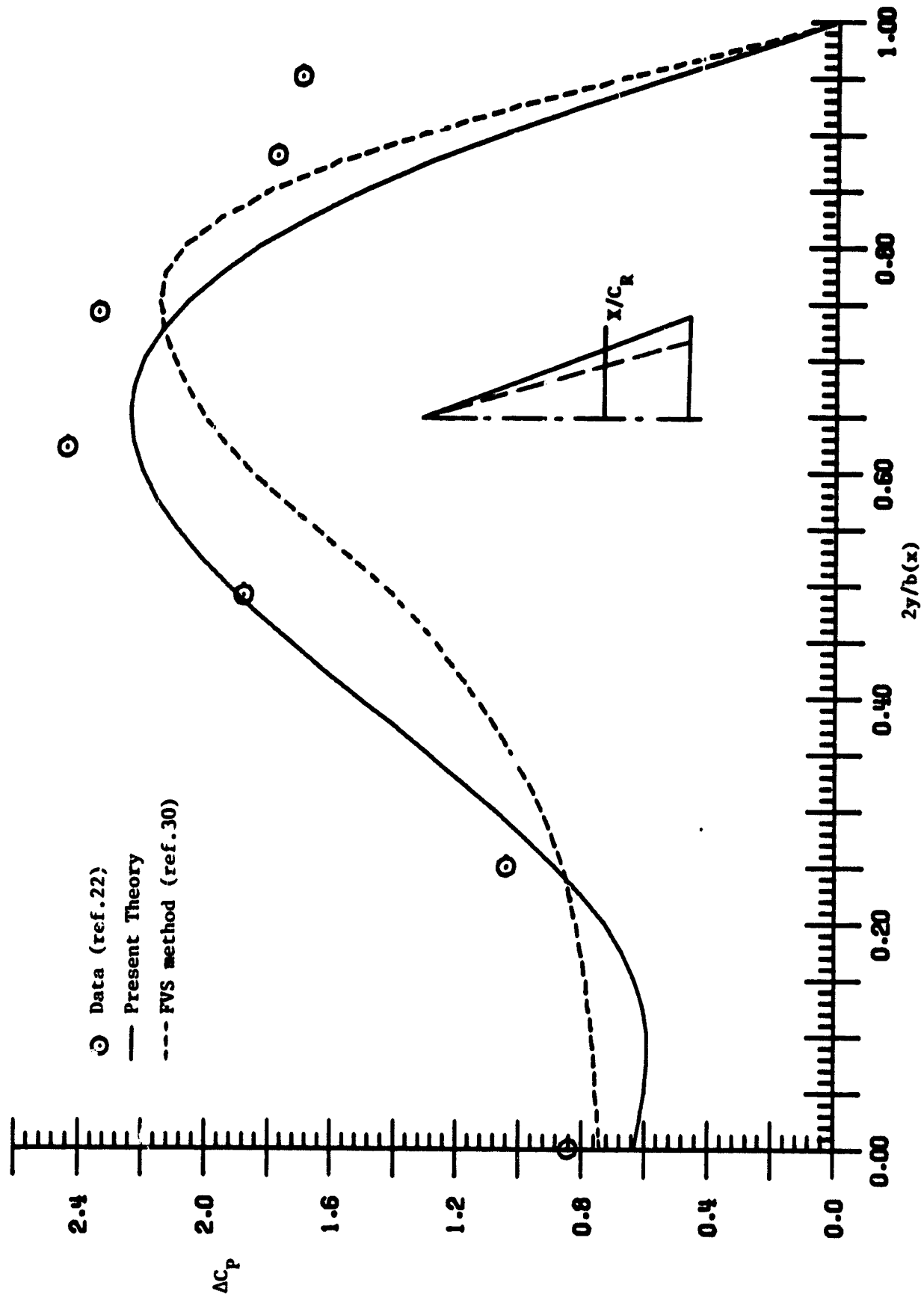
(a) $X/C_R = 0.67$

Figure 26.- Lifting pressure distribution for AR = 1.1493 Conical Cambered

Delta at 30.7 degree angle of attack; M = 0.

113
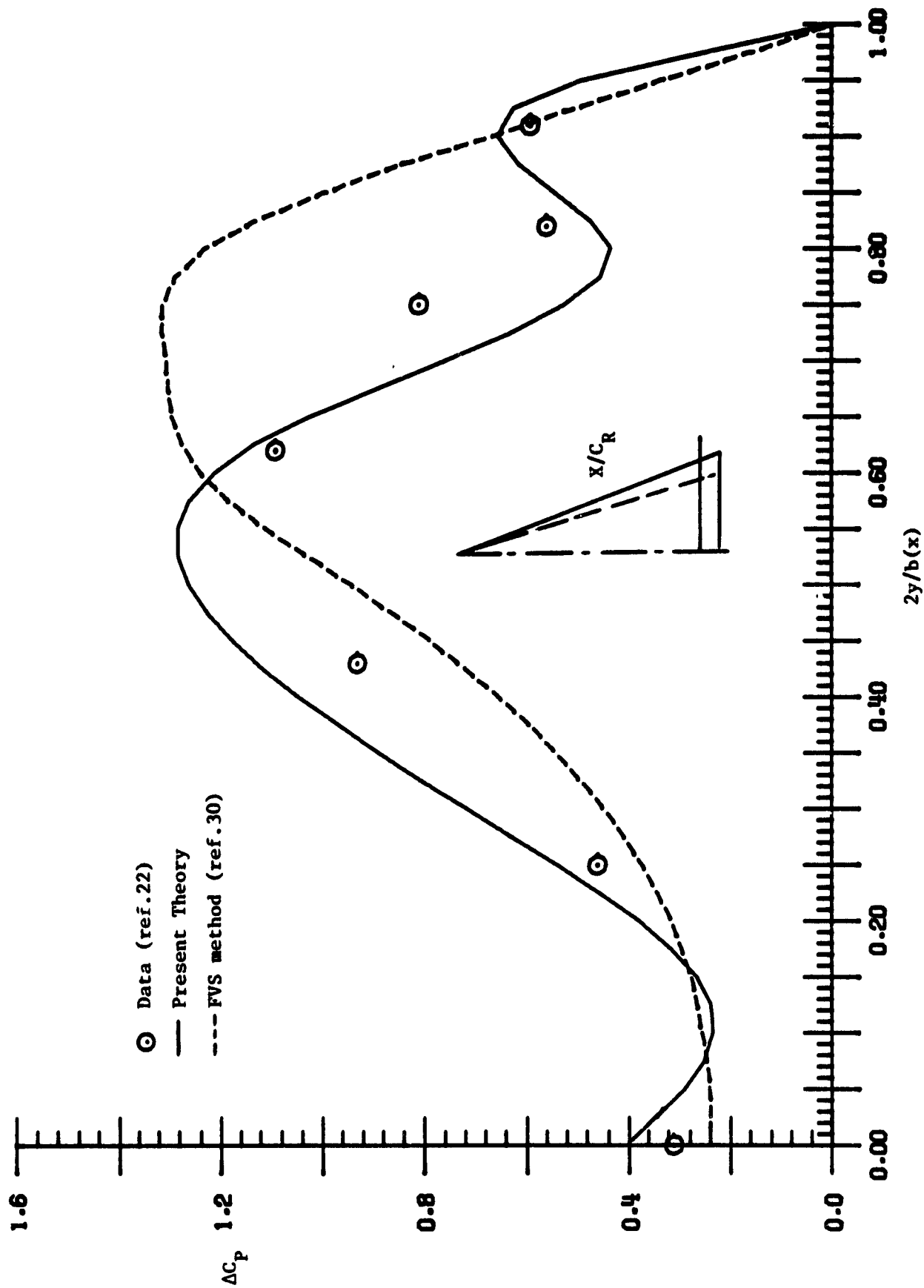
(b) $x/c_R = 0.935$

Figure 26.- Concluded.

114
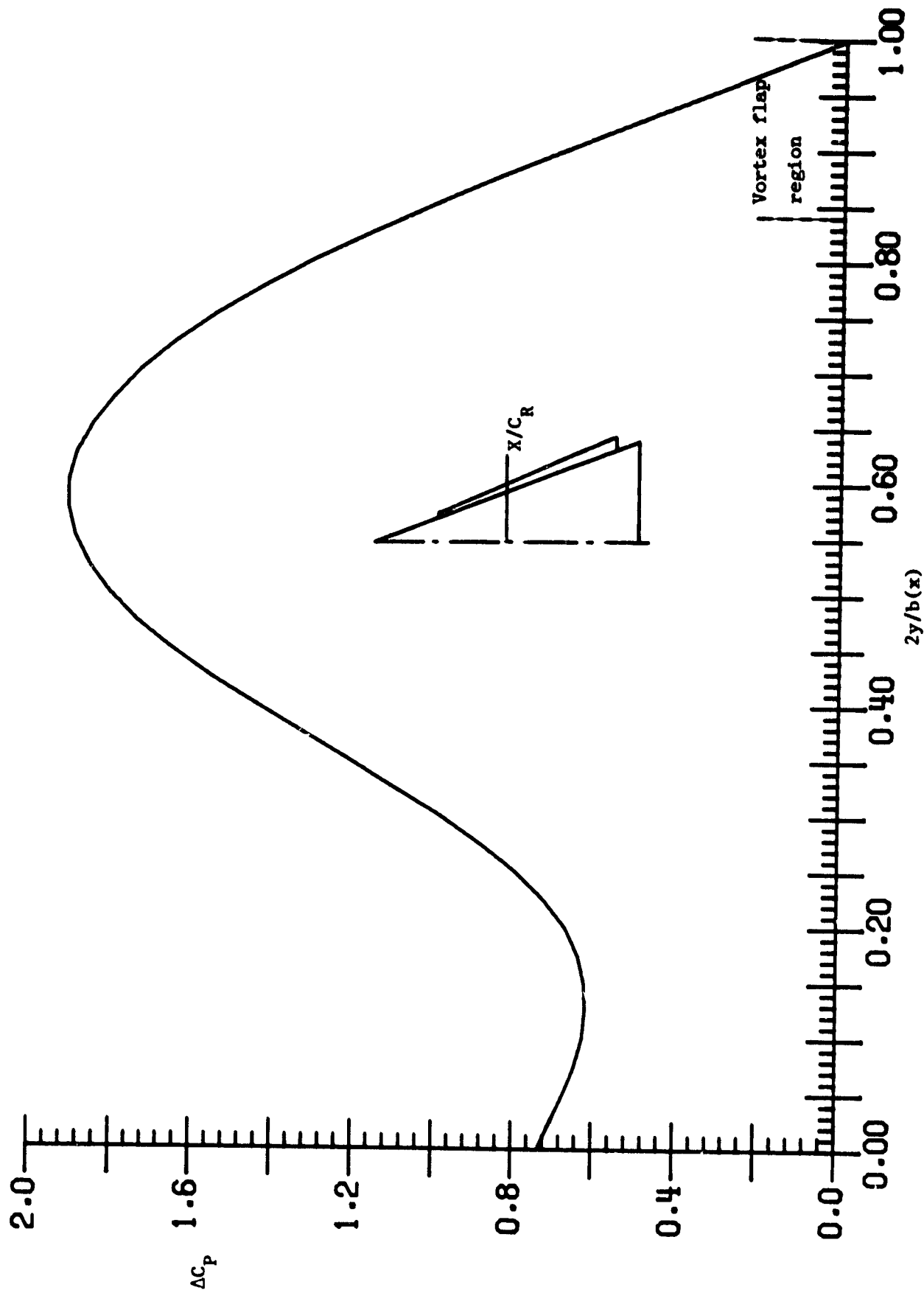
Figure 27.- Lifting pressure distribution for AR = 1.147 Delta Wing with a Leading-Edge
Vortex Flap at 24 degree angle of attack; δ_{ϵ} = 30°, M = 0.2 .

(a) X/C_R = 0.5129
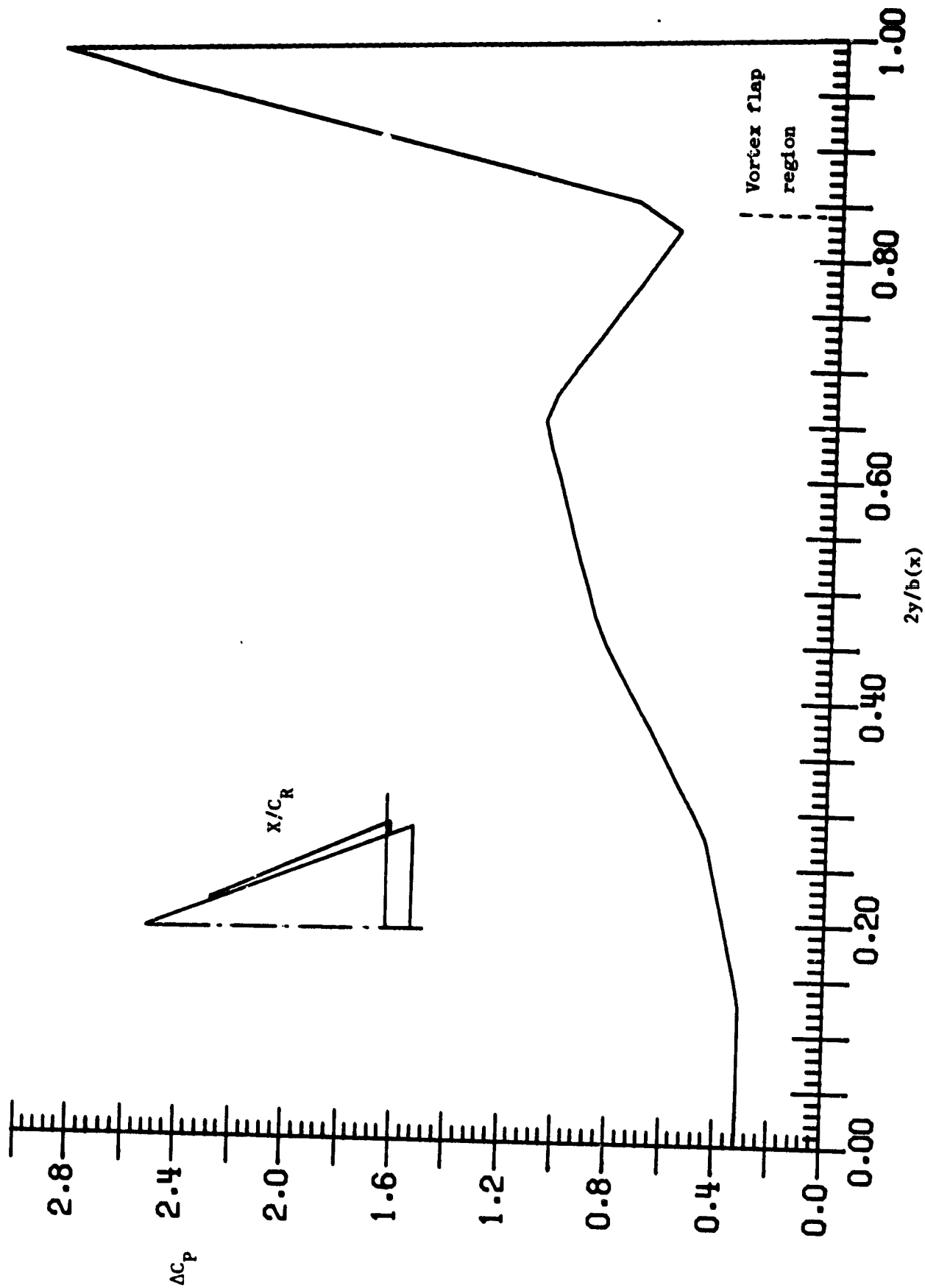
(b) $x/c_R = 0.8937$

Figure 27.- Concluded.

116
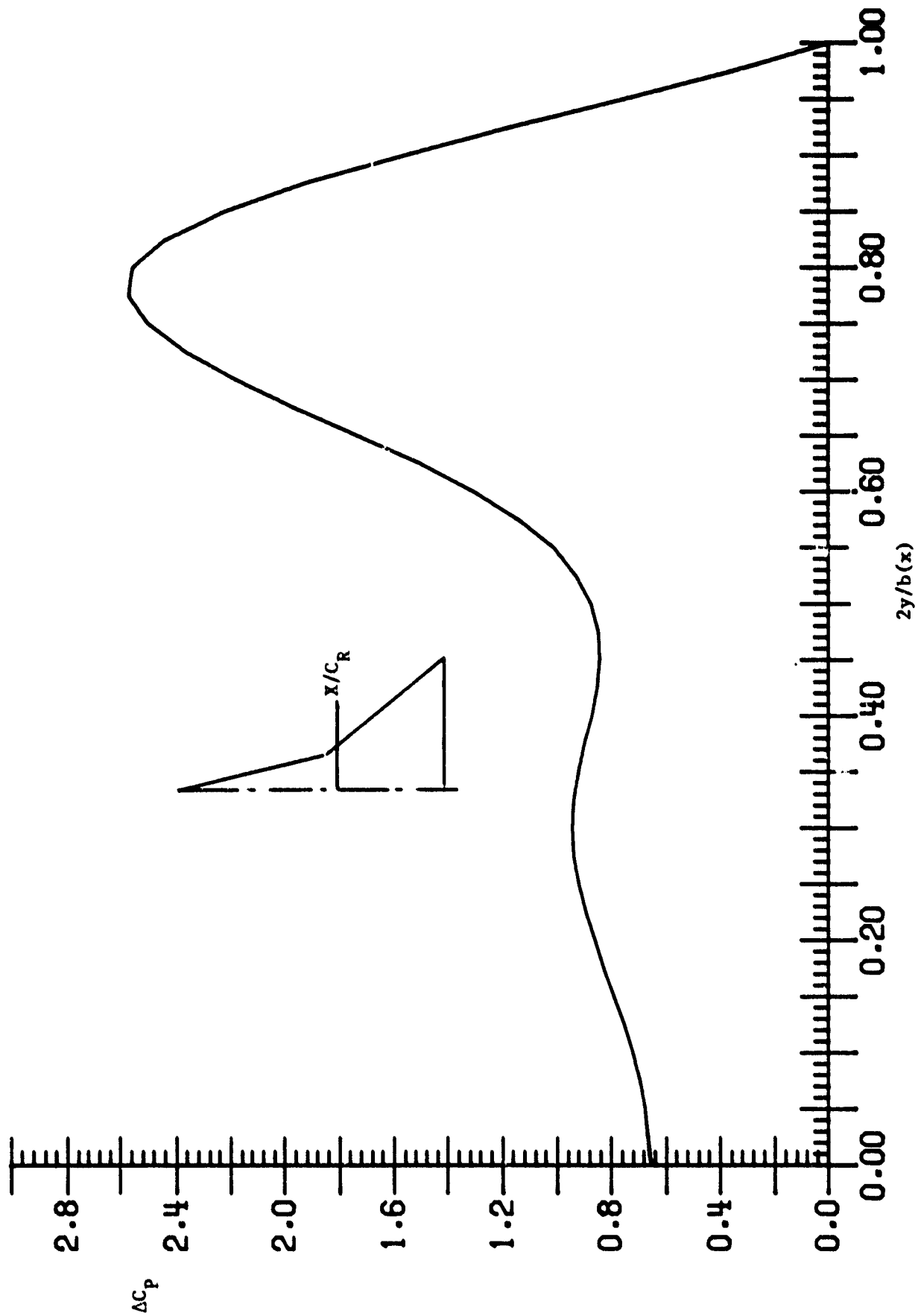
(a) $X/C_R = 0.5686$

Figure 28.- Lifting pressure distribution for Double Delta Wing at 20 degree angle of attack; M = 0.
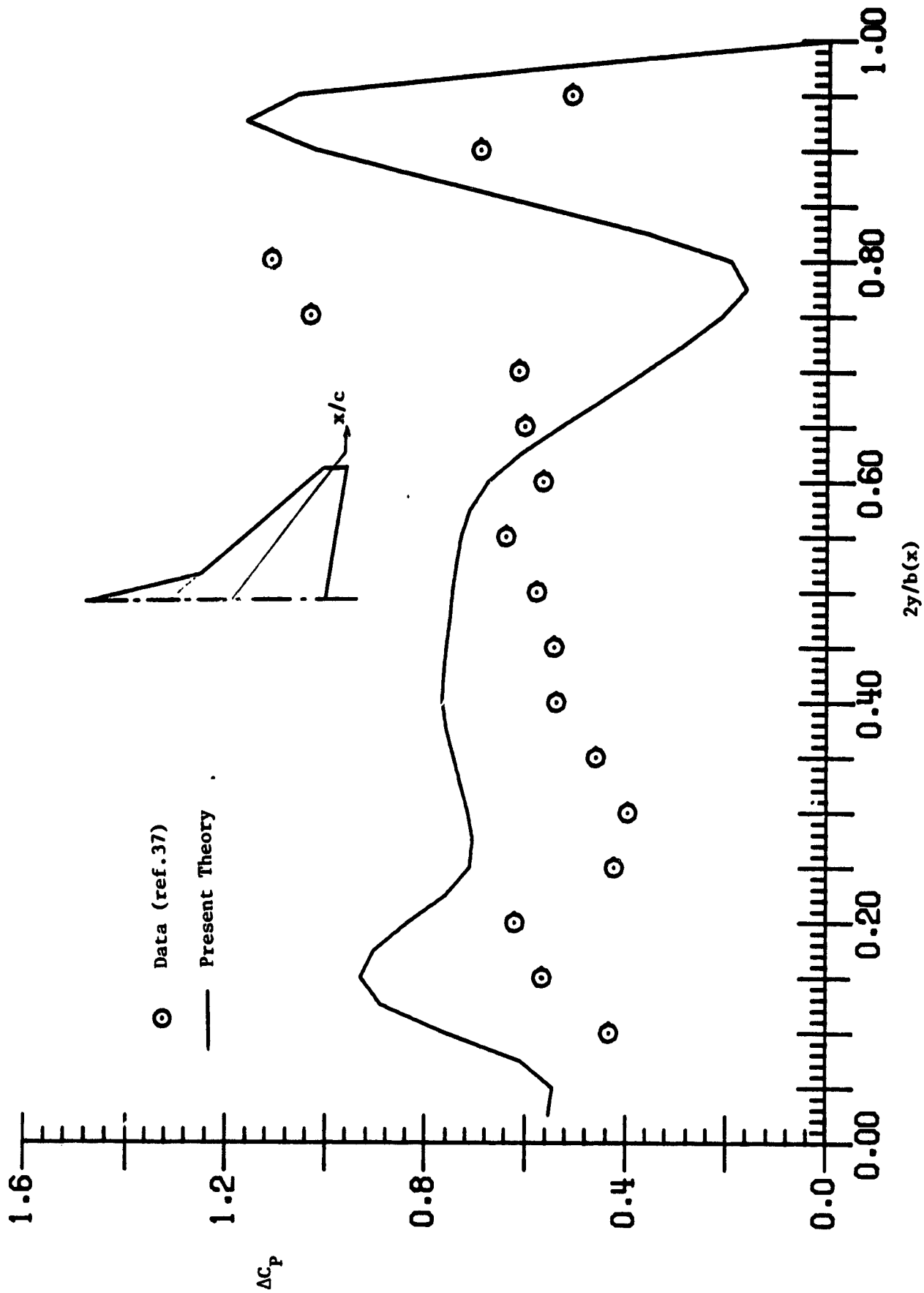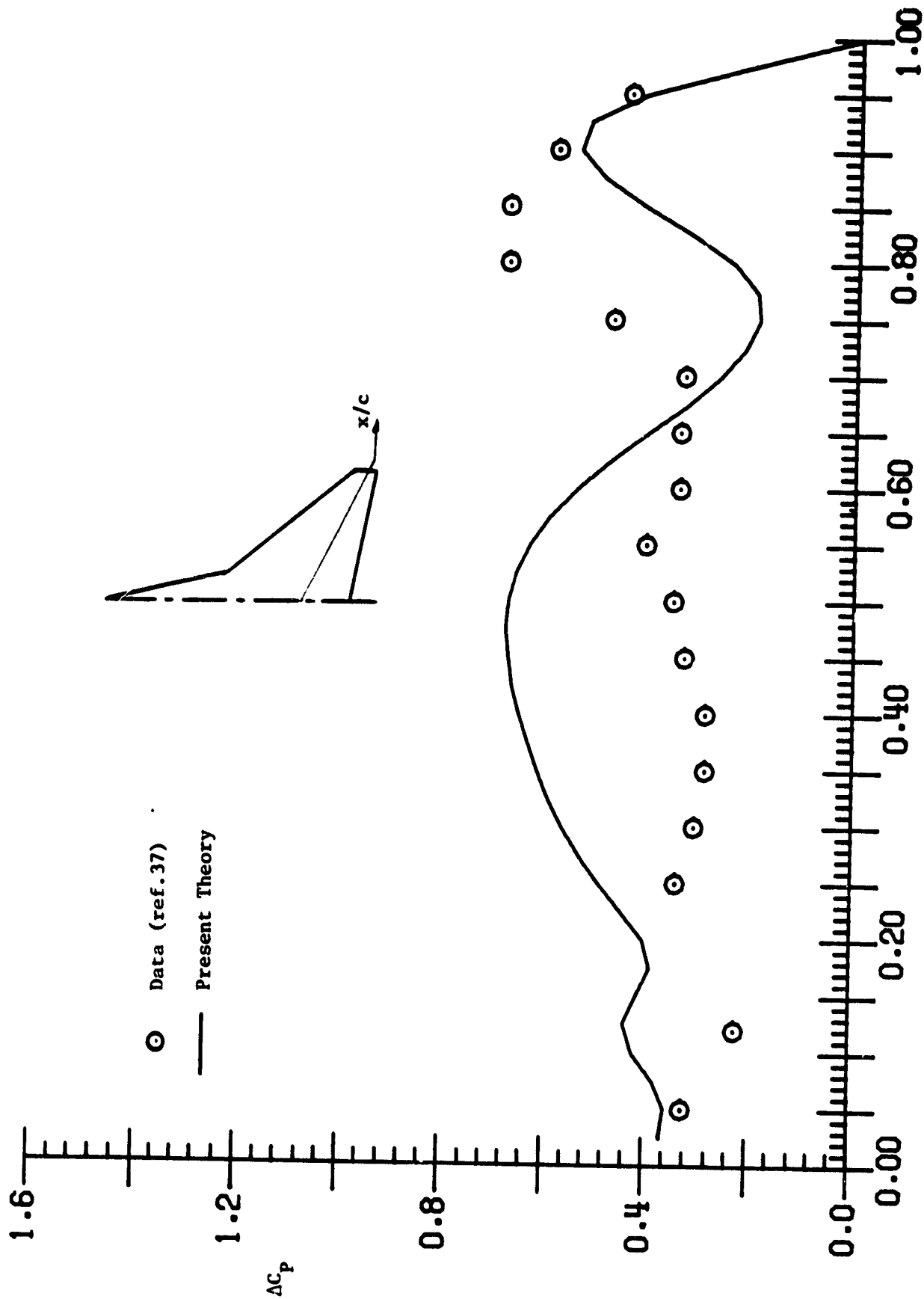
117
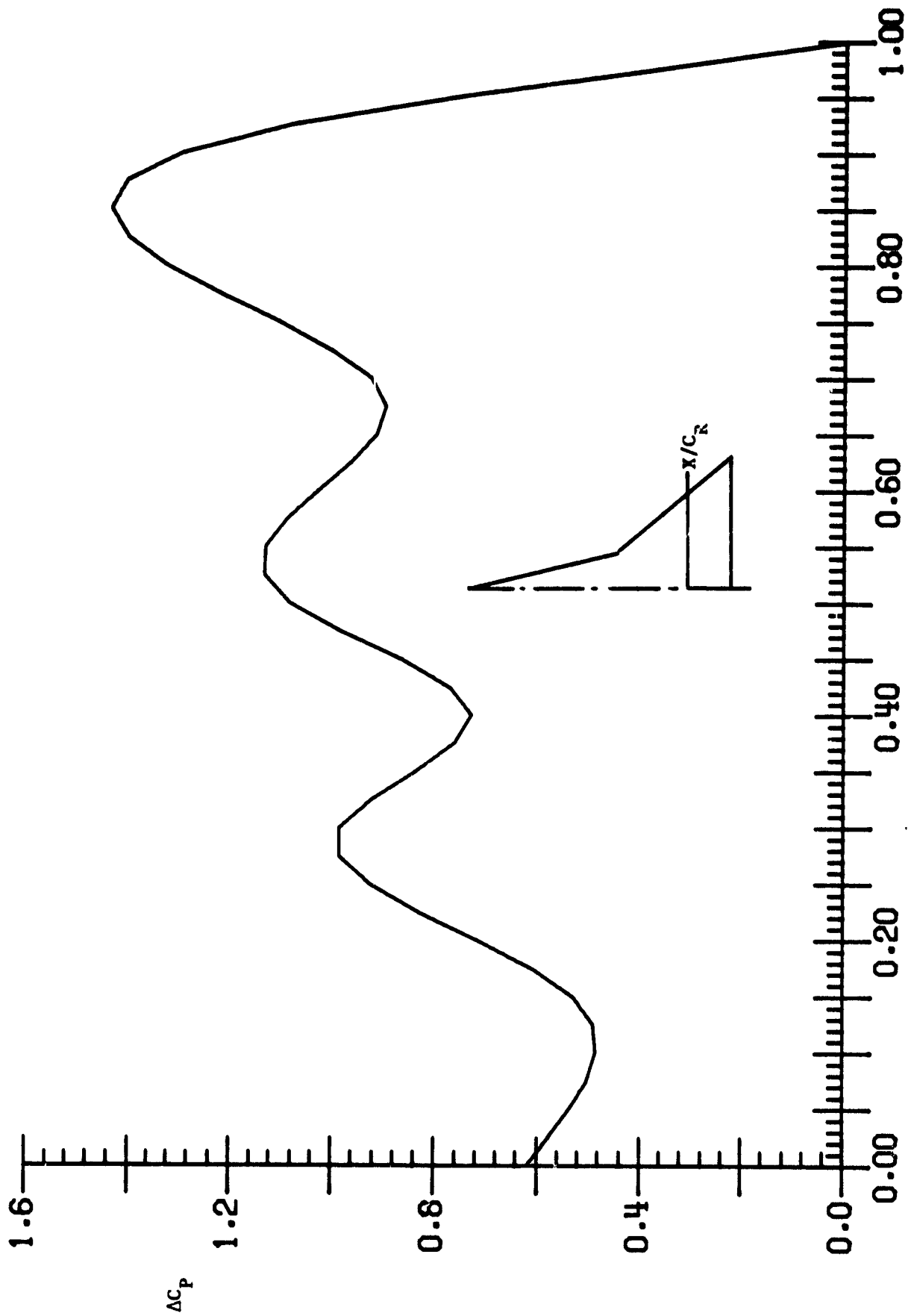
(b) $X/C_R = 0.8099$

Figure 28.- Concluded.

Figure 29.- Lifting pressure distribution for a Strake Wing at 12 degree

(a) x/c = 0.4

119

(b) $x/c = 0.7$

Figure 2°.- Continued.

120
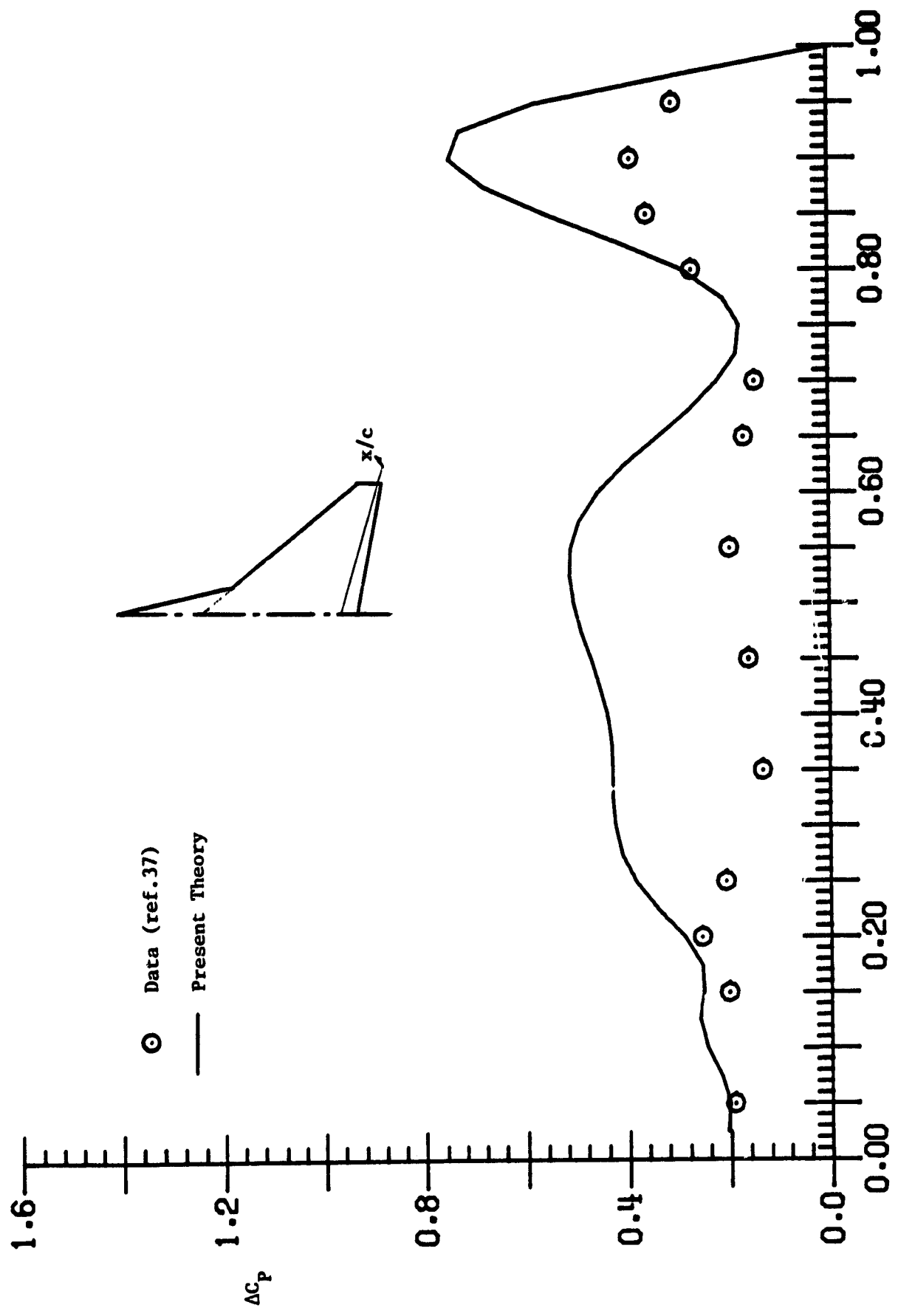
(c) x/c = 0.9

Figure 29.- Concluded.

121